LOUGHBOROUGH UNIVERSITY

Mathematical modelling of nonlinear internal waves in a rotating fluid

by

Azwani Binti Alias

A Doctoral Thesis

Submitted in partial fulfilment of the requirements for the award of Doctor of Philosophy of Loughborough University

in the

Faculty of Science

Department of Mathematical Sciences

September 2014

"In every mathematical investigation, the question will arise whether we can apply our mathematical results to the real world "

V. I. Arnold.

Abstract

Large amplitude internal solitary waves in the coastal ocean are commonly modelled with the Korteweg-de Vries (KdV) equation or a closely related evolution equation. The characteristic feature of these models is the solitary wave solution, and it is well documented that these provide the basic paradigm for the interpretation of oceanic observations. However, often internal waves in the ocean survive for several inertial periods, and in that case, the KdV equation is supplemented with a linear non-local term representing the effects of background rotation, commonly called the Ostrovsky equation. This equation does not support solitary wave solutions, and instead a solitary-like initial condition collapses due to radiation of inertia-gravity waves, with instead the long-time outcome typically being an unsteady nonlinear wave packet. The KdV equation and the Ostrovsky equation are formulated on the assumption that only a single vertical mode is used. In this thesis we consider the situation when two vertical modes are used, due to a near-resonance between their respective linear long wave phase speeds. This phenomenon can be described by a pair of coupled Ostrovsky equations, which is derived asymptotically from the full set of Euler equations and solved numerically using a pseudo-spectral method. The derivation of a system of coupled Ostrovsky equations is an important extension of coupled KdV equations on the one hand, and a single Ostrovsky equation on the other hand. The analytic structure and dynamical behaviour of the system have been elucidated in two main cases. The first case is when there is no background shear flow, while the second case is when the background state contains current shear, and both cases lead to new solution types with rich dynamical behaviour. We demonstrate that solitary-like initial conditions typically collapse into two unsteady nonlinear wave packets, propagating with distinct speeds corresponding to the extremum value in the group velocities. However, a background shear flow allows for several types of dynamical behaviour, supporting both unsteady and steady nonlinear wave packets, propagating with the speeds which can be predicted from the linear dispersion relation. In addition, in some cases secondary wave packets are formed associated with certain resonances which also can be identified from the linear dispersion relation. Finally, as a by-product of this study it was shown that a background shear flow can lead to the anomalous version of the single Ostrovsky equation, which supports a steady wave packet.

Keywords:

Internal waves, rotating ocean, Ostrovsky equation, coupled Ostrovsky equations, strong interactions, shear flow, resonance, steady and unsteady wave packets, pseudo-spectral method, sponge layer, dealiasing, asymptotic multiple-scale expansions.

Publications

The results of this thesis are partially summarised in the following papers and proceeding:

- ALIAS, A., GRIMSHAW, R. H. J. and KHUSNUTDINOVA, K. R. (2013) On strongly interacting internal waves in a rotating ocean and coupled Ostrovsky equations. *Chaos: An Interdisciplinary Journal of Nonlinear Science*, **23**(2) 023121.

- ALIAS, A., GRIMSHAW, R. H. J. and KHUSNUTDINOVA, K. R. (2014) Coupled Ostrovsky equations for internal waves, with a background shear flow. *Procedia IUTAM: Nonlinear Interfacial Wave Phenomena from the Micro-to the Macro-Scale*, 3-14.

- ALIAS, A., GRIMSHAW, R. H. J. and KHUSNUTDINOVA, K. R. (2014) Coupled Ostrovsky equations for internal waves in a shear flow. arXiv:1407.09.39 [nlin.PS]. *Submitted to Physics of Fluid.*

Acknowledgements

Bismillahi ar-rahmaan ar-rahim

In the Name of Allah the Most Gracious and Most Merciful

First of all, my praise and thanks to my Lord Allah, the Most Gracious and Most Merciful for enabling me to complete my PhD study successfully. Thank you for blessing and guiding me throughout this journey. I wish to extend my deepest gratitude and appreciation to everyone who contributed to the successful completion of my thesis.

I would like to express my sincere thankfulness to my supervisors Professor Roger Grimshaw and Dr Karima Khusnutdinova for their consistent research guidance and valuable support throughout this work. This thesis could not have been written without their constant advice. During my PhD study, I have learned a great deal from them, especially how to approach the scientific problems and how to write scientific reports properly. They gave me many valuable comments and suggestions through numerous discussion along this journey. I really appreciate their patience, help and time.

I would like to thank Universiti Malaysia Terengganu and the Ministry of Higher Education of Malaysia for giving me the opportunity to pursue my PhD study in Loughborough University and the financial support during my stay in UK.

I wish to bestow my deepest thanks to my beloved husband Mr Noorakmal Ikram Azizan for his endless support, love and prayers. I also thank my lovely son, Nazrin Ammar and my newborn daughter, Nazneen Amani who gave me so much joy and pleasure during my study. Thank you for always understanding and being by my side. I am always very grateful to all my family members especially my parents, Alias Yahya and Azma Senun for their unconditional prayers, love and support. Without their love and support, this thesis would never have been possible.

Lastly, I sincerely thank the entire staff and research students in the School of Mathematical Sciences at Loughborough University, especially my officemates, Ali and Konstantinos for their kind help and support.

Contents

List of Figures

List of Tables

Abbreviations

KdV	**K**orteweg-**d**e **V**ries
DFT	**D**iscrete **F**ourier **T**ransform
FFT	**F**ast **F**ourier **T**ransform
PS	**P**seudo-**S**pectral
NLS	**N**onlinear **S**chrödinger
KP	**K**adomtsev-**P**etviashvili

Chapter 1

Introduction

The ubiquity of internal waves in the ocean and atmosphere has been recognised, and these waves have been intensively studied over the past few decades. They commonly occur in shallow coastal seas, straits, fjords and lakes, see the reviews by Grimshaw [2], Holloway et al. [3], Helfrich and Melville [4]. Oceanic internal waves can sometimes be seen through their surface signature, although the largest displacements occur in the ocean interior. Atmospheric internal waves can also be seen as formations of clouds, which are made up of numerous rows of small clouds known as 'mackerel sky' and can emerge as several roll clouds known as 'morning glory' in the atmospheric boundary layer [5, 6]. The common occurrence of internal waves in the ocean and atmosphere is well documented, due to *in situ* observations, satellite images and also several significant laboratory experiments [3]. Mathematical modelling of these phenomena aims to generate nonlinear equations that describe their properties, which is a significant and important step in research.

The emphasis of the present study is on internal waves in the ocean, which is currently a very active research topic. Oceanic internal waves are waves in the interior of the ocean, which exist in density-stratified fluids. The difference in water density is mostly due to a difference in water temperature, but can also be due to a difference in salinity. The interface between layers of different densities is

called a pycnocline. However, when the density difference is due to temperature it is called a thermocline, and when it is due to salinity it is called a halocline.

It is now widely accepted that the weakly nonlinear long wave model, Korteweg-de Vries (KdV) equation plays an important role in describing the dynamics of internal waves. It is the simplest equation which incorporates both nonlinearity and dispersion. The characteristic feature of this model is the solitary wave, which results from a balance between these two effects. Nonlinearity tends to localise the wave while dispersion spreads it out. This concept is fascinating and well documented in many papers, which provide the basic paradigm for the interpretation of the oceanic observations, see Benjamin [7], Grimshaw et al. [8], Grimshaw [2], Holloway et al. [3], Ostrovsky and Stepanyants [9], Grimshaw et al. [10].

The solitary wave is the nonlinear wave of permanent form, initially observed in 1834, when the Scottish engineer John Scott Russell accidently noticed the 'great wave of translation' or the 'great solitary wave' while he was riding on horseback along the Edinburgh - Glasgow canal for a few miles before losing it in the meanders of the canal. He observed that a wave emerged at the front of a boat when it abruptly stopped and then he reported his observations and his subsequent experiments to the British Association in his Report on Waves, see Russell [11].

The first mathematical theory which aimed to describe Russell's findings of solitary waves had to wait more than three decades. It was first performed by Boussinesq who proposed such a theory and later this was confirmed by some investigations by Rayleigh [12]. Later, Korteweg and de Vries [13] derived a nonlinear evolution equation governing long one dimensional, small amplitude, surface gravity waves propagating in a shallow water channel of constant depth and they found solitary wave solutions, see Miles [14, 15]. This equation now bears their names (abbreviated as the KdV equation) although Boussinesq appeared to derive it first. Since its development by Korteweg and de Vries in 1895, hundreds of papers have been published based on KdV-type models for solitary waves in a wide variety of physical contexts, to name but a few (see, for example Lee and Beardsley [16], Ostrovsky

[17], Maslowe and Redekopp [18], Holloway et al. [19], Grimshaw [2], Helfrich and Melville [4]).

The phenomenon was forgotten until Zabusky and Kruskal [20] integrated the KdV equation numerically while they were investigating the Fermi-Pasta-Ulam (FPU) lattice model problem. They showed that these solitary wave solutions have a remarkable property of preserving their shapes and speeds while they travel and after the collisions with other solitary waves, and furthermore, the interaction of the KdV solitary wave is elastic with some additional spatial phase shift. The study of solitons by Zabusky and Kruskal [20] has led to the theoretical work by Gardner et al. [21] which showed that the KdV equation was integrable through an inverse scattering transform and led to a milestone in the discovery of the soliton theory. Nowadays, soliton theory is a very active and interesting research area, which is closely related to modern physics because this theory is applied to explain many physical phenomena, in particular to describe the behaviour of long, weakly nonlinear waves. For this reason, both mathematicians and physicists pay much attention to soliton theory and until now, this theory has been continuously progressing and developing.

The weakly nonlinear models for long internal waves are based on the KdV equation and its generalisations, which include various extensions including the roles of topography and stratification, mean flows, friction, higher order nonlinearity and the Earth's rotation [4, 22]. In the real world, oceanic internal waves are often observed to survive for long distances over several inertial periods, and therefore the Earth's background rotation becomes notable and needs to be taken into account. The simplest model equation which takes account of background rotation is the Ostrovsky equation, also known as the rotation-modified Korteweg-de Vries equation (e.g. Chen and Boyd [23]), which is a modification of the KdV equation. The Ostrovsky equation is widely used in application to many physical problems, including the description of surface and internal waves in a rotating ocean, see Ostrovsky [17], Grimshaw [24], Grimshaw et al. [25, 26], Ostrovsky and Stepanyants [27] and magneto-sonic waves in a rotating plasma, see Obregon and Stepanyants [28]. Recently, Whitfield and Johnson [29] studied the strong and weak rotational

effects on the wave packets evolution. The Earth's background rotation plays a very important role in the present research, since in the presence of the Earth's rotation when there is no shear flow, a steady solitary wave solution does not exist, see Leonov [30] and Gilman et al. [31].

The studies from Renouard and Germain [32], Helfrich [33], Grimshaw and Helfrich [1], Grimshaw et al. [26], Grimshaw and Helfrich [34], using a combination of asymptotic analysis, numerical simulations, and laboratory experiments, have shown that the radiation of an inertial gravity wave causes a complete decay of the initial solitary wave, and eventually the long-time outcome is a coherent steadily propagating wave packet. Grimshaw and Helfrich [1] and Helfrich [33] explained that their numerical results show that the localised wave packet propagates with the associated maximum group velocity. Then, they constructed a weakly nonlinear theory of a higher order nonlinear Schrödinger (NLS) equation to describe the numerically found wave packet for the Ostrovsky equation, which propagates with the wavenumber of the extremum of the group velocity, see Grimshaw and Helfrich [1], Daisuke and Takuji [35]. Note that both equations, KdV and Ostrovsky, are formulated on the assumption that only a single vertical mode is used. Recent studies by Grimshaw et al. [36], Johnson and Grimshaw [37] have shown that strong rotation prevents the formation of undular bores structures.

Eckart [38] reported that it is possible for internal waves to have a nearly coincident phase speed of different modes, and there can be a resonant transfer of energy between waves. In this scenario, the KdV equation is replaced by two coupled KdV equations, see Gear and Grimshaw [39] and Grimshaw [40], describing a strong interaction between internal solitary waves of different modes. Various families of solitary waves can be expected from coupled KdV equations such as pure solitary waves, generalised solitary waves and envelope solitary waves depending on the structure of the linear dispersion relation [40]. In the present work, the study of the coupled KdV equations is extended by taking account of background rotation as well as background shear flow. It is found that the single Ostrovsky equation is replaced by two coupled Ostrovsky equations, each equation having both linear and nonlinear coupling terms.

The Ostrovsky equation, and a system of coupled Ostrovsky equations, belong to the class of universal mathematical models of nonlinear wave theory, and a study of the behaviour of their solutions is valuable for a variety of applications. In addition to the oceanographic applications already cited above, we can also mention the two-directional generalisation of the Ostrovsky equation derived by Gerkema [41]. The latter equation is related to the dynamics of a modified Toda lattice on an elastic substrate, considered by Daisuke and Takuji [35], where the emergence of nonlinear wave packets was also found, independently of the analogous results obtained by Grimshaw and Helfrich [1] for the Ostrovsky equation. Recently, a system of coupled Boussinesq equations has been derived as a model for long nonlinear waves in a layered solid waveguide with a soft bonding layer, see Khusnutdinova et al. [42]. A nonsecular weakly-nonlinear solution of the initial-value problem for this system has been constructed, under certain conditions, in terms of solutions of coupled and uncoupled Ostrovsky equations for unidirectional waves, see Khusnutdinova and Moore [43] and Khusnutdinova et al. [44]. Wave packets described by a single Ostrovsky equation were clearly observed in the numerical simulations for the coupled Boussinesq equations. Generalised solitary waves were generated in the case described in terms of solutions of the coupled Ostrovsky equations. Therefore, in general, solutions of the coupled Ostrovsky equations can significantly differ from the solutions of a single Ostrovsky equation, depending on the structure of the linear dispersion relation.

The structure of the thesis is given as follows. Chapter 2 introduces the theoretical background of the KdV-Ostrovsky model consisting of the balance between weak nonlinearity and weak dispersion and with additional background rotation effect. We review and re-derive the Ostrovsky equation from the complete set of equations of motion for an inviscid, incompressible, density stratified fluid with boundary conditions appropriate to an oceanic situation, using the asymptotic multiple-scales expansion method. We employ an Eulerian formulation for the derivation, and follow a similar strategy to the derivation of the KdV equation discussed by Grimshaw [2]. In the same chapter, we also discuss a soliton solutions of the KdV equation and nonlinear wave packet solutions of the Ostrovsky equation.

Chapter 3 demonstrates how a pair of coupled Ostrovsky equations can be systematically derived from the full set of Euler equations with free surface and rigid bottom boundary conditions, pertinent to the oceanic situation, using the asymptotic multiple-scales expansion method. This is an extension of the derivation from Chapter 2 when two different linear long wave modes have nearly coincident phase speeds.

Chapter 4 explains the numerical method that is used to solve the main equations. The numerical method is known as the pseudo-spectral method. This method is complemented with a linear damping region known as a sponge layer at the end of the domain and with a de-aliasing technique to treat the nonlinear and sponge layer terms in the system. Here, we considered two different types of initial conditions: an approximation to solitary wave solutions of coupled KdV equations; and a nonlinear wave packet based on certain predicted wavenumbers. We added a pedestal to the initial conditions.

The study is focussed on the situation where there are two different long wave modes with nearly coincident phase speeds in the presence of rotation. The main results of this thesis are divided into two different topics in Chapter 5 and Chapter 6, both of which take the Earth's rotation, or more specifically the Coriolis force into account. One of them concerns the easier problem in which the shear flow is not considered. This will be discussed in Chapter 5. Using parameters based on a three-layer model of the oceanic stratification, it is shown that typically initial solitary-like waves in the coupled system are destroyed, and replaced by nonlinear envelope wave packets, a two-component counterpart of the outcome for the single Ostrovsky equation (typical case).

Chapter 6 extends the problem considered in Chapter 5 by including the effect of shear flow. These studies simulate the propagation of internal solitary waves in a rotating fluid in the presence of shear flow in some idealised situations modelling the oceanic conditions. The dispersion relation of the system discloses various behaviours of weakly nonlinear oceanic internal waves including the existence of unsteady and steady envelope wave packets.

The final chapter provides the summary and the conclusions of the work throughout the thesis, together with description of the directions for future work.

As a by-product of the main study it was also shown that sufficiently strong shear near a pycnocline may lead to the anomalous version of the single Ostrovsky equation, which is discussed in Appendix A.

Chapter 2

Theoretical Background of KdV equation and Ostrovsky equation

2.1 Introduction

The KdV and Ostrovsky equations are the canonical models for the description of internal solitary waves and their relatives, commonly observed in the oceans (for example, see the reviews in Grimshaw [2], Helfrich and Melville [4], Grimshaw et al. [25] and references therein). Both equations are derived on the assumption that the dynamics is dominated only by a single linear long wave mode and written in a reference frame moving with the linear long wave speed. The Ostrovsky equation given by Ostrovsky [17], Grimshaw [24],

$$\{A_t + \nu A A_x + \lambda A_{xxx}\}_x = \gamma A\,, \tag{2.1}$$

is an extension of the KdV equation

$$A_t + \nu A A_x + \lambda A_{xxx} = 0\,, \tag{2.2}$$

in the presence of background rotation. Here $A(x,t)$ is the amplitude of the linear long wave mode $\phi(z)$ corresponding to the linear long wave phase speed c, which

is determined from the modal equations

$$(\rho_0 W^2 \phi_z)_z + \rho_0 N^2 \phi = 0\,, \tag{2.3}$$

$$\phi = 0 \quad \text{at} \quad z = -h\,, \quad \text{and} \quad W^2\phi_z = g\phi \quad \text{at} \quad z = 0\,; \tag{2.4}$$

$\rho_0(z)$ is the stable background density stratification, $\rho_0 N^2 = -g\rho_{0z}$, $W = c - u_0$ where $u_0(z)$ is the background shear flow, and it is assumed there are no critical levels, that is $W \neq 0$ for any z in the flow domain. The coefficients in the equations are given by

$$I\nu = 3\int_{-h}^{0} \rho_0 W^2 \phi_z^3\, dz\,, \quad I\lambda = \int_{-h}^{0} \rho_0 W^2 \phi^2\, dz\,, \quad I\gamma = f^2 \int_{-h}^{0} \rho_0 \Phi \phi_z\, dz\,, \tag{2.5}$$

where

$$I = 2\int_{-h}^{0} \rho_0 W \phi_z^2\, dz\,, \quad \rho_0 W\Phi = \rho_0 W\phi_z - (\rho_0 u_0)_z \phi\,, \tag{2.6}$$

and f is the Coriolis parameter. Note that when there is no shear flow, that is $u_0(z) \equiv 0$, then $\Phi \equiv \phi_z$ and $\gamma = f^2/2c$.

In this chapter, we briefly review the derivation of the Ostrovsky equations from the complete set of Euler equations for an inviscid, incompressible, density stratified fluid with boundary conditions appropriate to an oceanic situation, using the asymptotic multiple-scales expansions. This asymptotic derivation is done using the Eulerian formulation, following a similar strategy in Grimshaw [2] for the KdV equation. Then, we will discuss some general mathematical properties of solitary wave and wave packet solutions. We show the linear dispersion relation and present some preliminary numerical simulations using a pseudo-spectral method. Detailed description of the numerical method is given in Chapter 4.

2.2 Problem formulation and derivation of KdV-Ostrovsky type model equations

We consider the flow of an inviscid and incompressible fluid on a rotating frame. It is assumed that the fluid occupies the region $-h \leqslant z \leqslant 0$ with the plane $z = -h$ as the rigid bottom boundary and the plane $z = 0$ as the upper free surface boundary in the undisturbed state, see Figure 2.1. The problem is formulated by two dimensional governing equations in the xz-plane, where x and z denote the horizontal and vertical coordinates, respectively.

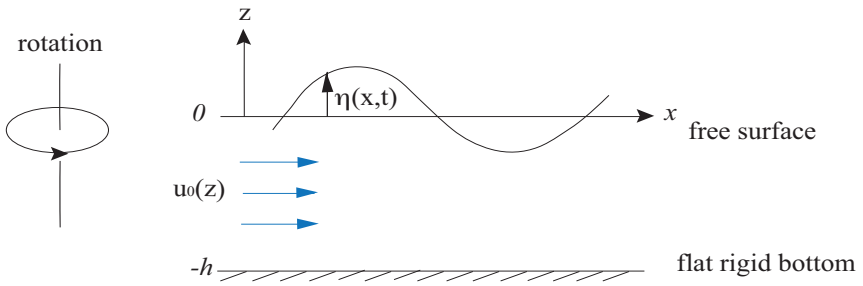

FIGURE 2.1: Configuration of the flow

In the basic state, the fluid has a background density stratification $\rho_0(z)$, a corresponding pressure $p_0(z)$ such that $p_{0z} = -g\rho_0$ and a horizontal shear flow $u_0(z)$ in the x-direction. When $u_0 \neq 0$, this basic state is maintained by a body force i.e, the term $\rho_0 f u_0$ in (2.7b) is balanced by this body force. The body force can be anything to maintain the stream or the current [45]. Then, the equations of

motion relative to this basic state are:

$$\begin{aligned}
\rho_0(u_t + u_0u_x + wu_{0z}) + p_x &= -(\rho_0 + \rho)(uu_x + wu_z - fv) - \rho(u_t + u_0u_x \\
&\quad + wu_{0z}) \,, \qquad (2.7a)\\
\rho_0(v_t + u_0v_x + fu) + \rho f u_0 &= -(\rho_0 + \rho)(uv_x + wv_z) - \rho(v_t + u_0v_x) \\
&\quad - \rho f u, \qquad (2.7b)\\
p_z + g\rho &= -(\rho_0 + \rho)(w_t + (u_0 + u)w_x + ww_z) \,, \qquad (2.7c)\\
g(\rho_t + u_0\rho_x) - \rho_0 N^2 w &= -g(u\rho_x + w\rho_z) \,, \qquad (2.7d)\\
u_x + w_z &= 0 \,. \qquad (2.7e)
\end{aligned}$$

Here, the terms (u_0+u, v, w) are the corresponding velocity components in (x, y, z) directions, $\rho_0 + \rho$ is the density, $p_0 + p$ is the pressure, t is time, $N(z)$ is called the buoyancy frequency or Brunt-Väisälä frequency , defined by $\rho_0 N^2 = -g\rho_{0z}$. The free surface and rigid bottom boundary conditions to the above problem are given by:

$$\begin{aligned}
w &= 0, \quad \text{at} \quad z = -h \,, \qquad (2.8a)\\
p_0 + p &= 0, \quad \text{at} \quad z = \eta \,, \qquad (2.8b)\\
\eta_t + (u_0 + u)\eta_x &= w, \quad \text{at} \quad z = \eta \,. \qquad (2.8c)
\end{aligned}$$

The constant h is the undisturbed depth of the fluid, and η describes the displacement of the free surface from its undisturbed position $z = 0$. In the subsequent derivation, a new variable ζ is used as the vertical particle displacement relative to the basic state, which is related to the vertical speed, w. It is defined by the equation:

$$\frac{D\zeta}{Dt} = \zeta_t + (u_0 + u)\zeta_x + w\zeta_z = w, \qquad (2.9)$$

and satisfies the boundary condition:

$$\zeta = \eta \quad \text{at} \quad z = \eta. \qquad (2.10)$$

The Ostrovsky equation is a modification of the KdV equation, which first appeared in the study of oceanic waves which included background rotation in the model [17]. So, the derivation of the Ostrovsky equation follows the same strategy as the derivation of the KdV equation [2, 3, 10]. By taking the leading linear long wave order of equations (2.7a)-(2.7e), and linearised boundary conditions (2.8b) and (2.8c), the solution of ζ is given by an expression of the form $A(x-ct)\phi(z)$, while the remaining dependent variables are given in (2.15). In general there is an infinite set of solutions for $[\phi(z);c]$. When considering only one mode, the asymptotic procedure leads to the Ostrovsky equation. The modal function $\phi(z)$ is defined by the following boundary-value problem:

$$(\rho_0 W^2\phi_z)_z + \rho_0 N^2\phi = 0 \quad \text{in} \quad -h < z < 0 \tag{2.11a}$$

$$\phi = 0 \quad \text{at} \quad z = -h\,, \tag{2.11b}$$

$$W^2\phi_z = g\phi \quad \text{at} \quad z = 0\,. \tag{2.11c}$$

Here, $W = c - u_0(z)$ where c is the long wave speed and $u_0(z)$ is the background shear flow. It is assumed that there are no critical levels, that is $W \neq 0$ for any z in the flow domain.

To proceed with the derivation of the evolution equation, it is necessary to set up the two small parameters, α and ϵ, characterising the wave amplitude and the dispersion of particle displacement of interface, respectively. Thus, the scaled variables are assigned by:

$$\tau = \epsilon\alpha t\,, \quad s = \epsilon(x-ct)\,, \quad f = \alpha\tilde{f}\,, \tag{2.12}$$

where $\alpha = \epsilon^2$ and we seek a solution in the form of asymptotic multiple-scales expansions:

$$[\zeta, u, \rho, p] = \alpha[\zeta_1, u_1, \rho_1, p_1] + \alpha^2[\zeta_2, u_2, \rho_2, p_2] + \cdots\,, \tag{2.13}$$

$$[w, v] = \alpha\epsilon[w_1, v_1] + \alpha^2\epsilon[w_2, v_2] + \cdots\,. \tag{2.14}$$

Substituting these expansions into the system (2.7a) - (2.7e), the leading order expressions take the form:

$$\zeta_1 = A(s,\tau)\phi(z)\,, \tag{2.15a}$$
$$u_1 = A\{W\phi\}_z\,, \tag{2.15b}$$
$$w_1 = -A_s W\phi\,, \tag{2.15c}$$
$$p_1 = \rho_0 A W^2 \phi_z\,, \tag{2.15d}$$
$$g\rho_1 = \rho_0 N^2 \zeta_1\,, \tag{2.15e}$$
$$v_1 = \tilde{f} B\Phi\,, \quad \rho_0 W\Phi = \rho_0 W\phi_z - (\rho_0 u_0)_z\phi\,, \quad B_s = A\,, \tag{2.15f}$$

where the modal function $\phi(z)$ satisfies the equations (2.11a)-(2.11c).

By collecting terms of second order, the following set of equations is obtained:

$$\begin{aligned}\rho_0(-Wu_{2s} + u_{0z}w_2) + p_{2s} &= -\rho_0(u_{1\tau} + u_1u_{1s} + w_1u_{1z}) + \\ &\quad \rho_1(Wu_{1s} - u_{0z}w_1) + \rho_0\tilde{f}v_1, \end{aligned}\tag{2.16a}$$
$$\begin{aligned}\rho_0(\tilde{f}u_2 - Wv_{2s}) + \rho_2\tilde{f}u_0 &= -\rho_0(v_{1\tau} + u_1v_{1s} + w_1v_{1z}) + \\ &\quad \rho_1 Wv_{1s} - \rho_1\tilde{f}u_1\,, \end{aligned}\tag{2.16b}$$
$$p_{2z} + g\rho_2 = \rho_0 W w_{1s}\,, \tag{2.16c}$$
$$-gW\rho_{2s} - \rho_0 N^2 w_2 = -g(\rho_{1\tau} + u_1\rho_{1s} + w_1\rho_{1z})\,, \tag{2.16d}$$
$$u_{2s} + w_{2z} = 0\,, \tag{2.16e}$$
$$W\zeta_{2s} + w_2 = \zeta_{1\tau} + u_1\zeta_{1s} + w_1\zeta_{1z}\,. \tag{2.16f}$$

Equations (2.16a), (2.16c) and (2.16e) respectively imply that:

$$\begin{aligned}p_{2s} &= -\rho_0(u_{1\tau} + u_1u_{1s} + w_1u_{1z}) + \rho_1(Wu_{1s} - u_{0z}w_1) + \rho_0\tilde{f}v_1 \\ &\quad -\rho_0(-Wu_{2s} + u_{0z}w_2)\,, \end{aligned}\tag{2.17}$$
$$g\rho_2 = \rho_0 W w_{1s} - p_{2z}\,, \tag{2.18}$$
$$u_{2s} = -w_{2z}\,. \tag{2.19}$$

Substituting (2.18) into (2.16d), using the fact that $(p_{2z})_s = (p_{2s})_z$, and equations (2.17) and (2.19), it can be shown that

$$\begin{aligned} &-W(\rho_0(-Ww_{2z} - u_{0z}w_2))_z + \rho_0 N^2 w_2 = g(\rho_{1\tau} + u_1 p_{1s} + w_1\rho_{1z}) \\ &-\rho_0 W^2 w_{1ss} - W(\rho_0(u_{1\tau} + u_1u_{1s} + w_1u_{1z}) - \rho_1(Wu_{1s} - u_{0z}w_1) - \rho_0\tilde{f}v_1)_z\,. \end{aligned} \tag{2.20}$$

Then, it is necessary to obtain w_2 from $w = \zeta_t + (u_0 + u)\zeta_x + w\zeta_z$ and also $w = \alpha\epsilon w_1 + \alpha^2\epsilon w_2 + \cdots$ and therefore, by equating these two expressions for w, the following equation is obtained:

$$\begin{aligned} \alpha\epsilon w_1 + \alpha^2\epsilon w_2 \;=\; & \epsilon(u_0 - c)(\alpha\zeta_{1s} + \alpha^2\zeta_{2s} + \cdots) + \alpha\epsilon(\alpha\zeta_{1\tau} + \alpha^2\zeta_{2\tau} + \cdots) \\ & +\epsilon(\alpha u_1 + \alpha^2 u_2 + \cdots)(\alpha\zeta_{1s} + \alpha^2\zeta_{2s} + \cdots) \\ & +(\alpha\epsilon w_1 + \alpha^2\epsilon w_2 + \cdots)(\alpha\zeta_{1z} + \alpha^2\zeta_{2z} + \cdots). \end{aligned}$$

Collecting terms of order $\alpha^2\epsilon$, it can be shown that

$$w_2 = -W\zeta_{2s} + \zeta_{1\tau} + u_1\zeta_{1s} + w_1\zeta_{1z}. \tag{2.21}$$

Substituting equation (2.21) and solutions obtained for u_1, w_1, ρ_1, p_1 and ζ_1 which are obtained from (2.15) into (2.20), the following is obtained:

$$\{\rho_0 W^2\zeta_{2sz}\}_z + \rho_0 N^2\zeta_{2s} = J_2 \quad \text{at} \quad -h < z < 0\,, \tag{2.22}$$

where J_2 is an expression containing terms in $A(s,\tau)$, derivatives of $A(s,\tau)$ and the modal function, $\phi(z)$, given by:

$$\begin{aligned} J_2 \;&=\; 2\{\rho_0 W\phi_z\}_z A_\tau - \rho_0 W^2\phi A_{sss} + C_1 A A_s - \tilde{f}^2\{B\rho_0\Phi\}_z\,, \\ \text{with}\quad C_1 \;&=\; \{3\rho_0 W^2{\phi_z}^2\}_z + 2\{\rho_0 W^2\phi_z\}_z\phi_z - 2\{\rho_0 W^2(\phi\phi_z)\}_z\,. \end{aligned} \tag{2.23}$$

Note that Φ and B are defined in (2.15f). The corresponding boundary conditions, (2.8a)-(2.8c) and (2.10) are treated in analogous manner to the second order,

yielding:

$$w_2 = 0 \quad \text{at} \quad z = -h\,, \tag{2.24}$$

$$p_2 - \rho_0 g\eta_2 + p_{1z}\eta_1 - \frac{1}{2}\rho_{0z} g\eta_1^2 = 0 \quad \text{at} \quad z = 0\,, \tag{2.25}$$

$$w_2 + w_{1z}\eta_1 - \eta_{1\tau} + W\eta_{2s} - u_{0z}\eta_1\eta_{1s} - u_1\eta_{1s} = 0 \quad \text{at} \quad z = 0\,, \tag{2.26}$$

$$\zeta_2 + \zeta_{1z}\eta_1 - \eta_2 = 0 \quad \text{at} \quad z = 0\,. \tag{2.27}$$

The corresponding boundary condition to (2.24) is:

$$\zeta_{2s} = 0 \quad \text{at} \quad z = -h. \tag{2.28}$$

Then, it is necessary to differentiate (2.25) with respect to s in order to use (2.17),(2.19),(2.21) to obtain the following equation:

$$\rho_0 W^2 \zeta_{2sz} - \rho_0 g\zeta_{2s} = K_2 \quad \text{at} \quad z = 0\,, \tag{2.29}$$

where K_2 is known and given by:

$$K_2 = 2\rho_0 W\phi_z A_\tau + \{3\rho_0 W^2\phi_z^2 - 2\rho_0 W^2\phi\phi_{zz}\}AA_s + \tilde{f}^2 B\rho_0\Phi\,. \tag{2.30}$$

Hence, there are three equations which need to be satisfied by ζ_2, namely equations (2.22),(2.28) and (2.29). The left hand sides of these equations are identical to the boundary value problem in (2.11a - 2.11c), which are used to define the modal function $\phi(z)$ and hence can be solved only if a certain compatibility condition is satisfied. The required compatibility condition is that the inhomogenous terms in (2.22) and (2.29) should be orthogonal to the solution of the adjoint of the modal equations (2.11a) and (2.11c). To obtain this compatibility condition, we define the linear operator $\mathcal{L}$:

$$\mathcal{L}(\phi) = \{\rho_0 W^2\phi_z\}_z + \rho_0 N^2\phi\,, \tag{2.31}$$

where $W = c - u_0$. Then, we consider a pair of functions ζ_{2s} and ϕ satisfying the

boundary condition on the bottom (2.28) of the problem ($\zeta_{2s} = 0$ and $\phi = 0$ at $z = -h$) and also satisfying

$$\int_{-h}^{z} \{\zeta_{2s}\mathcal{L}(\phi) - \phi\mathcal{L}(\zeta_{2s})\}dz = \rho_0 W^2(\zeta_{2s}\phi_z - \phi\zeta_{2sz})\,. \tag{2.32}$$

Now we have a solution of equation (2.22) for ζ_{2s}, so that

$$\phi\mathcal{L}(\zeta_{2s}) - \zeta_{2s}\mathcal{L}(\phi) = \phi J_2\,. \tag{2.33}$$

We substitute this into (2.29) and apply at the free surface at $z = 0$. By recalling that $\rho_0 W^2\phi_z = \rho_0 g\phi$ at $z = 0$, finally we will obtain the compatibility condition as

$$\int_{-h}^{0} J_2\phi\ dz = [K_2\phi]_{z=0}\,. \tag{2.34}$$

Then, the substitution of expressions of J_2 and K_2 into (2.34), gives the following governing evolution equation of weakly-nonlinear, long internal waves known as the Ostrovsky equation [17, 24, 25, 26] (this derivations did not include the shear flow):

$$A_\tau + \nu AA_s + \lambda A_{sss} = \gamma B\,, \tag{2.35}$$

where $B(s,\tau)_s = A(s,\tau)$ and $A(s,\tau)$ is the wave amplitude. The coefficients μ, λ and γ are parameters of terms representing nonlinearity, dispersion and rotation, respectively. They are found in the expressions involving the modal function and background density stratification, which are presented in the form:

$$I\nu = 3\int_{-h}^{0} \rho_0 W^2\phi_z^3 dz\,, \quad I\lambda = \int_{-h}^{0} \rho_0 W^2\phi^2\,dz\,, \quad I\gamma = \tilde{f}^2\int_{-h}^{0} \rho_0\Phi\phi_z\,dz\,, \tag{2.36}$$

where I is given by:

$$I = 2\int_{-h}^{0} \rho_0 W\phi_z^2\,dz\,.$$

The Ostrovsky equation (2.46) holds two conservation laws for the localised solutions:

$$\int_{-\infty}^{\infty} A\, ds = 0 \quad \text{and} \tag{2.37}$$

$$\frac{\partial}{\partial \tau} \int_{-\infty}^{\infty} A^2\, ds = 0\,. \tag{2.38}$$

Note that (2.37) is a zero mass condition, and when A is localised, then B also satisfies zero mean condition. The second conservation law (2.38), expresses momentum conservation.

2.3 Soliton solutions of the KdV equation

The KdV equation

$$A_t + \nu A A_x + \lambda A_{xxx} = 0\,, \tag{2.39}$$

is widely recognised as a model of weakly nonlinear long waves. The coefficients ν and λ represent the nonlinear and dispersion effects, respectively. The nonlinear effect causes the steepening of waveform, while the dispersion effect makes the waveform spread. Due to a balance between these two effects, a solitary wave solution arises and is given by

$$A(x,t) = a\ \mathrm{sech}^2(k(x-ct)), \quad c = \frac{\nu a}{3} = 4\lambda k^2. \tag{2.40}$$

Note that the speed c is proportional to the wave amplitude a, or to the square of the wavenumber k^2, which means that the solitary waves propagate with a speed that increases with the amplitude of the waves. Hence, the larger amplitude waves are narrower and travel faster than smaller ones. A soliton is a solitary wave that behave like a 'particle' and satisfies the following conditions:

1. A soliton must maintain its shape when it propagates at a constant speed .

2. When two soliton interact, they retain their shapes and speeds. The only result of interaction is a phase shift .

This solitary wave solution found by Korteweg and de Vries had earlier been obtained directly from the governing equations independently by Boussinesq (1871, 1877) and Rayleigh (1876) who were motivated to explain a very well-known observations and experiments of Russell (1844). The linear dispersion relation of the KdV equation for the phase velocity $c_p = \omega/k$ and the group velocity c_g are given by:

$$c_p = -\lambda k^2 \,, \quad c_g = \frac{dw}{dk} = -3\lambda k^2 \,, \tag{2.41}$$

as shown in blue curve in Figure 2.2 when $\lambda = 1$. The graph of the phase velocity of the KdV equation shows that there is a gap in the spectrum for all $c_p > 0$ where solitary waves can exist. An example of a typical solution of the KdV equation (2.39) for a localised initial condition leads to the generation of a finite number of solitary waves and some dispersive radiation, see Figure 2.3.

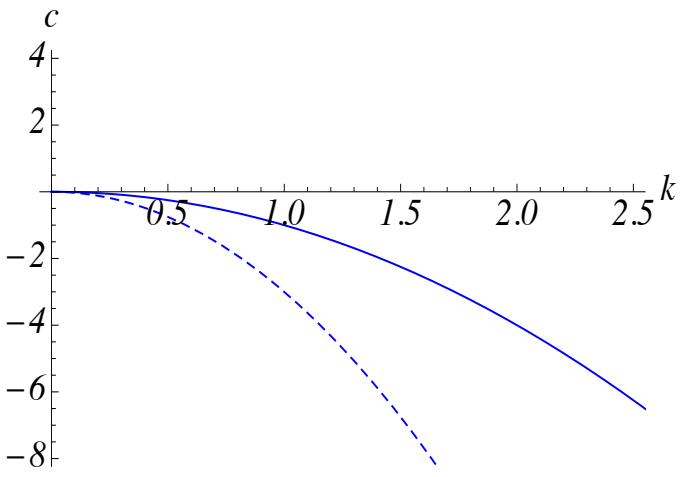

FIGURE 2.2: Phase (solid curve) and group (dashed curve) velocities of the KdV equation.

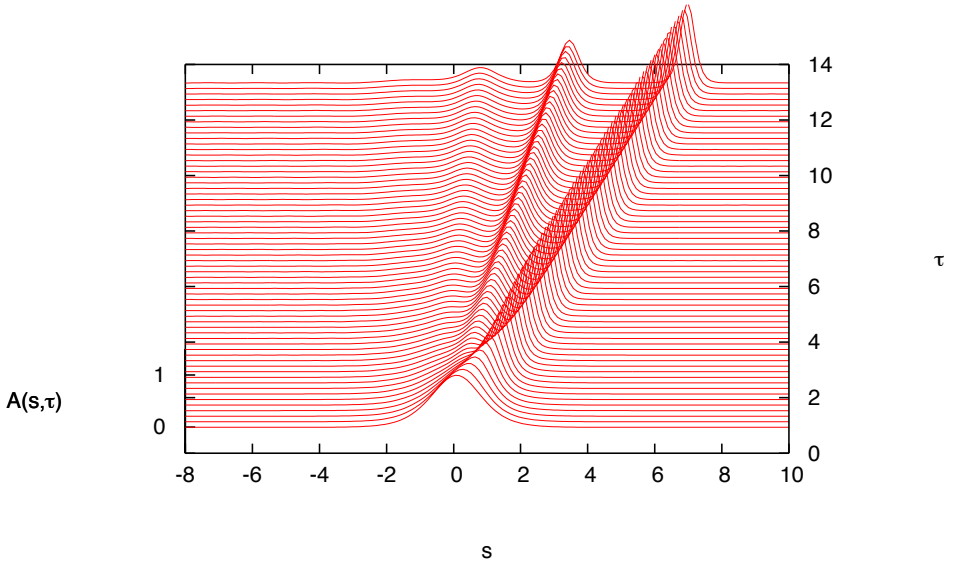

FIGURE 2.3: A typical solution of the KdV equation (2.39) when $\nu = 1$ and $\lambda = 0.01$ commencing with $A(x,0) = \text{sech}^2(x)$. Here three solitary waves have been generated, of which the two largest are clearly visible.

The KdV equation can be written as a conservation law:

$$\partial_t A = -\partial_x (A_{xx} + \frac{1}{2}A^2)\,, \tag{2.42}$$

and so u is a conserved density. In fact there are more conserved densities, three relevant conserved densities are given below. The integrability of the KdV equation is also characterised by the existence of an infinite set of independent conservation laws. The first three are

$$\int_{-\infty}^{\infty} A\,dx = \text{constant}\,, \tag{2.43}$$

$$\int_{-\infty}^{\infty} A^2\,dx = \text{constant}\,, \tag{2.44}$$

$$\int_{-\infty}^{\infty} A^3 - \frac{1}{2}A_x^2\,dx = \text{constant}\,, \tag{2.45}$$

which are related with the conservation of mass, momentum and energy, respectively. Indeed (2.43) is obtained from the KdV equation (2.39) by integrating over

x, while (2.44, 2.45) are obtained in an analogous manner after first multiplying (2.39) by A, A^2, respectively (see, for example, Ablowitz and Segur [46]).

2.4 Wave packet solutions of the Ostrovsky equation

As discussed before, in the weakly nonlinear long wave limit, oceanic internal solitary waves for the single linear long wave mode are described by the well-known KdV equation, extended to the Ostrovsky equation in the presence of the Earth's background rotation. Thus, the Ostrovsky equation is

$$A_\tau + \nu A A_s + \lambda A_{sss} = \gamma B\,. \tag{2.46}$$

The effect of the Earth's background rotation for the time evolution of the internal wave becomes important when the wave propagates for several inertial periods. Although this effect is small for an individual wave, but it is significant for the wave evolution [33]. The background rotation is represented by the coefficient γ, which in the absence of shear flow is given by

$$\gamma = \frac{\tilde{f}^2}{2c}\,, \tag{2.47}$$

where f is the Coriolis parameter. For oceanic internal waves $\lambda\gamma > 0$, it is known that the Ostrovsky equation does not support steady solitary wave solutions of the KdV equation, see Grimshaw and Helfrich [34] and the references therein. Strictly speaking, if $\gamma \neq 0$, but sufficiently small, $\gamma << 1$, then the soliton solution (2.40) is no longer valid. Recently, it was established that the long-time effect of rotation is the destruction of the initial internal solitary wave through the terminal radiation damping, and the eventual emergence of a coherent steadily propagating nonlinear wave packet, see Grimshaw and Helfrich [1], Helfrich [33] and Grimshaw and Helfrich [34]. It is worth noting that the same phenomenon was observed independently in Daisuke and Takuji [35] in the context of waves in solids. Indeed,

the discrete model in Daisuke and Takuji [35] can be related to the two-directional generalisation of the Ostrovsky equation derived in Gerkema [41].

Indeed, the linear dispersion relation of the Ostrovsky equation for sinusoidal waves of frequency ω and wavenumber k, for the phase velocity $c_p = \omega/k$ and the group velocity c_g are given by:

$$c_p = \frac{\gamma}{k^2} - \lambda k^2\,, \quad c_g = \frac{dw}{dk} = -\frac{\gamma}{k^2} - 3\lambda k^2. \tag{2.48}$$

It is important to note that the group velocity c_g is negative for all wavenumbers k, and then has a local maximum at finite wavenumber when $dc_g/dk = 0$ at $k = k_c$ where $3\lambda k_c^4 = \gamma$. The local maximum is $c_{gm} = -2\gamma/k_c^2 = -2\sqrt{3\gamma\lambda}$.

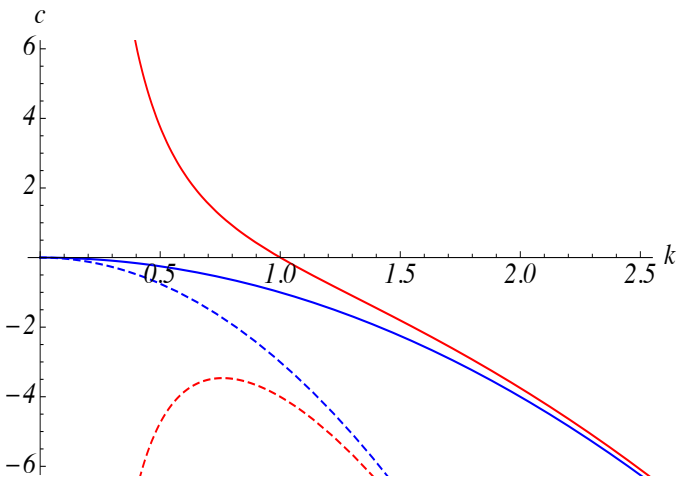

FIGURE 2.4: Phase (solid curves) and group (dashed curves) velocities of the KdV (blue) and Ostrovsky (red) equations.

The blue curve in Figure 2.4 shows the phase velocity of the KdV equation ($\gamma = 0$, $\lambda = 1$) as in Figure 2.2 and the red curve shows the phase velocity of the Ostrovsky equation ($\gamma = \lambda = 1$). The additional term on the right hand side of Ostrovsky equation is a linear long-wave perturbation to the KdV equation, and it has the ability of removing the spectral gap on which solitary waves exist for the KdV equation, as shown in the red curve. Hence no solitary waves are expected to occur when there is no shear flow since then $\lambda\gamma > 0$ for internal waves.

Grimshaw and Helfrich [34] provide mathematical evidence to show that the Ostrovsky equation with $\lambda\gamma > 0$ has no steady solitary wave solutions. The proof of the non-existence of solitary waves also was given in Leonov [30] and Galkin and Stepanyants [47]. In the opposite case when $\lambda\gamma < 0$, which can arise in other physical applications, solitary waves do exist, see Obregon and Stepanyants [28]. Several studies from Grimshaw and Helfrich [1], Helfrich [33], Grimshaw et al. [48] have revealed that the long-time effect of background rotation is the decay of the initial internal solitary wave into the trailing radiating waves, and eventually a coherent steadily propagating nonlinear wave packet emerges with the maximum value of the group velocity c_{gm} with a carrier wavenumber k_c.

An example of the numerical solution of the Ostrovsky equation for the initial KdV solitary wave with the amplitude $a = 32$ and all coefficients in (2.46) equal to unity is given in Figure 2.5. It can be seen that an initial solitary wave rapidly decays into the radiation of inertia-gravity waves and eventually forms a nonlinear envelope wave packet. Numerical experiments have been performed by Grimshaw and Helfrich [1], who run the simulation with amplitude a between 2 and 32. Notice that for the small amplitudes $a = 2$ and 4, the packet does not completely separate from the trailing radiation. However, the larger amplitudes $a = 8, 16$ and 32 illustrate that the separation of the packet is clear, whether it was a steady or nearly steady state.

We solve the Ostrovsky equation (2.46) numerically using the pseudo-spectral method, which uses a Fourier transform treatment of the space dependence. The numerical results are in agreement with the known experiment [1].

2.5 Conclusion

In this chapter we performed the systematic derivation of the Ostrovsky equation from the full set of Euler equations with the boundary conditions corresponding to the oceanic applications by using the multiple scale expansion method. The Ostrovsky equation is formulated on the assumption that only single vertical mode

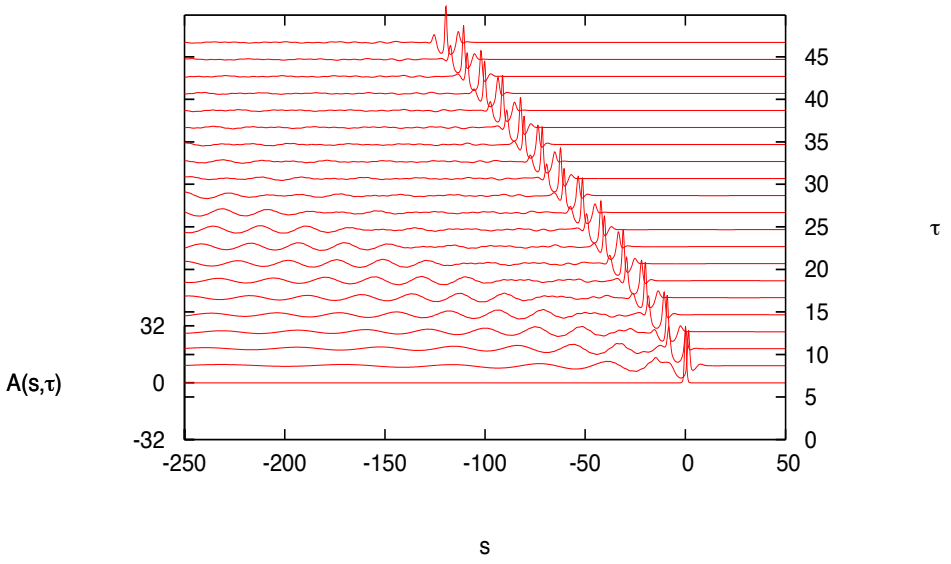

FIGURE 2.5: Numerical solution of the Ostrovsky equation for an initial condition given by a KdV solitary wave with amplitude $a = 32$, the same as in [1]. Note that only the interval containing the wave packet is shown.

is used. The Ostrovsky equation is an extension of the KdV equation in the presence of background rotation describing the weakly nonlinear oceanic internal waves for a single linear long wave mode. The characteristic feature of the KdV model is the solitary wave and for the Ostrovsky equation is the nonlinear wave packet. The Ostrovsky equation in the absence of a shear flow does not support solitary wave solutions, and instead a solitary-like initial condition collapses due to radiation of inertia gravity waves, with the long time outcome being a nonlinear wave packet (shear flow can lead to $\lambda\gamma < 0$, see Appendix A). In another situation, when two vertical modes are used, due to a near-resonance between their respective linear long wave phase speeds is described by a system of two coupled Ostrovsky equations. The derivation of the coupled Ostrovsky equation will be discussed in the next chapter.

Chapter 3

Coupled Ostrovsky equations

3.1 Introduction

It is known that for internal waves it is possible for the phase speeds of different modes to be nearly coincident, and then there will be a resonant transfer of energy between the waves, see Eckart [38]. In this case, the KdV equation is replaced by two coupled KdV equations, describing a strong interaction between internal solitary waves of different modes, see Gear and Grimshaw [39] and Grimshaw [40]. Various families of solitary waves are supported by coupled KdV equations depending on the structure of the linear dispersion relation, namely pure solitary waves, generalised solitary waves and envelope solitary waves, see the review Grimshaw [40].

This chapter is devoted to an outline of the derivation of a new model of a pair of coupled Ostrovsky equations describing internal waves in the rotating ocean. The derivation is an extension of the Gear and Grimshaw [39] work, which however did not included a shear flow and used Lagrangian variables. The system of coupled Ostrovsky equation is systematically derived in Eulerian variables from the complete set of fluid equations of motion for an inviscid, incompressible density-stratified fluid with a shear flow and boundary conditions appropriate to an oceanic situation, see Alias et al. [49]. The coupled Ostrovsky equations were also derived

in the context of waves in layered elastic waveguides, see Khusnutdinova et al. [42], Khusnutdinova and Moore [43]. Thus, this model belongs to the class of canonical mathematical models of nonlinear wave theory, inviting a detailed study of the dynamics of its solutions.

The coupled Ostrovsky equations are given by

$$I_1(A_{1\tau} + \mu_1 A_1 A_{1s} + \lambda_1 A_{1sss} - \gamma_1 B_1) + \nu_1 [A_1 A_2]_s + \nu_2 A_2 A_{2s} + \lambda_{12} A_{2sss} - \gamma_{12} B_2 = 0\,, \tag{3.1}$$

$$I_2(A_{2\tau} + \mu_2 A_2 A_{2s} + \lambda_2 A_{2sss} + \Delta A_{2s} - \gamma_2 B_2) + \nu_2 [A_1 A_2]_s + \nu_1 A_1 A_{1s} + \lambda_{21} A_{1sss} - \gamma_{21} B_1 = 0\,, \tag{3.2}$$

where $B_{i_s} = A_i$ with $i = 1, 2$ and each equation has both linear and nonlinear coupling terms. Equations (3.1, 3.2) are automatically reduced to the coupled KdV equations in the absence of rotation terms, γ_1 and γ_2. The full formulas are defined in equations (3.28a - 3.28h).

3.2 Formulation and Asymptotic derivation

Overall, the derivation of coupled Ostrovsky equations follows a similar strategy to the derivation of the coupled KdV equations. At the leading linear long wave order, and in the absence of any rotation, the solution for ζ is given by an expression of the form $A(x - ct)\phi(z)$ where the modal function is given by (2.11a). In general there is an infinite set of solutions for $[\phi(z), c]$ [2]. Here, we extend the derivation of the Ostrovsky equation from Chapter 2. When all speeds of the modes are distinct $c_1 \neq c_2$, then the asymptotic expansion can proceed for each mode separately, yielding a single Ostrovsky equation for each mode [17, 24, 25]. This is known as the weak interaction scenario. Here, instead, we are concerned with the case when there are two modes with nearly coincident speeds $c_1 = c$ and $c_2 = c + \epsilon^2\Delta$, $\epsilon \ll 1$, where Δ is the detuning parameter. Importantly, the modal functions $\phi_1(z), \phi_2(z)$

are *distinct*, and each satisfy the system (2.11a), that is:

$$(\rho_0 W_i^2 \phi_{iz})_z + \rho_0 N^2 \phi_i = 0\,, \quad i = 1, 2 \tag{3.3}$$

$$\phi_i = 0 \quad \text{at} \quad z = -h\,, \quad \text{and} \quad W_i^2 \phi_{iz} = g\phi_i \quad \text{at} \quad z = 0\,. \tag{3.4}$$

Here $W_i = c_i - u_0(z)$ where c_i is the long wave speed corresponding to the mode $\phi_i(z), i = 1, 2$.

It is readily shown from the two modal systems (3.3), (3.4) that:

$$\int_{-h}^{0} \rho_0 (W_1^2 - W_2^2) \phi_{1z} \phi_{2z} dz = 0\,,$$

by multiplying (3.3) for $i = 1$ by $\phi_2(z)$ and for $i = 2$ by $\phi_1(z)$, subtracting and then integrating them from $-h$ to 0 using integration by parts and the boundary conditions (3.4). Since in general $W_1 - W_2 = c_1 - c_2 \neq 0$, it follows that the two modes satisfy an orthogonality condition:

$$\int_{-h}^{0} \rho_0 [c_1 + c_2 - 2u_0] \phi_{1z} \phi_{2z}\, dz = 0\,, \quad \text{so that} \quad \int_{-h}^{0} \rho_0 W \phi_{1z} \phi_{2z}\, dz \approx 0\,. \tag{3.5}$$

Note that here, and in the sequel, $W_i = W = c - u_0(z)$ with an error of the order ϵ^2.

Next, by using the same scaled variables as for the single mode:

$$\tau = \epsilon \alpha t\,, \quad s = \epsilon (x - ct)\,, \quad f = \alpha \tilde{f}\,, \tag{3.6}$$

where $\alpha = \epsilon^2$, we seek a solution in the form of asymptotic multiple-scales expansions:

$$[\zeta, u, \rho, p] = \alpha [\zeta_1, u_1, \rho_1, p_1] + \alpha^2 [\zeta_2, u_2, \rho_2, p_2] + \cdots\,, \tag{3.7}$$

$$[w, v] = \alpha\epsilon [w_1, v_1] + \alpha^2 \epsilon [w_2, v_2] + \cdots\,. \tag{3.8}$$

Substituting these expansions into the system (2.7a) - (2.7e), at the leading order we obtain the following set of equations:

$$\rho_0(-Wu_{1s} + u_{0z}w_1) + p_{1s} = 0\,, \tag{3.9}$$

$$\rho_0(\tilde{f}u_1 - Wv_{1s}) + \rho_1\tilde{f}u_0 = 0\,, \tag{3.10}$$

$$p_{1z} + g\rho_1 = 0\,, \tag{3.11}$$

$$-gW\rho_{1s} - \rho_0 N^2 w_1 = 0\,, \tag{3.12}$$

$$u_{1s} + w_{1z} = 0\,, \tag{3.13}$$

$$W\zeta_{1s} + w_1 = 0\,. \tag{3.14}$$

Note that by assuming that two waves are present at the leading order, the following are obtained:

$$\zeta_1 = A_1(s,\tau)\phi_1(z) + A_2(s,\tau)\phi_2(z)\,, \tag{3.15a}$$

$$u_1 = A_1\{W\phi_1\}_z + A_2\{W\phi_2\}_z\,, \tag{3.15b}$$

$$w_1 = -A_{1s}W\phi_1 - A_{2s}W\phi_2\,, \tag{3.15c}$$

$$p_1 = \rho_0 A_1 W^2\phi_{1z} + \rho_0 A_2 W^2\phi_{2z}\,, \tag{3.15d}$$

$$g\rho_1 = \rho_0 N^2\zeta_1\,, \tag{3.15e}$$

$$v_1 = \tilde{f}(B_1\Phi_1 + B_2\Phi_2)\,. \tag{3.15f}$$

where, $\rho_0 W\Phi_{1,2} = \rho_0 W\phi_{1z,2z} - (\rho_0 u_0)_z\phi_{1,2}$ and $B_{1s,2s} = A_{1,2}$. Vitally, the exact solution of the linearised equations should contain the exact expressions W_1 and W_2 in the terms related to the first and second waves, respectively, rather than just W. In fact, $W_1 = W$ through the choice of $c_1 = c$, but there is an $O(\epsilon^2)$ difference between W_2 and W since $c_2 = c + \epsilon^2\Delta$. This difference between the exact and leading order solutions necessitates the introduction of correction terms at the next order, in order to recover the distinct modal equations for the functions ϕ_1 and ϕ_2.

By collecting terms of the second order for each equation, and calculating the correction terms originating from the leading order, the following set of equations

are obtained:

$$\begin{aligned}
\rho_0(-Wu_{2s}+u_{0z}w_2)+p_{2s} &= -\rho_0(u_{1\tau}+u_1u_{1s}+w_1u_{1z}) \\
&\quad +\rho_1(Wu_{1s}-u_{0z}w_1)+\rho_0\tilde{f}v_1, && \text{(3.16a)}\\
\rho_0(\tilde{f}u_2-Wv_{2s})+\rho_2\tilde{f}u_0 &= -\rho_0(v_{1\tau}+u_1v_{1s}+w_1v_{1z}) \\
&\quad +\rho_1Wv_{1s}-\rho_1\tilde{f}u_1\,, && \text{(3.16b)}\\
p_{2z}+g\rho_2 &= \rho_0Ww_{1s}+2\Delta A_2\{\rho_0W\phi_{2z}\}_z\,, && \text{(3.16c)}\\
-gW\rho_{2s}-\rho_0N^2w_2 &= -g(\rho_{1\tau}+u_1\rho_{1s}+w_1\rho_{1z})\,, && \text{(3.16d)}\\
u_{2s}+w_{2z} &= 0\,, && \text{(3.16e)}\\
W\zeta_{2s}+w_2 &= \zeta_{1\tau}+u_1\zeta_{1s}+w_1\zeta_{1z}\,. && \text{(3.16f)}
\end{aligned}$$

Here, the extra term proportional to A_2 in (3.16c) comes from the afore-mentioned difference between W_2 and W in the leading order pressure term (3.15d) creating in effect a contribution to p_1. There is no analogous term in (3.16a) as there is a cancellation between the corrections to u_1 and p_1. The boundary conditions (2.8a) - (2.8c), (2.10) are treated in analogous manner to yield:

$$w_2=0 \quad \text{at} \quad z=-h\,, \tag{3.17}$$

$$p_2-\rho_0g\eta_2+p_{1z}\eta_1-\frac{1}{2}\rho_{0z}g\eta_1^2-2\Delta\rho_0W\phi_{2z}A_2=0 \quad \text{at} \quad z=0\,, \tag{3.18}$$

$$w_2+w_{1z}\eta_1-\eta_{1\tau}+W\eta_{2s}-u_{0z}\eta_1\eta_{1s}-u_1\eta_{1s}=0 \quad \text{at} \quad z=0\,, \tag{3.19}$$

$$\zeta_2+\zeta_{1z}\eta_1-\eta_2=0 \quad \text{at} \quad z=0\,. \tag{3.20}$$

Eliminating all variables in favour of ζ_2 yields:

$$\{\rho_0W^2\zeta_{2sz}\}_z+\rho_0N^2\zeta_{2s}=M_2 \quad \text{at} \quad -h<z<0\,, \tag{3.21}$$

$$\zeta_2=0 \quad \text{at} \quad z=-h\,, \quad \rho_0W^2\zeta_{2sz}-\rho_0g\zeta_{2s}=N_2 \quad \text{at} \quad z=0\,, \tag{3.22}$$

where M_2, N_2 are known expressions containing terms in A_i and their derivatives. The expression for M_2 in (3.21) is given by

$$M_2=M_2^1+M_2^2+M^{12}[A_1A_2]_s+2\{\rho_0W\phi_{2z}\}_z\Delta A_{2s}-\tilde{f}^2\{B_1\rho_0\Phi_1+B_2\rho_0\Phi_2\}_z\,, \tag{3.23}$$

where

$$\begin{aligned} M_2^j &= 2\{\rho_0 W\phi_{jz}\}_z A_{j\tau} - \rho_0 W^2\phi_j A_{jsss} + (3\{\rho_0 W^2 {\phi_{jz}}^2\}_z \\ &\quad +2\{\rho_0 W^2\phi_{jz}\}_z\phi_{jz} - 2\{\rho_0 W^2(\phi_j\phi_{jz})_z\}_z)AA_{js}\,, \quad j=1,2, \\ M^{12} &= 3\{\rho_0 W^2\phi_{1z}\phi_{2z}\}_z - \rho_0 W^2(\phi_{1z}\phi_{2zz}+\phi_{2z}\phi_{1zz}) \\ &\quad -\{\rho_0 W^2(\phi_1\phi_{2zz}+\phi_2\phi_{1zz})\}_z\,. \end{aligned}$$

Similarly, the expression for N_2 in (3.22) is given by

$$N_2 = N_2^1 + N_2^2 + N^{12}[A_1A_2]_s + 2\rho_0 W\phi_{2z}\Delta A_{2s} - \tilde{f}^2\{B_1\rho_0\Phi_1 + B_2\rho_0\Phi_2\}\,, \quad (3.24)$$

where

$$\begin{aligned} N_2^j &= 2\rho_0 W\phi_{jz}A_{j\tau} + (3\rho_0 W^2\phi_{jz}^2 - 2\rho_0 W^2\phi_j\phi_{jzz})A_jA_{js}\,, \quad j=1,2\,, \\ N^{12} &= 3\rho_0 W^2\phi_{1z}\phi_{2z} - \rho_0 W^2(\phi_1\phi_{2zz}+\phi_2\phi_{1zz}). \end{aligned}$$

Here, we need two compatibility conditions for coupled modes to be imposed on the system (3.21), (3.22), given by

$$\int_{-h}^{0} M_2\phi_{1,2}\,dz - [N_2\phi_{1,2}]_{z=0} = 0\,, \quad (3.25)$$

where $\phi_{1,2}$ are evaluated at the leading order. As a result, these compatibility conditions lead to the coupled Ostrovsky equations:

$$\begin{aligned} &I_1(A_{1\tau} + \mu_1 A_1A_{1s} + \lambda_1 A_{1sss} - \gamma_1 B_1) \\ &\qquad +\nu_1[A_1A_2]_s + \nu_2 A_2A_{2s} + \lambda_{12}A_{2sss} - \gamma_{12}B_2 = 0\,, \quad (3.26) \\ &I_2(A_{2\tau} + \mu_2 A_2A_{2s} + \lambda_2 A_{2sss} + \Delta A_{2s} - \gamma_2 B_2) \\ &\qquad +\nu_2[A_1A_2]_s + \nu_1 A_1A_{1s} + \lambda_{21}A_{1sss} - \gamma_{21}B_1 = 0\,, \quad (3.27) \end{aligned}$$

where $B_{1s} = A_1, B_{2s} = A_2$, and the coefficients are given by

$$I_i\mu_i = 3\int_{-h}^{0} \rho_0 W^2 \phi_{i_z}^3 \, dz \,, \tag{3.28a}$$

$$I_i\lambda_i = \int_{-h}^{0} \rho_0 W^2 \phi_i{}^2 \, dz \,, \tag{3.28b}$$

$$I_i = 2\int_{-h}^{0} \rho_0 W \phi_{i_z}^2 \, dz \,, \tag{3.28c}$$

$$\lambda_{12} = \lambda_{21} = \int_{-h}^{0} \rho_0 W^2 \phi_1 \phi_2 \, dz \,, \tag{3.28d}$$

$$\nu_1 = 3\int_{-h}^{0} \rho_0 W^2 \phi_{1z}^2 \phi_{2z} \, dz \,, \tag{3.28e}$$

$$\nu_2 = 3\int_{-h}^{0} \rho_0 W^2 \phi_{2z}^2 \phi_{1z} \, dz \,, \tag{3.28f}$$

$$I_i\gamma_i = \tilde{f}^2 \int_{-h}^{0} \rho_0 \Phi_i \phi_{iz} \, dz \,, \tag{3.28g}$$

$$\gamma_{ij} = \tilde{f}^2 \int_{-h}^{0} \rho_0 \Phi_i \phi_{jz} \, dz \,. \tag{3.28h}$$

Here $i, j = 1, 2$. If there is no shear flow, that is $u_0 = 0$, then $\gamma_1 = \gamma_2 = \tilde{f}^2/2c$ and $\gamma_{12} = \gamma_{21} = 0$. Also note the Cauchy-Schwartz inequality $\lambda_{12}^2 < I_1 I_2 \lambda_1 \lambda_2$, which is readily shown by considering $\int_{-h}^{0} \rho_0 W^2 (x\phi_1 + y\phi_2)^2 \, dz > 0$ for all real x, y. Thus $x^2 I_1 \lambda_1 + 2xy\lambda_{12} + y^2 I_2 \lambda_2 > 0$, for all real x, y and so $\lambda_{12}^2 < I_1 I_2 \lambda_1 \lambda_2$.

When, there is no Earth's rotation, this system reduces to two coupled KdV equations, see Gear and Grimshaw [39] for the derivation in the absence of a shear flow. For the coupled KdV equation, Grimshaw and Gerard [50] predicted that there exist three possible families of solitary waves namely pure solitary waves, generalised solitary waves and envelope solitary waves depending on the sign of the coefficients $\lambda_{1,2}$ when $\Delta > 0$ without loss of generality and $\gamma_{1,2} > 0$. Detailed studies of the generalised solitary waves have been discussed in Fochesato et al. [51].

3.2.1 Reducing the parameters

The number of parameters in the coupled Ostrovsky equations (3.26) and (3.27) can be reduced. We scale the dependent and independent variables,

$$A_1 = \frac{u}{\mu_1}\,, \quad A_2 = \frac{v}{\mu_2}\,, \quad s = \lambda_1^{1/2} X\,, \quad \tau = \lambda_1^{1/2} T\,, \tag{3.29}$$

assuming that $\lambda_1 > 0, \mu_{1,2} \neq 0$ without loss of generality. We transform the equations (3.26), (3.27) to the form:

$$(u_T + uu_X + u_{XXX} + n(uv)_X + mvv_X + \alpha v_{XXX})_X = \beta u + \gamma v, \tag{3.30}$$

$$(v_T + vv_X + \delta v_{XXX} + \Delta v_X + p(uv)_X + quu_X + \lambda u_{XXX})_X = \mu v + \nu u, \tag{3.31}$$

where

$$\begin{aligned} &n = \frac{\nu_1}{I_1\mu_2}, \quad m = \frac{\mu_1\nu_2}{I_1\mu_2^2}, \quad \alpha = \frac{\lambda_{12}\mu_1}{\lambda_1 I_1\mu_2}, \quad \beta = \gamma_1\lambda_1, \quad \gamma = \frac{\gamma_{12}\mu_1\lambda_1}{I_1\mu_2}, \\ &\delta = \frac{\lambda_2}{\lambda_1}, \quad p = \frac{\nu_2}{I_2\mu_1}, \quad q = \frac{\mu_2\nu_1}{I_2\mu_1^2}, \quad \lambda = \frac{\lambda_{21}\mu_2}{\lambda_1 I_2\mu_1}, \quad \mu = \gamma_2\lambda_1, \quad \nu = \frac{\gamma_{21}\mu_2\lambda_1}{I_2\mu_1} \end{aligned} \tag{3.32}$$

Especially note that:

$$\frac{q}{n} = \frac{p}{m} = \frac{\lambda}{\alpha} = \frac{\gamma_{12}\nu}{\gamma_{21}\gamma} = \frac{I_1\mu_2^2}{I_2\mu_1^2}\,, \quad \frac{\alpha\lambda}{\delta} = \frac{\lambda_{12}^2}{\lambda_1\lambda_2 I_1 I_2} < 1\,. \tag{3.33}$$

Note that the scaled variables u and v, and the coefficient p should not be confused with the velocity components and the pressure.

3.2.2 Conservation laws

The coupled Ostrovsky equations (3.30, 3.31) possess three conservation laws:

$$\int_{-\infty}^{\infty} A_1\, ds = 0\,, \quad \int_{-\infty}^{\infty} A_2\, ds = 0\,, \quad \text{when} \quad I_1 I_2 \gamma_1\gamma_2 - \gamma_{12}\gamma_{21} \neq 0 \tag{3.34}$$

$$\int_{-\infty}^{\infty} [I_1 A_1^2 + I_2 A_2^2]\, ds = \text{constant}\,, \quad \text{when} \quad \gamma_{12} = \gamma_{21}. \tag{3.35}$$

All three hold when there is no shear flow, since then $\gamma_{12} = \gamma_{21} = 0$. Note that when $I_1 I_2 > 0$, then (3.35) guarantees stability in the framework of the coupled equations. But if $I_1 I_2 < 0$, then (3.35) does not constrain the solutions and then indicates possible instability of the coupled equations. Also note that when $I_1 I_2 < 0$, implying there is a critical layer in the background of shear flow, and this also implies that this background shear flow may be linearly unstable. A critical level occurs when $u_0(z) = c$ where $u_0(z)$ is the background shear flow and c is a wave speed. A critical layer is a small zone around the critical level where the usual linearised theory fails.

After the scaling of parameters, the counterparts of the conservation laws are:

$$\int_{-\infty}^{\infty} u\, dX = 0\,, \quad \int_{-\infty}^{\infty} v\, dX = 0\,, \quad \text{when} \quad \beta\mu - \gamma\nu \neq 0\,, \tag{3.36}$$

$$\int_{-\infty}^{\infty} [\lambda u^2 + \alpha v^2]\, dX = \text{constant}\,, \quad \text{when} \quad \gamma_{12} = \gamma_{21}\,, \quad \text{that is} \quad \alpha\nu = \lambda\gamma\,. \tag{3.37}$$

3.3 Conclusion

In this chapter, two coupled Ostrovsky equations are systematically derived for a density-stratified ocean from the full set of Euler equations with the boundary conditions corresponding to the oceanic applications. The asymptotic multiple-scales expansion method was used to perform the derivation. Typically, the initial solitary-like waves are destroyed and replaced by two coupled nonlinear wave packets, propagating usually with distinct speeds, which is discussed in the next chapter. This is the counterpart of the same phenomenon in the single Ostrovsky equation. Using the derived coupled Ostrovsky equations, we now aim to develop a numerical method for solving these equations, with the view to further develop our understanding of the behaviour of nonlinear waves governed by such models.

Chapter 4

Numerical Method

4.1 Introduction

The numerical approach used in the thesis is based on the pseudo-spectral (PS) method, which allows us to solve of the coupled Ostrovsky equations in a periodic domain by means of the discrete Fourier transform. The numerical solution of coupled systems is fascinating and delicate work, and only a few numerical works have been performed for coupled KdV equations. The PS method has been used to solve many nonlinear evolution equations and systems of the KdV type, see Chan and Kerkhoven [52], Canuto et al. [53], Nouri and Sloan [54], Boyd [55], Huang and Zhang [56], Rashid [57], Thomas and Ruo [58], Klein [59], Gulkac and Ozis [60], Rashid and Ismail [61], Yaguchi et al. [62] and references therein. Various numerical codes were developed for the solution of the single Ostrovsky equation, see Grimshaw and Helfrich [1], Grimshaw et al. [26], Gilman et al. [31], Yaguchi et al. [62], although it is noted that explicit finite-difference schemes can be used as well, see [63] for instance.

In the past several decades, Nouri and Sloan [54] have compared six Fourier pseudo-spectral methods for the KdV equation which differ in terms of the time discretisation. One of the most efficient methods tested was the semi-implicit scheme of Chan and Kerkhoven [52]. They integrated the KdV equation in time in Fourier

space using two Fast Fourier Transforms (FFT) per time step. Here, we extend this scheme to solve the coupled Ostrovsky equations.

The advantages of this method are the simplicity of its implementation and the low computing cost of using the fast Fourier transform (FFT), known to be a very efficient algorithm for calculating the discrete Fourier transform (DFT). The FFT algorithm is called the Cooley-Tukey algorithm, after the two authors who universalised it in 1965 [64], although they actually re-invented an algorithm developed by Gauss in 1805 [65]. Note that, when implementing the PS method, certain operations such as differentiation are computed in the spectral domain by applying the FFT to the data whereas other operations such as the multiplication of two functions are best done in real space with the inverse FFT. Finally, the scheme is complemented with a linear damping technique known as "sponge layer" at the ends of the domain and with the de-aliasing technique to treat the nonlinear and sponge layer terms in the systems. Both techniques will be discussed in subsections 4.2.1 and 4.2.2.

4.2 The pseudo-spectral method

In this work, we have set parameters γ and ν in equations (3.30) and (3.31) to be zero. This is based on the calculation of these parameters using the three-layer stratification model. Details of this calculation will be discussed in the next chapter. Equations (3.30) and (3.31) with $\gamma = \nu = 0$ read,

$$\{u_T + uu_X + u_{XXX} + n(uv)_X + mvv_X + \alpha v_{XXX}\}_X = \beta u\,, \quad (4.1)$$

$$\{v_T + vv_X + \delta v_{XXX} + \Delta v_X + p(uv)_X + quu_X + \lambda u_{XXX}\}_X = \mu v\,. \quad (4.2)$$

Thus, we formulate the problem over a periodic domain $-L < x < L$, with $L > 0$ sufficiently large such that the periodicity assumption $u(-L,t) = u(L,t)$ and $v(-L,t) = v(L,t)$ hold for the localised solutions. Initially, we transform the solution interval $[-L, L]$ to the periodicity interval $[0, 2\pi]$ using $\xi = sX + \pi$ where

$s = \pi/L$. Then equations (4.1) and (4.2) will be transformed to:

$$\{u_T + suu_\xi + s^3 u_{\xi\xi\xi} + ns(uv)_\xi + msvv_\xi + \alpha s^3 v_{\xi\xi\xi}\}_\xi = \frac{\beta}{s}u, \quad (4.3)$$

$$\{v_T + svv_\xi + \delta s^3 v_{\xi\xi\xi} + \Delta s v_\xi + ps(uv)_\xi + qsuu_\xi + \lambda s^3 u_{\xi\xi\xi}\}_\xi = \frac{\mu}{s}v. \quad (4.4)$$

It is now convenient to use the following notation for the nonlinear terms:

$$\begin{aligned} suu_\xi &= w_{u\xi}\,, \quad \text{where} \quad w_u = \frac{su^2}{2}\,, \\ svv_\xi &= w_{v\xi}\,, \quad \text{where} \quad w_v = \frac{sv^2}{2}\,, \\ s(uv)_\xi &= w_{c\xi}\,, \quad \text{where} \quad w_c = suv\,. \end{aligned}$$

In this method, the derivatives are computed in the frequency domain by first applying the FFT to the data, then multiplying by the appropriate values and converting back to the spatial domain with the inverse FFT. The interval $[0, 2\pi]$ is discretised by N equidistant points with the spacing $\Delta\xi = 2\pi/N$, generating the values $u(\xi_j, T)$ and $v(\xi_j, T)$ at $\xi = \xi_j = j\Delta\xi$, $j = 0, 1, \cdots, N-1$. Here, N is chosen to be a power of two. Transforming $u(\xi_j, T)$ and $v(\xi_j, T)$ by a DFT gives:

$$\widehat{u}(\kappa, T) = F(u) = \frac{1}{\sqrt{N}} \sum_{j=0}^{N-1} u(\xi_j, T) e^{-i\kappa\xi_j}, \quad -\frac{N}{2} \le \kappa \le \frac{N}{2} - 1,\ \kappa \neq 0\,,$$

$$\widehat{v}(\kappa, T) = F(v) = \frac{1}{\sqrt{N}} \sum_{j=0}^{N-1} v(\xi_j, T) e^{-i\kappa\xi_j}, \quad -\frac{N}{2} \le \kappa \le \frac{N}{2} - 1,\ \kappa \neq 0\,, \quad (4.5)$$

where $i = \sqrt{-1}$ and κ is an integer, which can be interpreted as a discretised and scaled version of a wavenumber. The inverse formulas for the discrete transform are:

$$u(\xi_j, T) = F^{-1}(\widehat{u}) = \frac{1}{\sqrt{N}} \sum_{\kappa=-N/2}^{N/2-1} \widehat{u}(\kappa, T) e^{i\kappa\xi_j}, \qquad j = 0, 1, \cdots, N-1\,,$$

$$v(\xi_j, T) = F^{-1}(\widehat{u}) = \frac{1}{\sqrt{N}} \sum_{\kappa=-N/2}^{N/2-1} \widehat{v}(\kappa, T) e^{i\kappa\xi_j}, \qquad j = 0, 1, \cdots, N-1\,. \quad (4.6)$$

Note that we used $F(.)$ and $F^{-1}(.)$ to denote the discrete Fourier transform and

inverse Fourier transform, respectively. These transformations (4.5) and (4.6) can be performed efficiently using the FFT algorithm, which significantly reduces the amount of required calculations. The standard number of arithmetical operations for calculating the DFT is $O(N^2)$, however, by using the FFT algorithm, the DFT can be computed in $O(N \log N)$ operations, see Huang and Zhang [56].

The derivatives of u and v with respect to X can be calculated by:

$$\frac{\partial^n u}{\partial X^n} = F^{-1}\{(ik)^n F\{u\}\}, \quad n = 1, 2, \ldots. \tag{4.7}$$

The DFT of equations (4.3) and (4.4) with respect to ξ yields:

$$\widehat{u}_T + i\kappa\widehat{w}_u - i\kappa^3 s^3\widehat{u} + in\kappa\widehat{w}_c + im\kappa\widehat{w}_v - i\alpha\kappa^3 s^3\widehat{v} = -\frac{i\beta}{\kappa s}\widehat{u}, \tag{4.8}$$

$$\widehat{v}_T + i\kappa\widehat{w}_v - i\delta\kappa^3 s^3\widehat{v} + i\Delta\kappa s\widehat{v} + ip\kappa\widehat{w}_c + iq\kappa\widehat{w}_u - i\lambda\kappa^3 s^3\widehat{u} = -\frac{i\mu}{\kappa s}\widehat{v}. \tag{4.9}$$

Next, we use the time discretizations:

$$\begin{aligned}
\widehat{u}_T(\kappa, T) &\approx \frac{\widehat{u}(\kappa, T+\Delta T) - \widehat{u}(\kappa, T-\Delta T)}{2\Delta T}, \\
\widehat{u}(\kappa, T) &\approx \frac{\widehat{u}(\kappa, T+\Delta T) + \widehat{u}(\kappa, T-\Delta T)}{2}, \\
\widehat{v}_T(\kappa, T) &\approx \frac{\widehat{v}(\kappa, T+\Delta T) - \widehat{v}(\kappa, T-\Delta T)}{2\Delta T}, \\
\widehat{v}(\kappa, T) &\approx \frac{\widehat{v}(\kappa, T+\Delta T) + \widehat{v}(\kappa, T-\Delta T)}{2}.
\end{aligned} \tag{4.10}$$

Finally, we obtain the forward scheme for the coupled Ostrovsky equations in the form:

$$\begin{aligned}
\widehat{u}(\kappa, T+\Delta T) = \frac{1}{(1 - i\kappa^3 s^3\Delta T + \frac{i\beta\Delta T}{\kappa s})}\{&(1 + i\kappa^3 s^3\Delta T \\
&- \frac{i\beta\Delta T}{\kappa s})\widehat{u}(\kappa, T-\Delta T) - 2i\kappa\Delta T\widehat{w}_u - 2i\kappa\Delta T n\widehat{w}_c \\
&- 2i\kappa\Delta T m\widehat{w}_v + 2i\kappa^3 s^3\Delta T\alpha\widehat{v}\},
\end{aligned} \tag{4.11}$$

$$\begin{aligned}\widehat{v}(\kappa, T+\Delta T) &= \frac{1}{(1-i\kappa^3 s^3 \Delta T\delta + i\kappa s(\Delta T)\Delta + \frac{i\mu\Delta T}{\kappa s})}\{[1+i\kappa^3 s^3\Delta T\delta \\ &\quad -i\kappa s(\Delta T)\Delta - \frac{i\mu\Delta T}{\kappa s}]\widehat{v}(\kappa, T-\Delta T) - 2i\kappa\Delta T\widehat{w}_v \\ &\quad -2i\kappa\Delta T p\widehat{w}_c - 2i\kappa\Delta T q\widehat{w}_u + 2i\kappa^3 s^3\Delta T\lambda\widehat{u}\}\,. \qquad (4.12)\end{aligned}$$

The scheme was successfully tested by checking the single Ostrovsky equation using the initial KdV solitary wave with different amplitudes and comparing with the results from Grimshaw and Helfrich [1]. To validate and illustrate the robustness of the developed numerical scheme, we have undertaken several runs with theoretically predicted results. We tested the code for single KdV and Ostrovsky equations as well as the coupled KdV equations with the periodic boundary conditions.

4.2.1 Domain truncation: sponge layer

In the periodic domain, $-L < x < L$, some waves propagate out of the region of interest and sometimes the radiated waves re-enter the region of interest and interfere with the main wave structure. A solution to prevent the possibility of radiated waves coming back to the main domain is by adding a linear damping region ('sponge layer') at each end of the domain [55]. This approach produces better results because the sponge layer absorbs the waves so that the centre of the domain is unaffected by spurious waves. This technique was also used in [1, 33, 56, 66].

Adding the sponge layer to the coupled Ostrovsky equations (4.1) and (4.2), gives:

$$\{u_T + uu_X + u_{XXX} + n(uv)_X + mvv_X + \alpha v_{XXX} + r(x)u\}_X = \beta u, \quad (4.13)$$

$$\{v_T + vv_X + \delta v_{XXX} + \Delta v_X + p(uv)_X + quu_X + \lambda u_{XXX} + r(x)v\}_X = \mu v, \quad (4.14)$$

where the sponge layer $r(x)$ is a combination of "tanh" functions to damp the solution towards zero at the end of the periodic domain defined by:

$$r(x) = \frac{\nu}{2}\{(1 + \tanh\kappa(x - 3L/4)) + (1 - \tanh\kappa(x + 3L/4))\}\,,$$

for some constants ν and κ. For instance, we chose $\kappa L = 12$ and the value of ν is chosen so that the damping occurs quickly.

The additional sponge layer terms are handled in the same manner as the nonlinear terms, and we use the following new notation:

$$r(x)u = R_u\,, \quad r(x)v = R_v\,.$$

Finally, the forward scheme for the coupled Ostrovsky equations with the sponge layer can be written as:

$$\begin{aligned}\widehat{u}(\kappa, T + \Delta T) &= \frac{1}{(1 - i\kappa^3 s^3 \Delta T + \frac{i\beta\Delta T}{\kappa s})}\{(1 + i\kappa^3 s^3 \Delta T \\ &\quad - \frac{i\beta\Delta T}{\kappa s})\widehat{u}(\kappa, T - \Delta T) - 2i\kappa\Delta T\widehat{w}_u - 2i\kappa\Delta T n\widehat{w}_c \\ &\quad - 2i\kappa\Delta T m\widehat{w}_v + 2i\kappa^3 s^3 \Delta T\alpha\widehat{v} - 2\Delta T R_u\}\,, \end{aligned} \tag{4.15}$$

$$\begin{aligned}\widehat{v}(\kappa, T + \Delta T) &= \frac{1}{(1 - i\kappa^3 s^3 \Delta T\delta + i\kappa s(\Delta T)\Delta + \frac{i\mu\Delta T}{\kappa s})}\{[1 + i\kappa^3 s^3 \Delta T\delta \\ &\quad - i\kappa s(\Delta T)\Delta - \frac{i\mu\Delta T}{\kappa s}]\widehat{v}(\kappa, T - \Delta T) - 2i\kappa\Delta T\widehat{w}_v \\ &\quad - 2i\kappa\Delta T p\widehat{w}_c - 2i\kappa\Delta T q\widehat{w}_u + 2i\kappa^3 s^3 \Delta T\lambda\widehat{u} \\ &\quad - 2\Delta T R_v\}\,. \end{aligned} \tag{4.16}$$

The solution in physical space is obtained by the inverse discrete Fourier transform (4.6). The values of L and N and the appropriate time step Δt were chosen through numerical experiments.

4.2.2 Dealiasing and Two-Thirds Rule

The PS method solves nonlinear partial differential equations with periodic boundary conditions by means of the discrete Fourier transform. The multiplication operations used in the PS method can generate higher frequencies due to DFT. These higher frequencies are referred to as aliasing error due to the pollution of the numerically calculated Fourier transform by higher frequencies because of the truncation of the series, see Canuto et al. [53] and Boyd [55] for details. This operation is important to the nonlinear and sponge layer terms in the coupled Ostrovsky equations. The implementation to control the development of high frequency modes or to remove the aliasing error is called the de-aliasing technique.

There are several such techniques and one of them is the 2/3 dealiasing rule. The aliasing error can be terminated by putting a certain number of high-frequency components of $\widehat{u}$ and $\widehat{v}$ equal to 0 after the multiplication operations. Basically, we put roughly 1/3 of the coefficients equal to 0 [53]. Therefore, the scheme only deals with a lower resolution that is 2/3 of the number N of modes. This should be done every time that the nonlinear and the sponge layer terms in the equations are computed. This implementation of the 2/3 de-aliasing rule has also been used by Thomas and Ruo [58] to compare the behaviour of PS methods using 2/3 dealiasing rule between a high order Fourier smoothing in order to remove the aliasing errors.

4.3 Initial conditions

4.3.1 Approximate solitary wave solution of coupled KdV equations

The initial conditions are obtained as approximate solitary wave solutions of the coupled KdV equations, (3.30) and (3.31) with the rotation terms omitted: $\beta =$

$\mu = \gamma = \nu = 0$,

$$u_T + uu_X + u_{XXX} + n(uv)_X + mvv_X + \alpha v_{XXX} = 0, \tag{4.17}$$

$$v_T + vv_X + \delta v_{XXX} + \Delta v_X + p(uv)_X + quu_X + \lambda u_{XXX} = 0. \tag{4.18}$$

Solitary wave solutions of these equations are found by seeking solutions which depend only on $X - c_s T$, where c_s is the solitary wave speed to be found as part of the solution. Thus, for solitary waves, (4.17) and (4.18) reduce to:

$$-c_s u + \frac{u^2}{2} + u_{XX} + nuv + \frac{mv^2}{2} + \alpha v_{XX} = 0, \tag{4.19}$$

$$-c_s v + \frac{v^2}{2} + \delta v_{XX} + \Delta v + puv + \frac{qu^2}{2} + \lambda u_{XX} = 0. \tag{4.20}$$

The dynamical systems approach is used for small-amplitude waves, where the solutions bifurcate from the linear long wave speeds, which are 0 in the first case and Δ in the second one (see, for example, Grimshaw and Gerard [50]). Recall that $\Delta < 0$, so the bifurcation from 0 will yield a KdV solitary wave, and the bifurcation from Δ will yield a generalised solitary wave.

4.3.1.1 Bifurcation from 0

In the linear long wave limit, $v \to 0$, and u is arbitrary. This is then expanded as follows:

$$u = \epsilon^2 A(\xi) + \epsilon^4 A_2(\xi) + \cdots, \quad v = \epsilon^4 B_2(\xi) + \cdots, \quad c_s = \epsilon^2 c_2 + \cdots, \quad \xi = \epsilon X\,. \tag{4.21}$$

By collecting terms of $O(\epsilon^4)$, we obtain the following equations:

$$-c_2 A + \frac{A^2}{2} + A_{\xi\xi} = 0\,, \quad \Delta B_2 + \frac{qA^2}{2} + \lambda A_{\xi\xi} = 0\,; \tag{4.22}$$

where:

$$A = a\,\mathrm{sech}^2(\gamma\xi)\,, \quad c_2 = \frac{a}{3} = 4\gamma^2\,, \tag{4.23}$$

$$B_2 = -\frac{\lambda a^2}{3\Delta}\mathrm{sech}^2(\gamma\xi) + \frac{(\lambda - q)a^2}{2\Delta}\mathrm{sech}^4(\gamma\xi)\,. \tag{4.24}$$

Hence in the original coordinates the initial condition is:

$$u = a\,\mathrm{sech}^2(\gamma X)\,, \quad a = 12\gamma^2\,, \tag{4.25}$$

$$v = -\frac{\lambda a^2}{3\Delta}\,\mathrm{sech}^2(\gamma X) + \frac{(\lambda - q)a^2}{2\Delta}\,\mathrm{sech}^4(\gamma X)\,, \tag{4.26}$$

where a is a disposable parameter, ideally small (parameters have been rescaled as $\epsilon^2 a \to a$ and $\epsilon\gamma \to \gamma$). This asymptotic solution requires that $\Delta \neq 0$ is order unity. Note that the nonlinear term $(u^2/2)_{XX}$ has a maximum absolute value of $2a^2\gamma_1^2 = a^3/6$. When instead $\Delta \sim O(a)$, then equations (4.17) and(4.18) are strongly coupled, and the expressions (4.25) cannot be used.

4.3.1.2 Bifurcation from Δ

In the linear long wave limit, $c_s \to \Delta$, $u \to 0$, and v is arbitrary. The expansion is now given by:

$$u = \epsilon^4 A_2(\xi) + \cdots\,, \quad v = \epsilon^2 B(\xi) + \epsilon^4 B_2(\xi) + \cdots\,, \quad c_s = \Delta + \epsilon^2 c_2 + \cdots\,, \quad \xi = \epsilon X\,. \tag{4.27}$$

By collecting the terms of $O(\epsilon^4)$, the following is obtained:

$$-c_2 B + \frac{B^2}{2} + \delta B_{\xi\xi} = 0\,, \quad -\Delta A_2 + \frac{mB^2}{2} + \alpha B_{\xi\xi} = 0\,; \tag{4.28}$$

where:

$$B = b\,\mathrm{sech}^2(\gamma\xi)\,, \quad c_2 = \frac{b}{3} = 4\delta\gamma^2\,, \tag{4.29}$$

$$A_2 = \frac{\alpha b^2}{3\delta\Delta}\mathrm{sech}^2(\gamma\xi) + \frac{(\delta m - \alpha)b^2}{2\delta\Delta}\mathrm{sech}^4(\gamma\xi)\,. \tag{4.30}$$

Hence in the original coordinates the initial condition is:

$$v = b\,\mathrm{sech}^2(\gamma X)\,, \quad b = 12\delta\gamma^2\,, \tag{4.31}$$

$$u = \frac{\alpha b^2}{3\delta\Delta}\mathrm{sech}^2(\gamma X) + \frac{(\delta m - \alpha)b^2}{2\delta\Delta}\mathrm{sech}^4(\gamma X)\,, \tag{4.32}$$

where b is a disposable parameter, ideally small (parameters have been rescaled as $\epsilon^2 b \to b$ and $\epsilon\gamma \to \gamma$). Formally, these are generalised solitary waves, with an exponentially small radiating tail, but that is ignored here, as we only require an initial condition for our computations. Note that the nonlinear term $(v^2/2)_{XX}$ has a maximum absolute value of $2b^2\gamma_2^2 = b^3/6\delta$. This asymptotic solution again requires that $\Delta \neq 0$ is order unity.

4.3.1.3 Weak coupling KdV solitary waves

The asymptotic solutions described above are not suitable when either Δ is small, or when the amplitudes a, b are not small. However, if the coupling is weak, that is $m, n, p, q, \alpha, \lambda$ are all small, then the leading order approximation is just the free solitary wave solution of each uncoupled equation. Here a small modification of these solutions is proposed, that is:

$$u = a\,\mathrm{sech}^2(\gamma_1 X)\,, \quad \frac{a}{3} = 4(1+\alpha)\gamma_1^2\,, \tag{4.33}$$

$$v = b\,\mathrm{sech}^2(\gamma_2 X)\,, \quad \frac{b}{3} = 4(\delta+\lambda)\gamma_2^2\,. \tag{4.34}$$

This should be useful especially when $m = n = p = q = 0$ and Δ, α, λ are small. This was implemented with the constraint $\gamma_1 = \gamma_2$. In the symmetric case, when $\delta = 1$, and $\alpha = \lambda$, this is an exact solution when $\Delta = 0$, and it is this feature which has motivated the incorporation of the terms α, λ in these expressions. Note that here the nonlinear terms $(u^2/2)_{XX}$ and $(v^2/2)_{XX}$ have maximum absolute values of $2a^2\gamma_1^2 = a^3/6(1+\alpha)$ and $2b^2\gamma_2^2 = b^3/6(\delta+\lambda)$ respectively.

4.3.2 Nonlinear wave packet

The nonlinear wave packet initial condition is based on either a maximum point in the group velocity curve where $\partial c_g/\partial k = 0$ and $k = k_m$, or a maximum point in the phase velocity curve where $c_p = c_g$ and $k = k_s$. The former corresponds to the unsteady nonlinear wave packet travelling at a speed close to the maximum group velocity.

To obtain a suitable wave packet initial condition, the procedure is to choose k, either k_m or k_s, and then find the ratio $r = u_0/v_0$ from (5.16) or (5.17) in the form $u_0 = U_0 a_0, v_0 = V_0 a_0$ where a_0 is an arbitrary function of X, but U_0, V_0 are known functions of k. Based on the expected outcome that the nonlinear wave packet will be governed by an evolution equation such as the nonlinear Schrödinger equation, $a_0(X) = A_0 \operatorname{sech}(K_0 X)$ is chosen. Note that the underlying theory suggests that the shape should be sech, and that K_0 depends on the amplitude A_0, see Grimshaw and Helfrich [1]. Here instead a value of $K_0 << k$ is selected. Then the wave packet initial conditions are:

$$u(X,0) = rV_0 A_0 \operatorname{sech}(K_0 X)\cos(kX)\,, \tag{4.35}$$

$$v(X,0) = V_0 A_0 \operatorname{sech}(K_0 X)\cos(kX)\,, \tag{4.36}$$

where $r = U_0/V_0$ is a known function of k, and V_0 can be chosen arbitrarily.

4.3.3 Pedestal

Solutions of the coupled Ostrovsky equations must satisfy the zero mass constraints:

$$\int_{-L}^{L} u(X,T)\,dX = 0\,, \quad \int_{-L}^{L} v(X,T)\,dX = 0\,. \tag{4.37}$$

If $u(X,0) = u_0(X)$ and $v(X,0) = v_0(X)$ then also:

$$\int_{-L}^{L} u_0(X)\,dX = 0\,, \quad \int_{-L}^{L} v_0(X)\,dX = 0\,.$$

Thus if the initial condition described above is, say $\tilde{u}_0(X)$, then this must be corrected to have zero mass by adding a negative pedestal $\tilde{d}(X)$ as follows:

$$u_0(X) = \tilde{u}_0(X) - \tilde{d}(X)\,, \quad \int_{-L}^{L} \tilde{u}_0(X)\,dX = \int_{-L}^{L} \tilde{d}(X)\,dX\,.$$

Note that $\tilde{d}(X)$ cannot be a constant here due to the presence of the sponge layer in equations (4.13) and (4.14).

For instance, consider the case of bifurcation from Δ, where the v-mode is given by:

$$\tilde{v}_0 = b\,\mathrm{sech}^2(\gamma X)\,,$$
$$v_0(X) = \tilde{v}_0(X) - \tilde{d}_v(X)\,, \quad \int_{-L}^{L} \tilde{d}_v(X)\,dX = \int_{-L}^{L} \tilde{v}_0(X)\,dX \approx \frac{2b}{\gamma}\,, \quad \gamma L \gg 1\,.$$

Then, we can choose $\tilde{d}_v(X)$ as follows:

$$\tilde{d}_v(X) = \frac{d_{0v}}{2}\{\tanh\left(\kappa_0(X + L/2)\right) - \tanh\left(\kappa_0(X - L/2)\right)\}\,, \quad \kappa_0 L/4 \gg 1\,.$$

For example, let $\kappa_0 L = 12$, then:

$$\int_{-L}^{L} \tilde{d}_v(X)\,dX \approx d_{0v} L\,, \quad \text{so that} \quad d_{0v} = \frac{2b}{\gamma L}\,.$$

Next, for the u-mode given by:

$$\tilde{u}_0 = \frac{\alpha b^2}{3\delta\Delta}\,\mathrm{sech}^2(\gamma X) + \frac{(\delta m - \alpha)b^2}{2\delta\Delta}\,\mathrm{sech}^4(\gamma X)\,,$$

the same method is used, that is we let

$$\tilde{d}_u(X) = \frac{d_{0u}}{2}\{\tanh\left(\kappa_0(X + L/2)\right) - \tanh\left(\kappa_0(X - L/2)\right)\}\,, \quad \kappa_0 L/4 \gg 1\,,$$

$$d_{0u} L = \int_{-L}^{L} \tilde{u}_0(X)\,dX = \int_{-L}^{L} \{\frac{\alpha b^2}{3\delta\Delta}\,\mathrm{sech}^2(\gamma X) + \frac{(\delta m - \alpha)b^2}{2\delta\Delta}\,\mathrm{sech}^4(\gamma X)\}\,dX\,,$$

$$\text{so that} \quad d_{0u} = \frac{2\alpha b^2}{3\delta\Delta\gamma L} + \frac{2(\delta m - \alpha)b^2}{3\delta\Delta\gamma L} = \frac{2mb^2}{3\delta\Delta\gamma L}\,.$$

Now, the initial conditions with a negative pedestal are:

$$u_0(x) = \tilde{u}_0(x) - \tilde{d}_u(X)\,,$$

$$v_0(x) = \tilde{v}_0(x) - \tilde{d}_v(X)\,.$$

An analogous procedure was used for the other initial conditions.

4.4 Conclusion

In this chapter we first described the pseudo-spectral method used to solve the derived coupled Ostrovsky equations numerically. The proposed numerical method has been successfully used for the solution of the single KdV equation and Ostrovsky equation by Nouri and Sloan [54], Gulkac and Ozis [60], Grimshaw and Helfrich [1]. The method was complemented with the use of the linear 'sponge layer' at the ends of the domain and the '2/3 dealiasing rule'. Next, we described a number of initial conditions which will be used in the subsequent numerical simulations.

Chapter 5

Coupled Ostrovsky equations for internal waves in a three-layer model without a shear flow

5.1 Introduction

In this chapter we consider the case when there is no shear flow, that is $u_0(z) = 0$. A three-layer model is used in order to illustrate the general theory and as a guide to choosing the coefficients in the coupled Ostrovsky equations. It has to be stressed that the aim of this chapter is just an illustration of a general idea and the model that we described is not necessarily realistic. It is an extension of the model used by Gear and Grimshaw [39] and designed to allow for an explicit analytical determination of the system parameters to guide the explicit construction of a suite of linear dispersion curves, to be used as a basis for the numerical simulations. However, it could be viewed as a simple model of a double thermocline. The extension to include a background shear flow is described in Chapter 6.

5.2 Analysis

5.2.1 Three-layer model

We consider a three-layer model, which is an extension of the model discussed by Gear and Grimshaw [39]. We assume that there is no shear flow, $u_0(z) = 0$, and the buoyancy frequency is given by:

$$N = N_1 + (N_2 - N_1)H(z + h_2 + h_3) + (N_3 - N_2)H(z + h_3)\,. \tag{5.1}$$

Here N is a constant, $N_{1,2,3}$, in each of three layers of depths $h_{1,2,3}$ where $h = h_1 + h_2 + h_3$, counted from the bottom to the top, see Figure 5.1, and $H(z)$ is the Heaviside step function ($H(z) = 0$ for $z < 0$ and $H(z) = 1$ for $z \geq 0$).

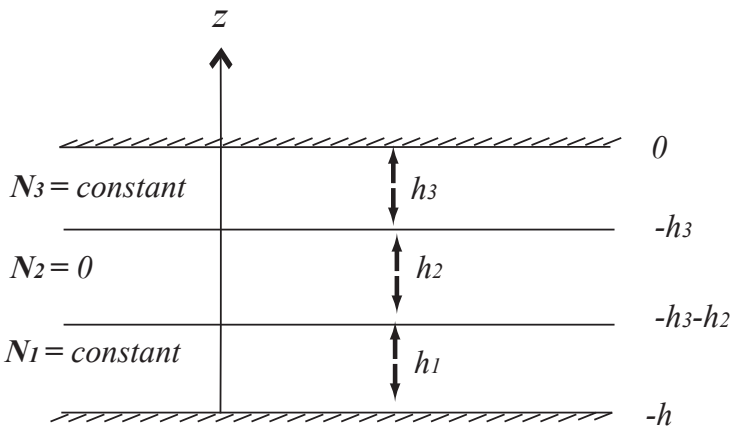

FIGURE 5.1: Schematic plot for a three-layer stratification without shear flow.

This is not meant to be a realistic model of a typical ocean stratification, but nonetheless is representative of a double thermocline. The present example is designed to be amenable to an analytic solution, so that the expressions for all coefficients can be found explicitly. Using the Boussinesq and rigid lid approximations with no shear flow, we can find two modes $\phi_{1,2}$ each satisfying the modal

equation (3.3) and the boundary conditions (3.4):

$$\phi_{zz} + \frac{N^2}{c^2}\phi = 0\,, \tag{5.2}$$

$$\phi = 0 \quad \text{at} \quad z = -h, 0\,. \tag{5.3}$$

The modal equation (5.2) holds in each layer, and ϕ, ϕ_z are continuous at the layer boundaries. This is the extension of the case studied by Gear and Grimshaw [39] who also put $h_1 = h_2 = h_3$ and $N_2 = 0$; their Figure 2 shows a near resonance at $N_3 = 0.42N_1$. Here we also put $N_2 = 0$, but leave $h_{1,2,3}$ undetermined at this stage. The solution is given by

$$\phi = A_1 \frac{\sin\left(N_1(z+h)/c\right)}{\sin\left(N_1 h_1/c\right)}\,, \quad -h < z < -h + h_1\,, \tag{5.4}$$

$$\phi = -A_1 \frac{z + h_3}{h_2} + A_3 \frac{z + h_2 + h_3}{h_2}\,, \quad -h_2 - h_3 < z < -h_3\,, \tag{5.5}$$

$$\phi = -A_3 \frac{\sin\left(N_3 z/c\right)}{\sin\left(N_3 h_3/c\right)}\,, \quad -h_3 < z < 0\,, \tag{5.6}$$

where A_1, A_3 are the amplitudes at $z = -h + h_1, z = -h_3$ respectively, and the continuity of ϕ is already satisfied. Then, continuity of ϕ_z yields:

$$A_1 N_1 \cot\left(N_1 h_1/c\right) = -A_1 \frac{c}{h_2} + A_3 \frac{c}{h_2}\,, \tag{5.7}$$

$$-A_3 N_3 \cot\left(N_3 h_3/c\right) = A_3 \frac{c}{h_2} - A_1 \frac{c}{h_2}\,. \tag{5.8}$$

The determinant of this 2×2-system of equations (5.7) and (5.8), will yield c. Thus, we get that:

$$D_1 D_3 - D_2^2 = 0\,, \tag{5.9}$$

where:

$$D_1 = N_1 \cot\left(\frac{N_1 h_1}{c}\right) + \frac{c}{h_2}\,,$$

$$D_3 = N_3 \cot\left(\frac{N_3 h_3}{c}\right) + \frac{c}{h_2}\,,$$

$$D_2 = \frac{c}{h_2}\,.$$

In order to obtain a resonance, that is a double solution c with two distinct modes, it is required that $D_1 = D_3 = D_2 = 0$ simultaneously in order to ensure that there are two independent solutions for A_1, A_3. Formally, it is necessary to take the limit $h_2 \gg h_{1,3}$. In this limit, $D_2 \to 0$, and this obtains a desired resonance if $c = c_{res}$ is chosen so that $D_1 = D_3 = 0$, that is:

$$\frac{N_1 h_1}{c_{res}} = \frac{N_3 h_3}{c_{res}} = (n + \frac{1}{2})\pi\,, \quad n = 0, 1, 2, \cdots\,. \tag{5.10}$$

Clearly this requires that $N_1 h_1 = N_3 h_3$, which is satisfied, in particular, in the symmetric case $h_1 = h_3, N_1 = N_3$. In this limit there is an exact resonance, with a double solution for c_{res} and A_1, A_3 can be chosen arbitrarily. A sensible choice is $A_1 = 1, A_3 = 0$ and $A_1 = 0, A_3 = 1$ so that the two modes with the same speed correspond to a lower interface mode, and an upper interface mode respectively. In practice, it is assumed that h_2 is finite, but $h_{1,3} \ll h_2$. Then the detuning parameter Δ is small, but non-zero. Letting $c = c_{res} + \Delta$ it is found that:

$$\Delta = -\frac{c_{res}^2 (N_1 + N_3)}{h_2 N_1 N_3 (n + 1/2)\pi}\,. \tag{5.11}$$

At the leading order, the modes defined by (5.4), (5.5), (5.6) are now given by:

$$\begin{aligned}
&\phi_1 = (-1)^n \sin\{\frac{(n+1/2)\pi(z+h)}{h_1}\}\,, \quad -h < z < -h + h_1\,,\\
&\phi_1 = -\frac{z + h_3}{h_2}\,, \quad -h_2 - h_3 < z < -h_3\,,\\
&\phi_1 = 0\,, \quad -h_3 < z < 0\,,
\end{aligned} \tag{5.12}$$

$$\begin{aligned}
&\phi_2 = 0\,, \quad -h < z < -h + h_1\,,\\
&\phi_2 = \frac{z + h_2 + h_3}{h_2}\,, \quad -h_2 - h_3 < z < -h_3\,,\\
&\phi_2 = (-1)^{n+1} \sin\{\frac{(n+1/2)\pi z}{h_3}\}\,, \quad -h_3 < z < 0\,.
\end{aligned} \tag{5.13}$$

Note that formally, $\phi_{1,2} = 1$ in the near field where $z + h_2 + h_3 > 0, z + h_3 < 0$ respectively when z is fixed as h_2 is large. All coefficients in the coupled Ostrovsky

system can now be evaluated, here for $n = 0$. Thus, we get that

$$c_{res} = C\,, \quad C = \frac{2N_1h_1}{\pi} = \frac{2N_3h_3}{\pi}\,,$$

$$I_1 = \frac{N_1^2h_1}{C} = \frac{\pi^2 C}{4h_1}\,, \quad I_2 = \frac{N_3^2h_3}{C} = \frac{\pi^2 C}{4h_3}\,,$$

$$I_1\mu_1 = 2N_1^2\,, \quad I_2\mu_2 = -2N_3^2\,,$$

$$I_1\lambda_1 = C^2\left(\frac{h_1}{2} + \frac{h_2}{3}\right)\,, \quad I_2\lambda_2 = C^2\left(\frac{h_3}{2} + \frac{h_2}{3}\right) \quad \lambda_{12} = \lambda_{21} = C^2\frac{h_2}{6}\,,$$

$$\nu_1 = \nu_2 = 0\,, \quad \gamma_1 = \gamma_2 = \frac{\tilde{f}^2}{2C}\,, \quad \gamma_{12} = \gamma_{21} = 0\,.$$

Note that the nonlinear coupling coefficients $\nu_{1,2}$ are zero, but $\lambda_{12} \neq 0$ so the coupling is purely through the linear dispersion terms. There is an apparent serious deficiency here in that $\lambda_{1,2,12}$ all scale with h_2, and h_2 is large. In this limit $I_1\lambda_1 \sim I_2\lambda_2 \sim 2\lambda_{12}$. However a rescaling of time and space in the coupled Ostrovsky equations can remove this, as seen in the rescaled equations (3.30), (3.31).

The simplest case here is the symmetric case when $N_1 = N_3, h_1 = h_3$, when the symmetry indicates that $\mu_1 = -\mu_2, \lambda_1 = \lambda_2$. Then, except for the detuning parameter Δ, the coupled Ostrovsky system is symmetric. This reduces the parameter space considerably, as then $m = n = p = q = 0, \delta = 1, \alpha = \lambda = -1/2, \beta = \mu, \gamma = \nu = 0$, leaving only two parameters, Δ, β, which can be varied independently. The non-symmetric case when $N_1 \neq N_3$ has $p = n = q = m = 0$, $\gamma = \nu = 0$, and $\delta = h_3/h_1\,, \beta = \mu$, while $\alpha = -h_3/2h_1 = -\delta/2, \lambda = -1/2$, so that $\alpha\lambda = h_3/4h_1$. Hence there are now three parameters $\Delta, \beta, \delta = h_3/h_1$, which can be varied independently.

5.2.2 Linear dispersion relation

The scaled coupled Ostrovsky equations obtained in Chapter 2 are given by

$$(u_T + uu_X + u_{XXX} + n(uv)_X + mvv_X + \alpha v_{XXX})_X = \beta u + \gamma v, \quad (5.14)$$

$$(v_T + vv_X + \delta v_{XXX} + \Delta v_X + p(uv)_X + quu_X + \lambda u_{XXX})_X = \mu v + \nu u, \quad (5.15)$$

The linear dispersion relation is obtained by linearising the equations (5.14), (5.15) and then seeking solutions in the form of:

$$u = u_0 e^{ik(X - c_p T)} + c.c., \quad v = v_0 e^{ik(X - c_p T)} + c.c.\,,$$

where k is the wavenumber and c_p is the phase speed and $c.c.$ denotes the complex conjugate. This leads to:

$$(c_p - C_1(k))u_0 + (\alpha k^2 - \frac{\gamma}{k^2})v_0 = 0\,, \quad (5.16)$$

$$(\lambda k^2 - \frac{\nu}{k^2})u_0 + (c_p - C_2(k))v_0 = 0\,, \quad (5.17)$$

$$\text{where} \quad C_1(k) = -k^2 + \frac{\beta}{k^2}\,, \quad C_2(k) = \Delta - \delta k^2 + \frac{\mu}{k^2}\,. \quad (5.18)$$

The determinant of this 2×2 system yields the dispersion relation:

$$(c_p - C_1(k))(c_p - C_2(k)) = D(k) = (\alpha k^2 - \frac{\gamma}{k^2})(\lambda k^2 - \frac{\nu}{k^2})\,. \quad (5.19)$$

Solving this dispersion relation we obtain the two branches of the dispersion relation:

$$c_p = c_{p1,p2} = \frac{C_1 + C_2}{2} \pm \frac{1}{2}\{4D + (C_1 - C_2)^2\}^{1/2}\,. \quad (5.20)$$

Here $C_{1,2}(k)$ are the linear phase speeds of the uncoupled Ostrovsky equations, obtained formally by setting the coupling term $D(k) = 0$. If $D(k) > 0$ for all k, then both branches are real-valued for all wavenumbers k, and the linearised system is spectrally stable. This will be assumed henceforth, and it is noted that this is assured in the absence of a background shear flow, as then $\gamma = \nu = 0$ and $\alpha\lambda > 0$ so that $D(k) > 0$ for all k.

The case when there is no background shear is the main concern in this chapter, and in that case $\gamma = \nu = 0$, and it can be assumed also that $c > 0, I_1 > 0, I_2 > 0$ without loss of generality. It follows that then $\lambda_{1,2} > 0$, so that $\delta > 0$, $\beta = \mu > 0$ and $0 < \alpha\lambda < \delta$. In particular the coupling coefficient $D(k) = \alpha\lambda k^4 > 0$ for all $k > 0$. Also it is recalled that $\Delta < 0$ without loss of generality. Then (5.20) reduces to:

$$c_{p1,p2} = \frac{\beta}{k^2} + \frac{\Delta}{2} - \frac{(1+\delta)k^2}{2} \pm \frac{1}{2}\sqrt{[\Delta + (1-\delta)k^2]^2 + 4\alpha\lambda k^4}. \tag{5.21}$$

The group velocities are given by $c_g = d(kc_p)/dk$:

$$c_{g1,g2} = -\frac{\beta}{k^2} + \frac{\Delta}{2} - \frac{3(1+\delta)k^2}{2} \pm \frac{[\Delta + (1-\delta)k^2][\frac{1}{2}\Delta + \frac{3}{2}(1-\delta)k^2] + 6\alpha\lambda k^4}{\sqrt{[\Delta + (1-\delta)k^2]^2 + 4\alpha\lambda k^4}}\,. \tag{5.22}$$

It is useful now to examine the limits $k \to 0, \infty$. Thus:

$$c_{p1,p2} \to \frac{\beta}{k^2} + (0, \Delta) + O(k^2), \quad \text{as} \quad k \to 0\,, \tag{5.23}$$

$$c_{p1,p2} \to E_{1,2}k^2\,, \quad \text{as} \quad k \to \infty\,, \tag{5.24}$$

where $2E_{1,2} = -(1+\delta) \pm \{(1-\delta)^2 + 4\alpha\lambda\}^{1/2}$.

Note that since $0 < \alpha\lambda < \delta$, $E_2 < E_1 < 0$. It follows that both branches have no spectral gaps, and it is inferred that there are no solitary waves. Note that the two branches coalesce as $k \to 0$, implying that in this limit there is a strong coupling between the two modes. This can be compared with the case for no rotation, when $\beta = 0$, and there is a spectral gap for both modes when $c > 0$ where KdV solitary waves for mode 1 exist, and a spectral gap for mode 2 when $c > \Delta$ and then generalised solitary waves exist, in resonance with mode 1. But when there is rotation $\beta > 0$, both gaps are removed, which is the same scenario that arises for the single Ostrovsky equation.

Note that with the scaling (3.29), X, T are scaled variables and have dimensions of $C^{-1/2}, C^{-3/2}$ respectively, where C is a velocity scale, i.e ms^{-1} . The dependent variables u and v have the dimension of C. The coefficients $n, m, \alpha, \delta, p, q, \lambda$ are

dimensionless, while β, γ, μ, ν have dimensions of C^2, and Δ has the dimension of C. The wavenumber k and c_p, c_g have the dimensions of $C^{1/2}$ and C respectively. In what follows we omit writing the dimensions for the scaled variables.

A typical dispersion curve is shown in Figure 5.2, which is based on the parameter values obtained from the three-layer example discussed above in section 5.2.1. The significant features are that there is no spectral gap, and that both group velocity curves have a turning point with maximum speed. Hence, based on the results for the single Ostrovsky equation obtained by Grimshaw and Helfrich [1], it is expected that the initial solitary-like wave initial conditions will collapse through the radiation of inertia-gravity waves, followed by the emergence of two nonlinear wave packets associated with each of these maximum group velocities.

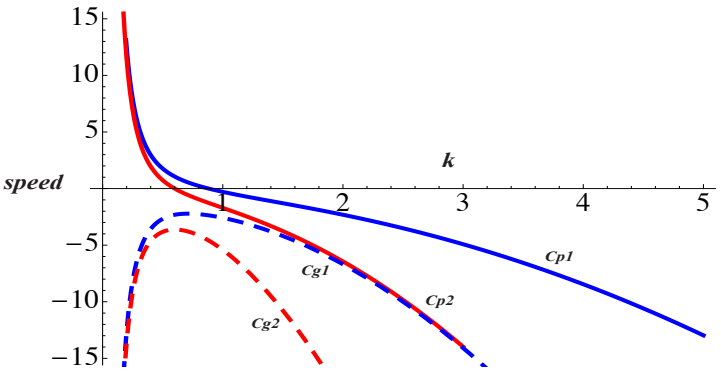

FIGURE 5.2: Typical dispersion curves from (5.21) with $\delta = 1, \alpha = \lambda = -0.5, \beta = \mu = 0.5$. The solid curves are the phase speed, and the dashed curves are the group velocity.

5.3 Numerical results

The coupled Ostrovsky equations (3.30), (3.31) are solved numerically with the PS scheme and the initial conditions described in Chapter 3, which model a solitary wave solution of the coupled KdV system obtained by removing the rotation terms. The derivation of this initial data is described in (4.3.1.1), (4.3.1.2) when Δ is $O(1)$ and the initial amplitudes a, b of u, v are small, and by (4.3.1.3) when Δ is small but a, b are not small. Note that then in order for nonlinear effects to

be significant initially, it is required that $(u^2/2)_{XX} > \beta u$ and $(v^2/2)_{XX} > \mu v$. For the initial conditions (4.3.1.1) and (4.3.1.2) these imply that $a^2 > 6\beta$ and $b^2 > 6\delta\mu$, and $a^2 > 6\beta|1+\alpha|$ and $b^2 > 6\mu|\delta+\lambda|$ respectively. Although the initial conditions (4.3.1.1) and (4.3.1.2) are firmly based on a valid bifurcation analysis, in practice the initial conditions were too small to generate significant nonlinear effects, and consequently the emergence of the expected nonlinear wave packets was suppressed. Consequently, all the results shown here used the initial condition (4.3.1.3). A summary of some typical simulations is set out in Table 5.1 and 5.3.

Three cases will be discussed based on the three-layer example of section (5.2.1). These are the symmetric case $N_1 = N_3$ when $m = n = p = q = 0$, $\alpha = \lambda = -1/2$ and $\delta = 1$, and two non-symmetric cases $N_1 \neq N_3$ with $N_3/N_1 = 4$, where $\delta = h_3/h_1 = 1.5, 0.2$, $\alpha = -h_3/2h_1 = -0.75, -0.1$ respectively. Note that $\lambda = -1/2$ in all cases. As diagnostics, we compare the speeds of the numerically found wave packets with the maximum group speeds c_{g1}, c_{g2} from the linear dispersion relation, see (5.22), and also the modal structure, that is the ratio $r_{1,2} = |u_0|/|v_0|$ computed from either (5.16) or (5.17) for the corresponding wave numbers. A summary of the results from our simulations is shown in Tables 5.2 and 5.4. Overall, there is good agreement with the predicted speeds $c_{g1,g2}$ and ratios $r_{1,2}$ and those found in the simulations, $C_{g1,g2}$ and $R_{1,2}$. In the following subsections, some typical plots of numerical simulations are shown.

5.3.1 Symmetric case

Here, when $\Delta = 0$, the initial condition 4.3.1.3 used has $u = v$ at $t = 0$. But in this special case, $u = v$ is an exact solution for all time, each satisfying a single Ostrovsky equation. Hence in this case only one mode is activated and the solution is the same as that found for a single Ostrovsky equation by Grimshaw and Helfrich [1]. As $|\Delta|$ is increased, the signature of a second wave packet emerges. A typical result is shown in Figures 5.3 and 5.4. Two wave packets are clearly visible in the plots for the v-component, but the second packet is barely discernible in the

plots for the u-component, where its predicted amplitude is too small for it to be distinguished from the background field of radiating waves.

Simulation	N	L	Δt	Δ	β	δ	α	λ	a	b
1	2048	1200	0.0001	-0.1	1	1	-0.5	-0.5	5	5
2	2048	1200	0.0001	-0.5	1	1	-0.5	-0.5	5	5
3	2048	1200	0.0001	-1.0	1	1	-0.5	-0.5	5	5

TABLE 5.1: Simulation parameters for symmetric case

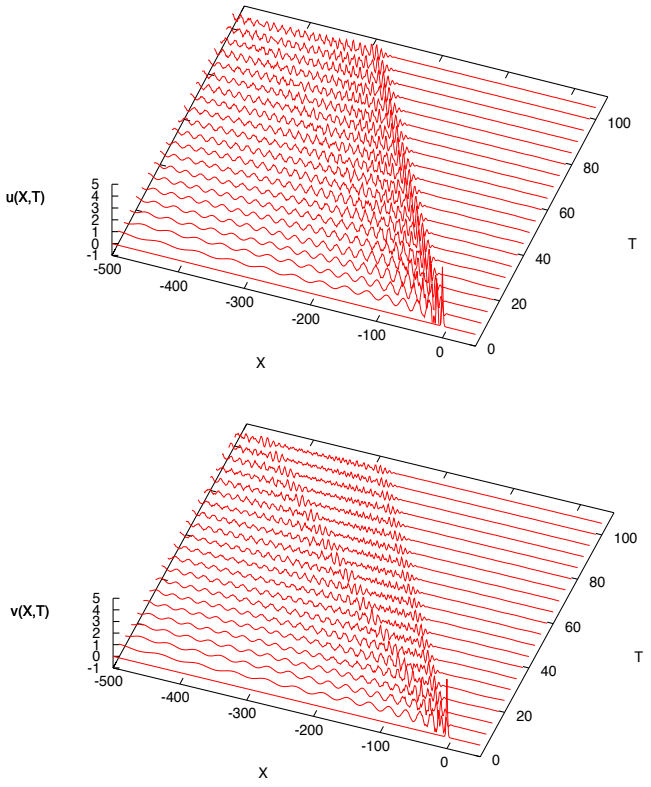

FIGURE 5.3: Numerical simulations for the symmetric case ($N_1 = N_3$) using a KdV initial condition of weak coupling with the parameter $a = b = 5$.

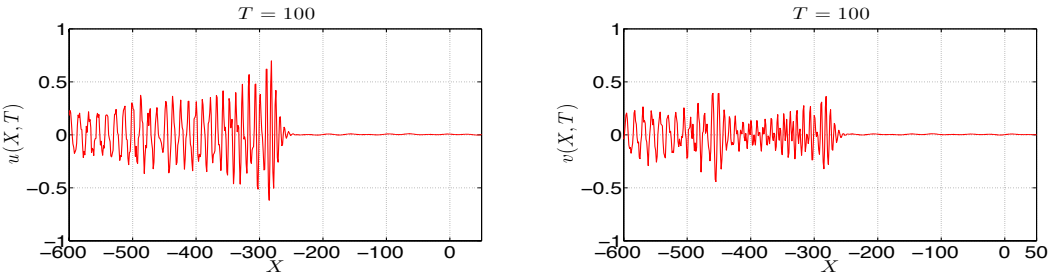

FIGURE 5.4: Same as Figure 5.3, but a cross-section at $T = 100$ for both modes.

Data	c_{g1}	C_{g1}	c_{g2}	C_{g2}	r_1	R_1	r_2	R_2
1	-2.502	-2.548	-4.288	-4.238	1.130	1.143	0.810	0.789
2	-2.749	-2.778	-4.452	-4.500	1.781	1.905	0.400	0.320
3	-3.008	-3.056	-4.783	-4.778	2.950	3.167	0.235	0.238

TABLE 5.2: Numerically determined group velocities, $C_{g1,g2}$ and modal ratio $R_{1,2}$ versus theoretical predictions $c_{g1,g2}$ and ratio $r_{1,2}$ for each case.

5.3.2 Non-symmetric case

When $\delta \neq 1$, the symmetry is broken even when $\Delta = 0$, and now two wave packets are clearly seen. Typical plots are shown when $\delta = 1.5, \beta = 0.1$ and $\Delta = -0.1$ in Figures 5.5 and 5.6, and for $\delta = 0.2, \beta = 0.5$ and $\Delta = -0.1$ in Figures 5.7 and 5.8. Numerical results for $\Delta = -0.01$ and the same values of δ and β are qualitatively similar. The comparison between the predicted and numerical values shown in Table 5.3 is now very good. In some simulations, the results were qualitatively similar to Figure 4, when two wave packets can be seen in the v-component, but one of them is too small to be seen in the u-component.

Simulation	N	L	Δt	Δ	β	δ	α	λ	a	b
4	2048	1500	0.0001	-0.01	0.1	1.5	-0.75	-0.5	0.75	3
5	2048	1500	0.0001	-0.1	0.1	1.5	-0.75	-0.5	0.75	3
6	2048	800	0.0001	-0.01	0.5	0.2	-0.1	-0.5	3	-1
7	2048	800	0.0001	-0.1	0.5	0.2	-0.1	-0.5	3	-1

TABLE 5.3: Simulation parameters for the non-symmetric case

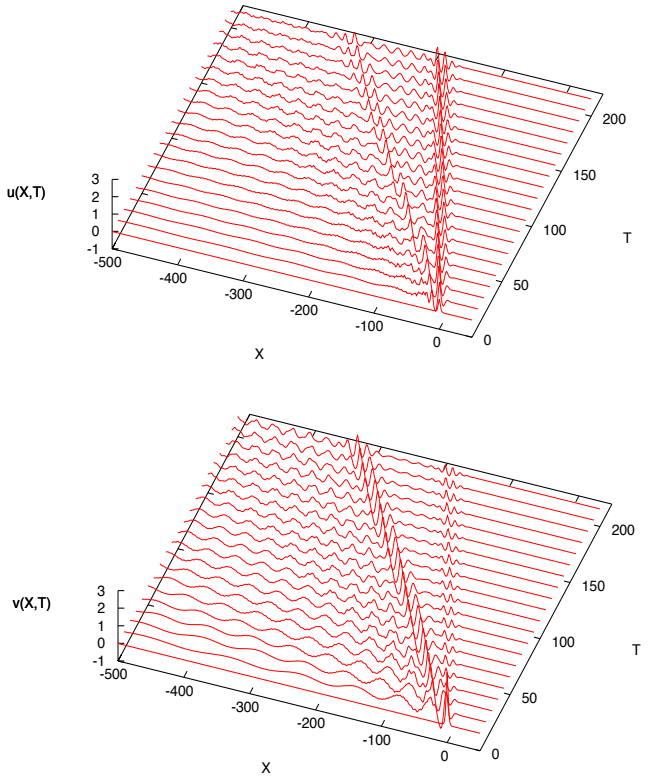

FIGURE 5.5: Numerical simulations for the non-symmetric case ($N_1 \neq N_3$) using a KdV initial condition of weak coupling with the parameter $\delta = 1.5$, $\Delta = -0.1$, $a = 0.75$ and $b = 3$.

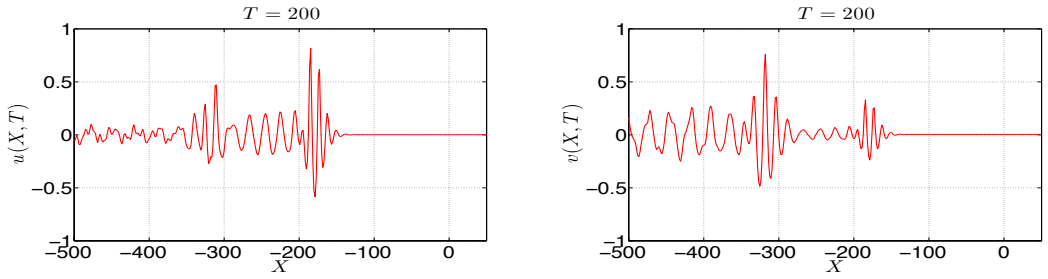

FIGURE 5.6: Same as Figure 5.5, but a cross-section at $T = 200$ for both modes.

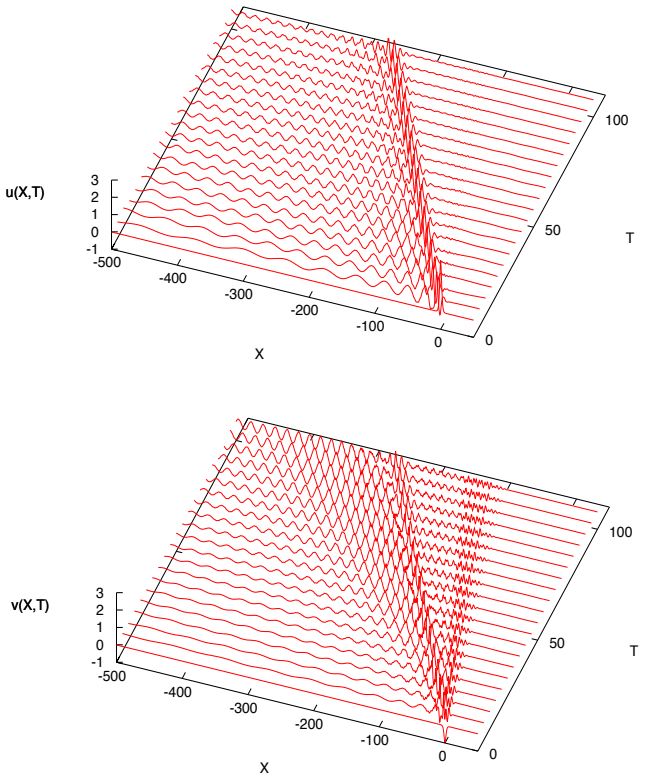

FIGURE 5.7: Numerical simulations for the non-symmetric case ($N_1 \neq N_3$) using a KdV initial condition of weak coupling with the parameter $\delta = 0.2$, $\Delta = -0.1$, $a = 3$ and $b = -1$.

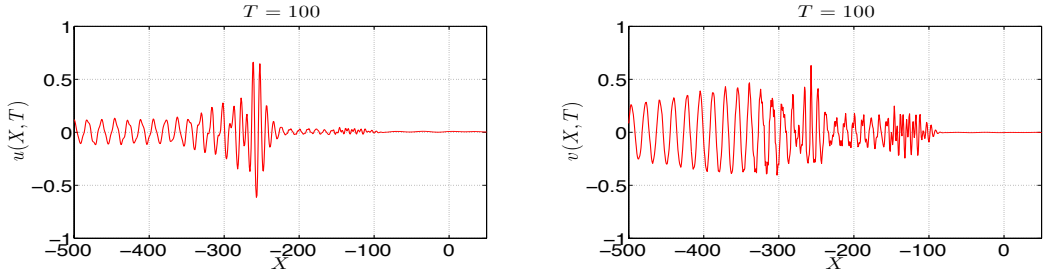

FIGURE 5.8: Same as Figure 5.7, but a cross-section at $T = 100$ for both modes.

Data	c_{g1}	C_{g1}	c_{g2}	C_{g2}	r_1	R_1	r_2	R_2
4	−0.844	−0.857	−1.521	−1.536	1.881	1.938	0.778	0.655
5	−0.876	−0.881	−1.579	−1.548	2.450	2.333	0.498	0.370
6	−0.932	−0.947	−2.520	−2.579	0.118	0.125	1.669	1.622
7	−1.017	−1.026	−2.523	−2.526	0.129	0.143	1.254	1.243

TABLE 5.4: Numerically determined group velocities, $C_{g1,g2}$ and modal ratio $R_{1,2}$ versus theoretical predictions $c_{g1,g2}$ and ratio $r_{1,2}$ for each case.

5.4 Conclusion

In this chapter we evaluated the coefficients of coupled Ostrovsky equations for the case of a three-layer stratification in the absence of shear flow. This is an extension of the special case considered by Gear and Grimshaw [39]. Within the scope of this and similar models of the density stratification, both branches of the dispersion relation of the linearised equations resemble the dispersion curve of a typical single Ostrovsky equation, with no spectral gaps, and with an extremum in both group velocity curves. Importantly, in all the cases shown here these extrema are distinct. Hence, based on the results for the single Ostrovsky equation obtained by Grimshaw and Helfrich [1], it was expected to observe the emergence of two separated nonlinear wave packets associated with the extrema in these group velocity curves.

This generic outcome has been confirmed in the numerical simulations, using a pseudo-spectral code, and initiated using solitary-type initial conditions. As for the single Ostrovsky equation, it is expected that each of these wave packets can be described by an extended nonlinear Schrödinger equation, although the derivation of that asymptotic reduction is beyond the scope of this research. Of course, at early times, for example around $T = 10\,\text{to}\,20$ in Figure 5.3, there is an interaction between these wave packets, and indeed, there is continuing small-amplitude radiation from the leading wave packet which does then interact with

the second wave packet. But this does not seem to greatly affect its coherence as a stable and persistent nonlinear wave packet.

In the oceanic context, it might be helpful to show an example of some more realistic model. Therefore, the extension of the work from this chapter will include the shear flow and density stratification and provide such an example.

Chapter 6

Coupled Ostrovsky equations for internal waves in a three-layer shear flow

6.1 Introduction

This chapter is devoted to studying the effects of a nonzero shear flow when $u_0(z) \neq 0$. This is an extension of the previous work for coupled KdV equations, particularly in Grimshaw [67], Grimshaw and Skyrnnikov [68], Grimshaw [40]. A very useful model which will be considered here is a fluid consisting of three layers when the middle layer depth is much greater than upper layer and the lower one. The density and shear flow are presented as piecewise-constant and then we will obtain the coefficients of the system of coupled Ostrovsky equations for this model.

Our analysis shows that the dispersion relation of the system of coupled Ostrovsky equations discloses various behaviours of weakly nonlinear oceanic internal waves including the existence of unsteady and steady wave packets. The shear flow allows for a configuration when initial solitary-like waves in the coupled system are

destroyed, and replaced by a variety of nonlinear envelope wave packets, extending the scenarios previously studied in the absence of the shear flow in Chapter 5.

6.2 Analysis

6.2.1 Three-layer shear flow

As an illustrative example with sufficient parameters to explore several cases of interest, a three-layer fluid is considered, $-h < z < 0$, with interfaces at $z = -h_2 - h_1, z = -h_1$, and $h = h_1 + h_2 + h_3$, as shown in Figure 6.1. Here, ρ_0 and u_0 are piecewise-constant density and velocity fields, respectively, and they are represented using the Heaviside step function as follows:

$$\rho_0(z) = \rho_3 + (\rho_2 - \rho_3)H(z + h_2 + h_1) + (\rho_1 - \rho_2)H(z + h_1)\,,$$

$$u_0(z) = U_3 + (U_2 - U_3)H(z + h_2 + h_1) + (U_1 - U_2)H(z + h_1)\,.$$

With rigid boundaries at $z = -h, 0$, the modal functions are given by:

$$\begin{aligned}
&\phi = A_3\frac{h+z}{h_3}\,, \quad -h < z < -h_2 - h_1\,,\\
&\phi = A_1\frac{h_1+h_2+z}{h_2} - A_3\frac{h_1+z}{h_2}\,, \quad -h_2 - h_1 < z < -h_1\,,\\
&\phi = -A_1\frac{z}{h_1}\,, \quad -h_1 < z < 0\,.
\end{aligned} \tag{6.1}$$

This is normalized so that $\phi = A_{1,3}$ at $z = -h_1, -h_1 - h_2$. At each interface there is the density jump relation:

$$[\rho_0(c - u_0)^2\phi_z] = g[\rho_0]\phi\,.$$

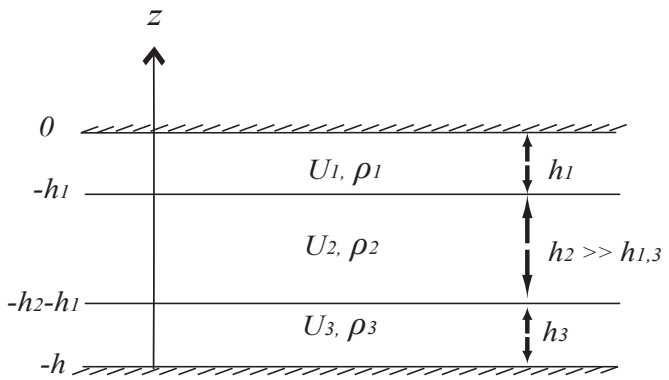

FIGURE 6.1: A schematic representation of the three-layer model with a shear flow.

This yields the system:

$$\{\frac{\rho_1(c-U_1)^2}{h_1}+\frac{\rho_2(c-U_2)^2}{h_2}-g(\rho_2-\rho_1)\}A_1-\frac{\rho_2(c-U_2)^2}{h_2}A_3 = 0\,, \quad (6.2)$$

$$-\frac{\rho_2(c-U_2)^2}{h_2}A_1+\{\frac{\rho_3(c-U_3)^2}{h_3}+\frac{\rho_2(c-U_2)^2}{h_2}-g(\rho_3-\rho_2)\}A_3 = 0\,, \quad (6.3)$$

which can be written as

$$D_1A_1-D_2A_3=0\,, \quad -D_2A_1+D_3A_3=0\,, \quad (6.4)$$

$$D_1=\frac{\rho_1(c-U_1)^2}{h_1}+\frac{\rho_2(c-U_2)^2}{h_2}-g(\rho_2-\rho_1)\,, \quad (6.5)$$

$$D_3=\frac{\rho_3(c-U_3)^2}{h_3}+\frac{\rho_2(c-U_2)^2}{h_2}-g(\rho_3-\rho_2)\,, \quad (6.6)$$

$$D_2=\frac{\rho_2(c-U_2)^2}{h_2}\,. \quad (6.7)$$

Without loss of generality we put $U_2=0$ henceforth.

The dispersion relation, determining the speed c is then:

$$D_1D_3=D_2^2\,. \quad (6.8)$$

A resonance with two distinct modes requires that $D_1=D_3=D_2=0$ simultaneously. There are two cases, either $c=0$ or $h_2\gg h_{1,3}$. The first case contains

implicit critical layers, and hence is not considered here. The second case is,

$$h_2 \gg h_{1,3}\,, \quad c = U_1 \pm \{\frac{gh_1(\rho_2-\rho_1)}{\rho_1}\}^{1/2} = U_3 \pm \{\frac{gh_3(\rho_3-\rho_2)}{\rho_3}\}^{1/2}\,. \tag{6.9}$$

For given densities $\rho_{1,2,3}$ and layer depths $h_{1,3}$, these determine the allowed shear $U_1 - U_3$. There are four cases, but to avoid a critical layer we must choose $c > 0$, which then imposes a constraint on the allowed choices for $U_1 - U_3$.

The modal functions and their derivatives are given by:

$$\begin{aligned}
\phi_1 = 0\,, \quad \phi_{1z} = 0\,, \quad & -h < z < -h_2 - h_1\,, \\
\phi_1 = \frac{h_1+h_2+z}{h_2}\,, \quad \phi_{1z} = \frac{1}{h_2}\,, \quad & -h_2 - h_1 < z < -h_1\,, \\
\phi_1 = -\frac{z}{h_1}\,, \quad \phi_{1z} = -\frac{1}{h_1}\,, \quad & -h_1 < z < 0\,,
\end{aligned} \tag{6.10}$$

$$\begin{aligned}
\phi_2 = \frac{h+z}{h_3}\,, \quad \phi_{2z} = \frac{1}{h_3}\,, \quad & -h < z < -h_2 - h_1\,, \\
\phi_2 = -\frac{h_1+z}{h_2}\,, \quad \phi_{2z} = -\frac{1}{h_2}\,, \quad & -h_2 - h_1 < z < -h_1\,, \\
\phi_2 = 0\,, \quad \phi_{2z} = 0\,, \quad & -h_1 < z < 0\,.
\end{aligned} \tag{6.11}$$

Now all coefficients in the coupled Ostrovsky equation can be calculated, by taking into account $h_2 \gg h_1, h_3$ where appropriate:

$$I_1\mu_1 = -\frac{3\rho_1(c-U_1)^2}{h_1^2}\,, \quad I_2\mu_2 = \frac{3\rho_3(c-U_3)^2}{h_3^2} \tag{6.12}$$

$$I_1\lambda_1 = I_2\lambda_2 = \frac{c^2\rho_2 h_2}{3}\,, \tag{6.13}$$

$$I_1 = \frac{2\rho_1(c-U_1)}{h_1}\,, \quad I_2 = \frac{2\rho_3(c-U_3)}{h_3}\,, \tag{6.14}$$

$$\lambda_{12} = \lambda_{21} = \frac{c^2\rho_2\ h_2}{6}\,, \tag{6.15}$$

$$\nu_1 = \nu_2 = 0\,. \tag{6.16}$$

For the coefficients $\gamma_{1,2,12}$ we must evaluate $\Phi_{1,2}$:

$$\Phi_{1,2} = \phi_{1z,2z} - \frac{(\rho_0 u_0)_z}{\rho_0 W}\phi_{1,2}\,, \tag{6.17}$$

$$I_i\gamma_i = \tilde{f}^2 \int_{-h}^{0} \rho_0 \Phi_i \phi_{iz}\, dz\,, \tag{6.18}$$

$$\gamma_{ij} = \tilde{f}^2 \int_{-h}^{0} \rho_0 \Phi_i \phi_{jz}\, dz\,. \tag{6.19}$$

Here $\rho_0, W = c - u_0$ are piecewise constant, so the second term in (6.17) behaves like a δ-function. Specifically, we write:

$$\Phi_{1,2} = \phi_{1z,2z} + \{(\log|W|)_z - \frac{u_0}{W}(\log\rho_0)_z\}\phi_{1,2}\,,$$

where the last term can be ignored in the Boussinesq approximation, but is kept here, and we treat $\log|W|$ and $\log\rho_0$ as piecewise-constant functions. The derivatives of $[\cdots]$ are δ-functions, leading to the product of a δ-function with a discontinuous function in (6.18, 6.19). In order to evaluate these expressions it is first noted that ϕ_{1z}, ϕ_{2z} are zero except in the upper and bottom layer respectively, where they are constants, and also $\Phi_1 = 0$ in the bottom layer, and $\Phi_2 = 0$ in the top layer. Hence:

$$\begin{aligned} I_1\gamma_1 &= -\frac{\rho_1\tilde{f}^2}{h_1}\int_{-h}^{0} \Phi_1 H(z+h_1)\, dz \\ &= \frac{\rho_1\tilde{f}^2}{h_1}\{1 + \frac{1}{2}\log(\frac{|W_2|}{|W_1|}) - \frac{U_1}{2W_1}\log(\frac{\rho_2}{\rho_1})\}\,, \qquad (6.20) \\ I_2\gamma_2 &= \frac{\rho_3\tilde{f}^2}{h_3}\int_{-h}^{0} \Phi_2 H(-z-h_1-h_2) dz \\ &= \frac{\rho_3\tilde{f}^2}{h_3}\{1 + \frac{1}{2}\log(\frac{|W_2|}{|W_3|}) - \frac{U_3}{2W_3}\log(\frac{\rho_2}{\rho_3})\}\,, \qquad (6.21) \\ \gamma_{12} &= \gamma_{21} = 0\,. \qquad (6.22) \end{aligned}$$

Here we have used the expression that when a δ-function multiplies a discontinuous function $f(x)$:

$$\int f(x)\delta(x)dx = \frac{1}{2}(f(0+) + f(0-))\,.$$

Next, letting $g_1 = g(\rho_2 - \rho_1)/\rho_1$, $g_3 = g(\rho_3 - \rho_2)/\rho_3$ and using the Boussinesq approximation that otherwise $\rho_1 \approx \rho_2 \approx \rho_3$, it is then obtained that

$$
\begin{aligned}
n &= m = p = q = \gamma = \nu = 0\,, && (6.23)\\
\delta &= \frac{h_3(c-U_1)}{h_1(c-U_3)} = -2\alpha\,, \quad \lambda = -\frac{1}{2}\,, && (6.24)\\
\beta &= \frac{c^2 h_1 h_2 \tilde{f}^2 (1 + \frac{1}{2}\log|c/(c-U_1)|)}{12(c-U_1)^2}\,, && (6.25)\\
\mu &= \frac{c^2 h_1 h_2 \tilde{f}^2 (1 + \frac{1}{2}\log|c/(c-U_3)|)}{12(c-U_1)(c-U_3)}\,, && (6.26)\\
\text{so that}\quad \mu &= \beta F\,, \quad F = (\frac{c-U_1}{c-U_3})\frac{1 + \frac{1}{2}\log|c/(c-U_3)|}{1 + \frac{1}{2}\log|c/(c-U_1)|}\,. && (6.27)
\end{aligned}
$$

Then there are four possibilities according to the value of c:

$$
\begin{aligned}
&\text{Case 1}: \quad c = U_1 + \sqrt{g_1 h_1} = U_3 + \sqrt{g_3 h_3}\,,\\
&\text{Case 2}: \quad c = U_1 - \sqrt{g_1 h_1} = U_3 - \sqrt{g_3 h_3}\,,\\
&\text{Case 3}: \quad c = U_1 + \sqrt{g_1 h_1} = U_3 - \sqrt{g_3 h_3}\,,\\
&\text{Case 4}: \quad c = U_1 - \sqrt{g_1 h_1} = U_3 + \sqrt{g_3 h_3}\,.
\end{aligned} \qquad (6.28)
$$

Considering the right-propagating waves and bearing in mind that a piecewise-constant shear flow is a simplified model of a continuous shear flow, then in order to avoid an implicit critical layer, we require that $c > \max[U_1, 0, U_3]$, where it is recalled that we have set $U_2 = 0$. This condition then implies that we consider Case 1.

In full detail, for Case 1:

$$
\begin{aligned}
\delta &= \sqrt{\frac{g_1 h_3}{g_3 h_1}} = -2\alpha\,, \quad \lambda = -\frac{1}{2}\,, && (6.29)\\
\beta &= \frac{h_2 \tilde{f}^2 (\sqrt{g_1 h_1} + U_1)^2 (1 + \frac{1}{2}\log|(\sqrt{g_1 h_1} + U_1)/\sqrt{g_1 h_1}|)}{12 g_1}\,, && (6.30)\\
\mu &= \beta F\,, \quad F = \sqrt{\frac{g_1 h_1}{g_3 h_3}}\frac{(1 + \frac{1}{2}\log|(\sqrt{g_3 h_3} + U_3)/\sqrt{g_3 h_3}|)}{(1 + \frac{1}{2}\log|(\sqrt{g_1 h_1} + U_1)/\sqrt{g_1 h_1}|)}\,. && (6.31)
\end{aligned}
$$

Note that $\beta > 0$ unless U_1 is such that:

$$|1 + \frac{U_1}{\sqrt{g_1 h_1}}| < e^{-2}\,, \quad -1 < \frac{U_1}{\sqrt{g_1 h_1}} < e^{-2} - 1 = -0.865\,,$$

when $\beta < 0$. Similarly $\mu > 0$ unless U_3 is such that:

$$|1 + \frac{U_3}{\sqrt{g_3 h_3}}| < e^{-2}\,, \quad -1 < \frac{U_3}{\sqrt{g_3 h_3}} < e^{-2} - 1 = -0.865\,,$$

when $\mu < 0$. But note that U_1, U_3 are constrained by the resonance condition (6.28). Nevertheless, all four possibilities can be realised, that is; Case A: $\beta > 0, \mu > 0$, Case B: $\beta > 0, \mu < 0$, Case C: $\beta < 0, \mu > 0$, Case D: $\beta < 0, \mu < 0$.

Specifically, we choose $\tilde{f} = 5 \times 10^{-3}\, s^{-1}$ and choose $g_{1,3}$ of the order $10^{-1} \leftrightarrow 10^{-3}\, m\, s^{-2}$. The upper layer and lower depths $h_{1,3}$ are chosen to be of order $50 \leftrightarrow 1000\, m$. Next, we choose U_1 and use the resonance condition (6.28) to determine the value of U_3, since U_1 and U_3 are not independent. Finally, h_2 is a free parameter, so β can be chosen arbitrarily, but then $\mu = \beta F$ is determined. Typically, we choose β so that $h_2 \gg h_{1,3}$ but of order $4 \leftrightarrow 6\, km$. For instance, choose $U_1 = 1\, ms^{-1}$, $h_1 = 50\, m$, $g_1 = 0.1\, ms^{-2}$, and then $\beta > 0$; in this case, also $\mu > 0$ when $\sqrt{g_3 h_3} < 23.97$, and $\mu < 0$ when $\sqrt{g_3 h_3} > 23.97$, on using the resonance condition (6.28) to determine $U_3 = 3.236 - \sqrt{g_3 h_3}$. Alternatively, choose $U_1 = -1.8\, ms^{-1}$, $h_1 = 500\, m$, $g_1 = 0.01\, ms^{-2}$, and again $\beta > 0$, but now $U_3 = 0.436 - \sqrt{g_3 h_3}$, so that $\mu < 0$ when $\sqrt{g_3 h_3} > 3.22$, which is a more realistic value. Next, choose U_1 so that $-1 < U_1/\sqrt{g_1 h_1} < -0.865$, for instance $U_1 = -1.8\, ms^{-1}$, $h_1 = 800\, m$, $g_1 = 0.005\, ms^{-2}$ and then $\beta < 0$; in this case $U_3 = 0.2 - \sqrt{g_3 h_3}$, so that $\mu > 0$ when $\sqrt{g_3 h_3} < 1.48$, and $\mu < 0$ when $\sqrt{g_3 h_3} > 1.48$. Alternatively, choose $U_1 = -1.4\, ms^{-1}$, $h_1 = 1000\, m$, $g_1 = 0.0025\, ms^{-2}$ and then again $\beta < 0$; but now $U_3 = 0.181 - \sqrt{g_3 h_3}$, so that $\mu > 0$ when $\sqrt{g_3 h_3} < 1.34$, and $\mu < 0$ when $\sqrt{g_3 h_3} > 1.34$.

Notice that the type of current model considered in our three-layer model with shear flow can also lead to the anomalous version of the single Ostrovsky equation when $\lambda\gamma < 0$. Detailed explanation is given in Appendix A.

6.2.2 Linear dispersion relation

As in Chapter 4, the structure of the linear dispersion relation is obtained by seeking solutions of the linearised equations proportional to $e^{ik(X-c_pT)}$, where k is the wavenumber and $c_p(k)$ is the phase speed. The result is:

$$(c_p - C_1(k))u_0 + (\alpha k^2 - \frac{\gamma}{k^2})v_0 = 0\,, \tag{6.32}$$

$$(\lambda k^2 - \frac{\nu}{k^2})u_0 + (c_p - C_2(k))v_0 = 0\,, \tag{6.33}$$

$$\text{where} \quad C_1(k) = -k^2 + \frac{\beta}{k^2}\,, \quad C_2(k) = \Delta - \delta k^2 + \frac{\mu}{k^2}\,. \tag{6.34}$$

The determinant of this 2×2 system yields the dispersion relation:

$$(c_p - C_1(k))(c_p - C_2(k)) = D(k) = (\alpha k^2 - \frac{\gamma}{k^2})(\lambda k^2 - \frac{\nu}{k^2})\,. \tag{6.35}$$

Solving this dispersion relation we obtain the two branches of the dispersion relation:

$$c_p = c_{p1,p2} = \frac{C_1 + C_2}{2} \pm \frac{1}{2}\{4D + (C_1 - C_2)^2\}^{1/2}\,. \tag{6.36}$$

Here $C_{1,2}(k)$ are the linear phase speeds of the uncoupled Ostrovsky equations, obtained formally by setting the coupling term $D(k) = 0$. If $D(k) > 0$ for all k, then both branches are real-valued for all wavenumbers k, and the linearised system is spectrally stable. Here $\gamma = \nu = 0$ and $\alpha\lambda > 0$ so that $D(k) = \alpha\lambda k^4 > 0$ for all k.

Consider now Case 1, where $c > 0, I_1 > 0, I_2 > 0$, and so $\lambda_{1,2} > 0$, so that $\delta > 0$, and $0 < \alpha\lambda = \delta/4$. Also recall that $\Delta < 0$ without loss of generality. The main effect of the background shear is that now $\beta \neq \mu$, and indeed each can be either positive or negative. Then (6.36) reduces to

$$c_{p1,p2} = \frac{\beta + \mu}{2k^2} + \frac{\Delta}{2} - \frac{(1+\delta)k^2}{2} \pm \frac{1}{2}\sqrt{(\frac{\beta - \mu}{k^2} - \Delta - (1-\delta)k^2)^2 + 4\alpha\lambda k^4}. \tag{6.37}$$

The group velocities are given by $c_g = d(kc_p)/dk$,

$$c_{g1,g2} = -\frac{\beta+\mu}{2k^2} + \frac{\Delta}{2} - \frac{3(1+\delta)k^2}{2} \pm \frac{\{\Delta + (1-\delta)k^2 - \frac{\beta-\mu}{k^2}\}\{\frac{3}{2}(1-\delta)k^2 + \frac{1}{2}(\Delta + \frac{\beta-\mu}{k^2})\} + 6\alpha\lambda k^4}{\sqrt{(\Delta + (1-\delta)k^2 - \frac{\beta-\mu}{k^2})^2 + 4\alpha\lambda k^4}}. \quad (6.38)$$

Next it is useful to examine the limits $k \to 0, \infty$. Thus,

$$c_{p1,p2} \to \frac{F_{1,2}}{k^2} \quad \text{and} \quad c_{g1,g2} \to -\frac{F_{1,2}}{k^2} \quad \text{as} \quad k \to 0\,, \quad (6.39)$$

$$c_{p1,p2} \to E_{1,2}\,k^2 \quad \text{and} \quad c_{g1,g2} \to 3E_{1,2}\,k^2 \quad \text{as} \quad k \to \infty\,, \quad (6.40)$$

where

$$2F_{1,2} = \beta + \mu \pm |\beta - \mu|\,, \quad (6.41)$$

$$2E_{1,2} = -(1+\delta) \pm \{(1-\delta)^2 + 4\alpha\lambda\}^{1/2}. \quad (6.42)$$

Note that since $0 < \alpha\lambda < \delta$, $E_2 < E_1 < 0$. One can see that there are four possibilities of qualitatively different behaviour of the dispersion relation, depending on the signs of the coefficients β and μ, as Case A: $\beta > 0, \mu > 0$, Case B: $\beta > 0, \mu < 0$, Case C: $\beta < 0, \mu > 0$, Case D: $\beta < 0, \mu < 0$.

Note again that with the scaling (3.29), X, T are scaled variables and have dimensions of $C^{-1/2}, C^{-3/2}$ respectively, where C is a velocity scale, i.e ms^{-1} . The dependent variables u and v have the dimension of C. The coefficients $n, m, \alpha, \delta, p, q, \lambda$ are dimensionless, while β, γ, μ, ν have dimensions of C^2, and Δ has the dimension of C. The wavenumber k and c_p, c_g have the dimensions of $C^{1/2}$ and C respectively. In what follows we omit writing the dimensions for the scaled variables, but write the unscaled physical parameters in dimensional form.

6.2.2.1 Case A: $(\beta > 0\,, \mu > 0)$

Case A happens when $\beta > 0$ and $\mu > 0$. Then $F_1 = \max[\beta\,, \mu] > F_2 = \min[\beta\,, \mu] > 0$. There is no spectral gap in either mode, and this case is similar to the situation

without any background shear, which has been discussed in Chapter 5. But there is now a significant difference since here $\beta \neq \mu$ due to the effect of the background shear flow. A typical dispersion curve is shown in Figure 6.2, where $\beta = 1\,, \mu = 0.604\,, \Delta = -0.5\,, \delta = 1.414\,, \alpha = -0.707\,, \lambda = -0.5$ when setting $h_1 = 50\,m\,, h_2 \approx 3.9\,km\,, h_3 = 100\,m\,,\ g_1 = g_3 = 0.1\,ms^{-2}\,,\ U_1 = 1\,m\,s^{-1}\,, U_3 = 0.074\,m\,s^{-1}\,, \rho_1 = 0.99\,\rho_2$ and $\rho_3 = 1.01\,\rho_2$. Here, and in the subsequent plots of dispersion curves, the letters $A\,, B, \cdots$ indicate the turning points and possible resonant points, identified for comparison with the numerical results. For both modes the group velocities are negative for all k, and each has a single turning point at $k = k_{m1,m2}$ respectively. In general it is possible that there are $0\,, 2\,, 4\,, \cdots$ turning points for c_p where $dc_p/dk = 0$ and $c_p = c_g$. Each such turning point can generate a generalised envelope solitary wave, see Grimshaw and Gerard [50] for instance. Further it is also possible that there are $1\,, 3\,, 5\,, \cdots$ turning points for c_g where $dc_g/dk = 0$, and each such turning point is expected to generate an unsteady wave packet analogous to those found by Grimshaw and Helfrich [1] for the single Ostrovsky equation. Figure 2 shows the simplest case when there are $0\,, 1$ turning points respectively. But since there are four independent parameters $\beta\,, \mu\,, \Delta\,, \alpha\lambda$ (note that $\delta = -2\alpha\,, \lambda = -0.5$, see (6.29)) in the expressions (6.37, 6.38) for $c_p\,, c_g$ respectively, it cannot be ruled out that there is a possibility that other "non-typical" cases may occur. Even though the expressions (6.37, 6.38) are explicit, a full exploration of the 4-dimensional parameter space is beyond the scope of the present study. Nevertheless an asymptotic expansion in the parameter $\alpha\lambda \ll 1$ described below confirms that only the typical case arises in this asymptotic regime.

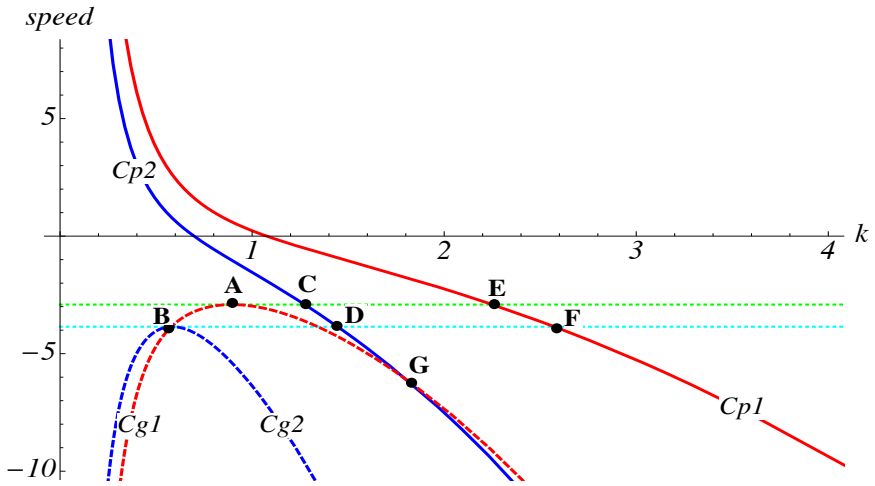

FIGURE 6.2: Typical dispersion curve for Case A with $\delta = 1.414\,, \alpha = -0.707\,, \lambda = -0.5\,, \Delta = -0.5\,, \beta = 1$ and $\mu = 0.604\,.$

Point	*Speed*	*Wavenumber*, k	*Ratio*, u_0/v_0
A	$-2.912\vert_{max\,Cg_1}$	0.895	$3.692\vert_{Cp_1}$
B	$-3.854\vert_{max\,Cg_2}$	0.584	$-0.132\vert_{Cp_2}$
C	$-9.628\vert_{Cg_2}$	1.274	$-0.602\vert_{Cp_2}$
D	$-12.131\vert_{Cg_2}$	1.446	$-0.659\vert_{Cp_2}$
E	$-9.135\vert_{Cg_1}$	2.251	$1.829\vert_{Cp_1}$
F	$-11.786\vert_{Cg_1}$	2.574	$1.788\vert_{Cp_1}$
$G_{1,2}$	$-6.118\vert_{Cg_1}$ $-18.501\vert_{Cg_2}$	1.806	$1.938\vert_{Cp_1}$ $-0.730\vert_{Cp_2}$

TABLE 6.1: Values of the group speed, wavenumber and ratio, calculated using the phase speed, at each point in Figure 6.2.

6.2.2.2 Case B: $(\beta > 0\,, \mu < 0)$

Case B occurs when $\beta > 0$ and $\mu < 0$. Then $F_1 = \beta > 0\,, F_2 = \mu < 0$. A typical dispersion curve is shown in Figure 6.3, where $\beta = 0.04\,, \mu = -0.02\,, \Delta = -1.5\,, \delta = 1\,, \alpha = -0.5\,, \lambda = -0.5$ when setting $h_1 = 500\,m\,, h_2 \approx 5.5\,km\,, h_3 = 1000\,m$, $g_1 = 0.01\,ms^{-2}\,, g_3 = 0.02\,ms^{-2}\,, U_1 = -1.8\,m\,s^{-1}\,, U_3 = -4.036\,m\,s^{-1}\,,$ $\rho_1 = 0.999\,\rho_2$ and $\rho_3 = 1.002\,\rho_2\,.$ There is no spectral gap in mode 1, and the group velocity is negative for all k with a turning point at $k = k_{m1}$. But mode 2 has a spectral gap, as the phase speed has a maximum value, c_{s2} at $k = k_{s2}$. For this mode the group velocity is positive as $k \to 0$ and negative as $k \to \infty$. At the

value $c_{p2} = c_{s2}$, the phase and group velocities are equal, and then this mode 2 can support a steady wave packet. However, this wave packet lies in the spectrum of mode 1, and hence may decay by radiation into mode 1; strictly, it is a generalised solitary wave. Here, in general it is possible that there are $0\,,2\,,4\,,\cdots$ turning points for c_p for mode 1, and $1\,,3\,,5\,,\cdots$ for mode 2. Further it is also possible here that there are $1\,,3\,,5\,,\cdots$ turning points for c_g in mode 1, and $0\,,2\,,4\,,\cdots$ for mode 2. However, the asymptotic expansion in the parameter $\alpha\lambda \ll 1$ described below confirms that only the typical case $0\,,1\,,1\,,0$ of turning points arises in this asymptotic regime.

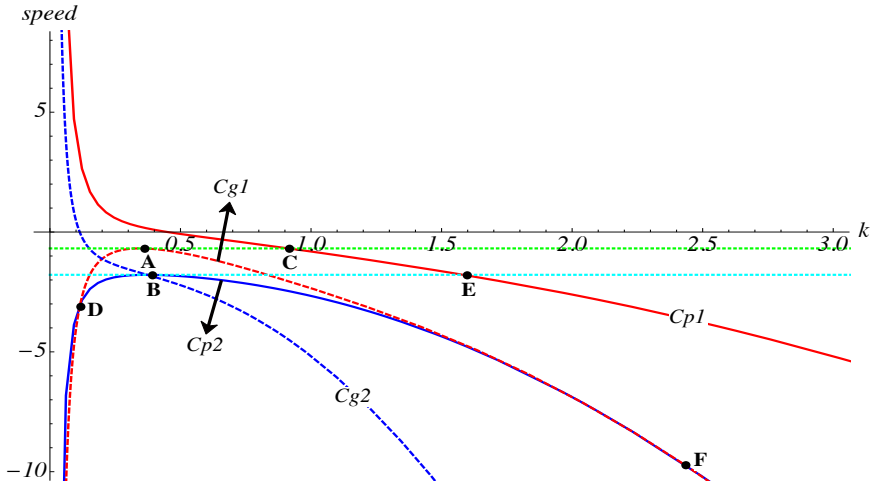

FIGURE 6.3: Typical dispersion curve for Case B with $\delta = 1\,, \alpha = -0.5\,, \lambda = -0.5\,, \Delta = -1.5\,, \beta = 0.04$ and $\mu = -0.02\,.$

Point	*Speed*	*Wavenumber*, k	*Ratio*, u_0/v_0
A	$-0.683\|_{max\, Cg_1}$	0.345	$33.696\|_{Cp_1}$
B	$-1.785\|_{max\, Cp_2=Cg_2}$	0.372	$-0.036\|_{Cp_2}$
C	$-2.0430\|_{Cg_1}$	0.914	$4.012\|_{Cp_1}$
$D_{1,2}$	$-2.987\|_{Cg_1}$ $-0.068\|_{Cg_2}$	0.117	$871.768\|_{Cp_1}$ $-0.001\|_{Cp_2}$
E	$-4.676\|_{Cg_1}$	1.583	$1.779\|_{Cp_1}$
$F_{1,2}$	$-9.722\|_{Cg_1}$ $-27.297\|_{Cg_2}$	2.433	$1.287\|_{Cp_1}$ $-0.778\|_{Cp_2}$

TABLE 6.2: Values of the group speed, wavenumber and ratio, calculated using the phase speed, at each point for Figure 6.3.

6.2.2.3 Case C: $(\beta < 0\,, \mu > 0)$

Case C happens when $\beta < 0$ and $\mu > 0$. Then $F_1 = \mu > 0, F_2 = \beta < 0$. Two examples of case C are shown here with the dispersion relation.

Example 1:

A typical dispersion curve is shown in Figure 6.4, where $\beta = -1\,,\ \mu = 0.56\,,\ \Delta = -0.5\,,\ \delta = 1.414\,, \alpha = -0.707\,,\ \lambda = -0.5$ when we set $h_{1,3} = 50\,m\,,\ g_1 = 0.1\,ms^{-2}$, $g_3 = 0.05\,ms^{-2}$, $U_1 = -2\,m\,s^{-1}, U_3 = -1.345\,m\,s^{-1}\,, \rho_1 = 0.99\,\rho_2$ and $\rho_3 = 1.005\,\rho_2$. However, this does not correspond to the realistic model for ocean since the value of $h_2 \approx 7$ x $10^6\,km$ which is too deep as the average depth of the ocean is around $4\,km$. As for case B, this is the typical case when there are $0, 1, 1, 0$ turning points for $c_{p1}, c_{p2}, c_{g1}, c_{g2}$, and the asymptotic analysis described below confirms that this is the only case when $\alpha\lambda \ll 1$. But, it is interesting to note that there is a "flat" part in mode 1 for c_{g1}, which suggests there is almost a turning point in c_{g1} around that point, called C in the Figure 6.4. We infer that an unsteady nonlinear wave packet might emerge from this point. This "flat" part can be interpreted as due to the existence of three turning points in the curve for c_{g1} and coalescence of two of these as the available parameters are varied. Indeed, by varying the parameters Δ, β, μ, cases can be found for which c_{g1} has three turning points, see Figure 6.5 with the value of h_2 is more close to the realistic ocean. However, we will not show the numerical simulations for this example since it is not a relevant value for the ocean.

Example 2:

A typical dispersion curve is shown in Figure 6.5, where $\beta = -0.01\,,\ \mu = 0.002\,,\ \Delta = -0.1\,,\ \delta = 1.414\,, \alpha = -0.707\,, \lambda = -0.5$ when setting $h_1 = h_3 = 800\,m\,, h_2 \approx 4.0\,km\,,\ g_1 = 0.005\,m\,s^{-2}\,,\ g_3 = 0.0025\,ms^{-2}\,,\ U_1 = -1.8\,m\,s^{-1}\,,\ U_3 = -1.214\,m\,s^{-1}$, $\rho_1 = 0.9995\,\rho_2$ and $\rho_3 = 1.00025\,\rho_2$. At first glance, this is overall similar to case B because there is no spectral gap in mode 1, and the group velocity is negative for all k; but now the group velocity c_{g1} has three turning points, a global maximum at A, a local minimum at K and a local maximum at B. This is not the simplest case, where only one turning point is expected, but it is displayed here as

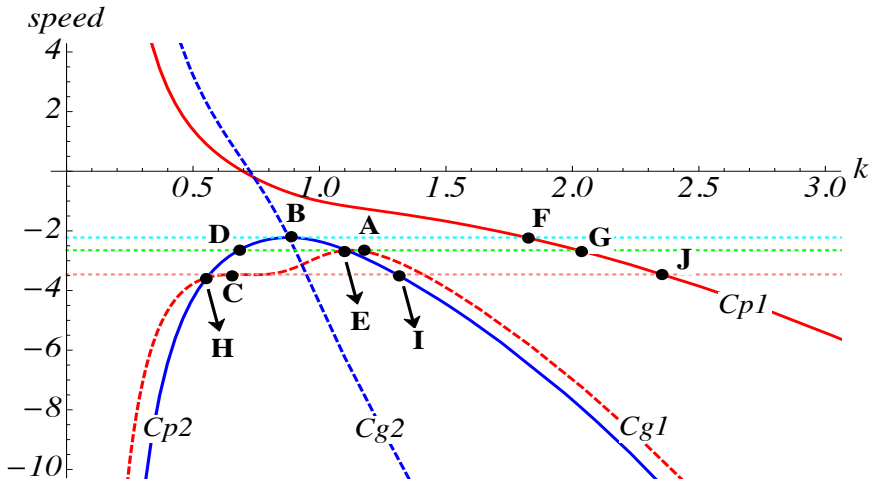

FIGURE 6.4: Typical dispersion curve for Case C with $\delta = 1.414\,, \alpha = -0.707\,, \lambda = -0.5\,, \Delta = -0.5\,, \beta = -1\,, \mu = 0.56$.

Point	*Speed*, c	*Wavenumber*, k	*Ratio*, u_0/v_0
A	$-2.650\vert_{max\, Cg_1}$	1.122	$1.028\vert_{Cp_1}$
B	$-2.223\vert_{max\, Cp_2=Cg_2}$	0.879	$-3.505\vert_{Cp_2}$
C	$-3.461\vert_{Cg_1}$	0.665	$0.109\vert_{Cp_1}$
D	$0.556\vert_{Cg_2}$	0.681	$-11.668\vert_{Cp_2}$
E	$-6.365\vert_{Cg_2}$	1.107	$-1.425\vert_{Cp_2}$
F	$-5.754\vert_{Cg_1}$	1.819	$1.685\vert_{Cp_1}$
G	$-7.143\vert_{Cg_1}$	2.024	$1.712\vert_{Cp_1}$
H	$2.114\vert_{Cg_2}$	0.565	$-0.823\vert_{Cp_2}$
I	$-9.555\vert_{Cg_2}$	1.306	$-1.031\vert_{Cp_2}$
J	$-9.702\vert_{Cg_1}$	2.357	$1.726\vert_{Cp_1}$

TABLE 6.3: Value of the group velocity, wavenumber and ratio, at each point for Figure 6.4.

potentially there could be energy focussing associated with each of these turning points, and the consequent emergence of three unsteady nonlinear wave packets. As in case B, mode 2 has a spectral gap, as the phase speed has a maximum at C; the group velocity is positive as $k \to 0$ and negative as $k \to \infty$. At this point, the phase and group velocities are equal, and so then this mode 2 can support a steady wave packet. However, this wave packet lies in the spectrum of mode 1, and hence may decay by radiation into mode 1. We will discuss the numerical results for this example in more details in the next section.

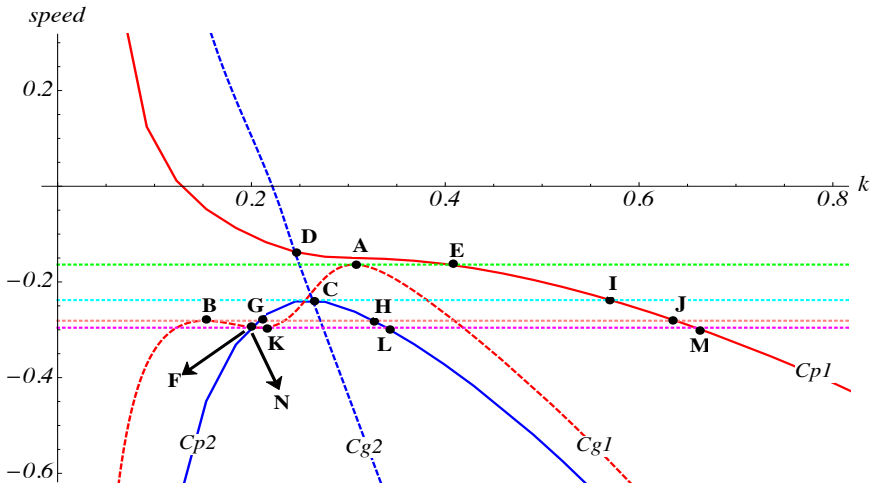

FIGURE 6.5: Typical dispersion curve for Case C with $\delta = 1.414\,, \alpha = -0.707\,, \lambda = -0.5\,, \Delta = -0.1\,, \beta = -0.01$ and $\mu = 0.002\,.$

Point	*Speed,*	*Wavenumber,* k	*Ratio,* u_0/v_0
A	$-0.164\|_{max\, Cg_1}$	0.306	$1.309\|_{Cp_1}$
B	$-0.281\|_{max\, Cg_1}$	0.152	$0.040\|_{Cp_1}$
C	$-0.238\|_{max\, Cp_2=Cg_2}$	0.259	$-2.164\|_{Cp_2}$
$D_{1,2}$	$-0.263\|_{Cg_1}$ $-0.137\|_{Cg_2}$	0.245	$0.472\|_{Cp_1}$ $-2.994\|_{Cp_2}$
E	$-0.273\|_{Cg_1}$	0.404	$1.898\|_{Cp_1}$
$F_{1,2}$	$-0.294\|_{Cg_1}$ $0.1081\|_{Cg_2}$	0.199	$0.149\|_{Cp_1}$ $-9.497\|_{Cp_2}$
G	$0.075\|_{Cg_2}$	0.206	$-7.874\|_{Cp_2}$
H	$-0.623\|_{Cg_2}$	0.326	$-0.932\|_{Cp_2}$
I	$-0.577\|_{Cg_1}$	0.571	$1.944\|_{Cp_1}$
J	$-0.722\|_{Cg_1}$	0.638	$1.914\|_{Cp_1}$
K	$-0.296\|_{min\, Cg_1}$	0.209	$0.191\|_{Cp_1}$
L	$-0.681\|_{Cg_2}$	0.339	$-0.870\|_{Cp_2}$
M	$-0.770\|_{Cg_1}$	0.659	$1.904\|_{Cp_1}$
N	$0.111\|_{Cg_2}$	0.199	$-9.651\|_{Cp_2}$

TABLE 6.4: Values of the group speed, wavenumber and ratio, calculated using the phase speed, at each point for Figure 6.5.

6.2.2.4 Case D: $(\beta < 0\,, \mu < 0)$

Case D occurs when $\beta < 0\,, \mu < 0$. Then $F_2 = \min[\beta\,, \mu] < F_1 = \max[\beta\,, \mu] < 0$. A typical dispersion curve for this case is shown in Figure 6.6, where $\beta =$

$-0.01\,, \mu = -0.02\,, \Delta = -0.5\,,\ \delta = 0.707, \alpha = -0.354, \lambda = -0.5$ when setting $h_1 = h_3 = 1000\,m, h_2 \approx 4.4\,km\,,\ g_1 = 0.0025\,m\,s^{-2}\,, g_3 = 0.005\,m\,s^{-2}\,, U_1 = -1.4\,m\,s^{-1}\,, U_3 = -2.055\,m\,s^{-1}\,, \rho_1 = 0.9998\,\rho_2$ and $\rho_3 = 1.0005\,\rho_2$. Now both modes have phase speeds with maxima $c_{s1}\,, c_{s2}$ at $k = k_{s1}\,, k_{s2}$, denoted by the points $A\,, B$ respectively. For both modes, the group velocity is positive as $k \to 0$, but negative as $k \to \infty$, and at the point of maximum phase speed, the phase and group velocities for each mode are equal. Hence a steady wave packet can exist for each mode, but will be radiating for mode 2.

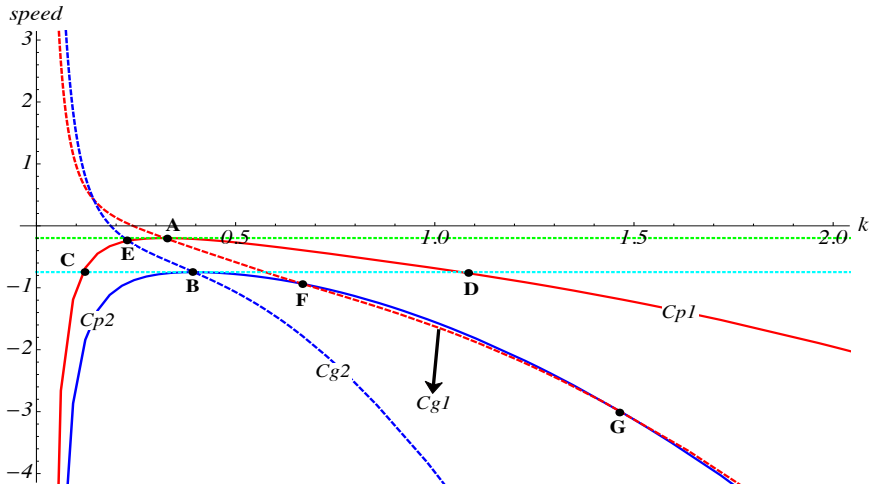

FIGURE 6.6: Typical dispersion curve for Case D with $\delta = 0.707\,, \alpha = -0.354\,, \lambda = -0.5\,, \Delta = -0.5\,, \beta = -0.01$ and $\mu = -0.02\,.$

Point	*Speed*	*Wavenumber*, k	*Ratio*, u_0/v_0
A	$-0.197\|_{max\,Cp_1=Cg_1}$	0.322	$10.973\|_{Cp_1}$
B	$-0.747\|_{max\,Cp_2=Cg2}$	0.395	$-0.105\|_{Cp_2}$
C	$0.692\|_{Cg_1}$	0.117	$180.200\|_{Cp_1}$
D	$-1.781\|_{Cg_1}$	1.066	$1.011\|_{Cp_1}$
$E_{1,2}$	$0.033\|_{Cg_1}$ $-0.241\|_{Cg_2}$	0.231	$25.339\|_{Cp_1}$ $-0.028\|_{Cp_2}$
$F_{1,2}$	$-0.931\|_{Cg_1}$ $-1.761\|_{Cg_2}$	0.664	$2.117\|_{Cp_1}$ $-0.334\|_{Cp_2}$
$G_{1,2}$	$-2.894\|_{Cg_1}$ $-8.182\|_{Cg_2}$	1.438	$0.794\|_{Cp_1}$ $-0.892\|_{Cp_2}$

TABLE 6.5: Values of the group speed, wavenumber and ratio, calculated using the phase speed, at each point for Figure 6.6.

6.3 Analysis of asymptotic expansion for turning points

As indicated above, an asymptotic expansion is used with $\epsilon = \alpha\lambda \ll 1$ to find all turning points explicitly. From (6.35), since here $\gamma = \nu = 0$:

$$(c_p - C_1(k))(c_p - C_2(k)) = \epsilon k^4\,, \tag{6.43}$$

where $C_1(k)$ and $C_2(k)$ are given in (6.34) and $\epsilon = \alpha\lambda \ll 1$. Note that the effective expansion parameter is ϵk^4 and so this can only be valid when k is also sufficiently small, say $k < 1$. Expanding in powers of ϵ then yields:

$$c_{p\tilde{i}} = C_1 + \frac{\epsilon k^4}{C_1 - C_2} - \frac{\epsilon^2 k^8}{(C_1 - C_2)^3} + \cdots\,,$$
$$c_{p\tilde{j}} = C_2 - \frac{\epsilon k^4}{C_1 - C_2} + \frac{\epsilon^2 k^8}{(C_1 - C_2)^3} + \cdots\,.$$

The derivatives are given by:

$$c_{p\tilde{i}k} = -2k - \frac{2\beta}{k^3} + \epsilon\{\frac{4k^3}{C_1 - C_2} - \frac{k^4(C_{1k} - C_{2k})}{(C_1 - C_2)^2}\} + \cdots\,, \tag{6.44}$$
$$c_{p\tilde{j}k} = -2\delta k - \frac{2\mu}{k^3} - \epsilon\{\frac{4k^3}{C_1 - C_2} - \frac{k^4(C_{1k} - C_{2k})}{(C_1 - C_2)^2}\} + \cdots\,. \tag{6.45}$$

The corresponding group velocities are found from $c_g = c_p + kc_{pk}$:

$$c_{g\tilde{i}} = -3k^2 - \frac{\beta}{k^2} + \epsilon\{\frac{5k^4}{C_1 - C_2} - \frac{k^5(C_{1k} - C_{2k})}{(C_1 - C_2)^2}\} + \cdots\,, \tag{6.46}$$
$$c_{g\tilde{j}} = \Delta - 3\delta k^2 - \frac{\mu}{k^2} - \epsilon\{\frac{5k^4}{C_1 - C_2} - \frac{k^5(C_{1k} - C_{2k})}{(C_1 - C_2)^2}\} + \cdots\,, \tag{6.47}$$
$$c_{g\tilde{i}k} = -6k + \frac{2\beta}{k^3} + \epsilon\{\frac{20k^3}{C_1 - C_2} - \frac{10k^4(C_{1k} - C_{2k})}{(C_1 - C_2)^2} - k^5\{\frac{(C_{1k} - C_{2k})}{(C_1 - C_2)^2}\}_k\} + \cdots\,, \tag{6.48}$$
$$c_{g\tilde{j}k} = -6\delta k + \frac{2\mu}{k^3} - \epsilon\{\frac{20k^3}{C_1 - C_2} - \frac{10k^4(C_{1k} - C_{2k})}{(C_1 - C_2)^2} - k^5\{\frac{(C_{1k} - C_{2k})}{(C_1 - C_2)^2}\}_k\} + \cdots\,. \tag{6.49}$$

The turning points for c_p can now be found by equating (6.44, 6.45) to zero, and those for c_g found by equating (6.48, 6.49) to zero. Consistently with this asymptotic expansion, the solutions for k are sought in the form $k = k_0 + \epsilon k_1 + \epsilon^2 k_2 + \dots$ by collecting the $O(1)$ and $O(\epsilon)$ terms. Then, we obtain the following formal asymptotic solutions:

$$c_{p\tilde{i}k} = 0 \quad : \qquad k = k_0 + \epsilon \frac{k_0^9(k_0^4(-1+\delta) - 2k_0^2\Delta + 3(\beta-\mu))}{(k_0^4 - 3\beta)(\beta + k_0^4(-1+\delta) - k_0^2\Delta - \mu)^2} + \dots$$

$$\text{with} \quad k_0 = \sqrt[4]{-\beta};$$

$$c_{p\tilde{j}k} = 0 \quad : \qquad k = k_0 - \epsilon \frac{k_0^9(k_0^4(-1+\delta) - 2k_0^2\Delta + 3(\beta-\mu))}{(k_0^4\delta - 3\mu)(\beta + k_0^4(-1+\delta) - k_0^2\Delta - \mu)^2} + \dots$$

$$\text{with} \quad k_0 = \sqrt[4]{\frac{-\mu}{\delta}};$$

$$c_{g\tilde{i}k} = 0 \quad : \qquad k = k_0 + \epsilon k_0^9 \{ \frac{3k_0^8(-1+\delta)^2 - 9k_0^6(-1+\delta)\Delta + 21(\beta-\mu)^2 + 27k_0^2\Delta(-\beta+\mu)}{3(k_0^4+\beta)(\beta + k_0^4(-1+\delta) - k_0^2\Delta - \mu)^3} + \frac{2k_0^4(4\beta(-1+\delta) + 5\Delta^2 + 4\mu(1-\delta)}{3(k_0^4+\beta)(\beta + k_0^4(-1+\delta) - k_0^2\Delta - \mu)^3} \} + \dots$$

$$\text{with} \quad k_0 = \sqrt[4]{\frac{\beta}{3}};$$

$$c_{g\tilde{j}k} = 0 \quad : \qquad k = k_0 - \epsilon k_0^9 \{ \frac{3k_0^8(-1+\delta)^2 - 9k_0^6(-1+\delta)\Delta + 21(\beta-\mu)^2 + 27k_0^2\Delta(-\beta+\mu)}{3(k_0^4\delta+\mu)(\beta + k_0^4(-1+\delta) - k_0^2\Delta - \mu)^3} - \frac{2k_0^4(4\beta(-1+\delta) + 5\Delta^2 + 4\mu(1-\delta)}{3(k_0^4\delta+\mu)(\beta + k_0^4(-1+\delta) - k_0^2\Delta - \mu)^3} \} + \dots$$

$$\text{with} \quad k_0 = \sqrt[4]{\frac{\mu}{3\delta}}.$$

The outcomes for each case are described below:

Case A: $(\beta > 0\,, \mu > 0)$

Here put $\tilde{i} = 1\,, \tilde{j} = 2$ and find that both $c_{p1k} < 0$ and $c_{p2k} < 0$. Thus there are no turning points for c_{p1} and c_{p2} in this approximation. However, $c_{g1k} = 0$ yields

just one turning point $k = k_0 + \epsilon k_1 \approx 0.868$ for the parameter values of Figure 6.2, compared to the exact value 0.895. Also $c_{g2k} = 0$ yields just one turning point $k = k_0 + \epsilon k_1 \approx 0.574$, compared to the exact value 0.584.

Case B: $(\beta > 0\,, \mu < 0)$

Here, again, put $\tilde{i} = 1\,, \tilde{j} = 2$ and find that $c_{p1k} < 0$ and so there is no turning point for c_{p1}. However, there is a single turning point for c_{p2}, given by $c_{p2k} = 0$, $k = k_0 + \epsilon k_1 \approx 0.372$, for the parameter values of Figure 6.3 compared to the exact value 0.372. Next, there is a single turning point for c_{g1} when $c_{g1k} = 0$ gives $k = k_0 + \epsilon k_1 \approx 0.345$, compared to the exact value 0.345. Since $c_{g2k} < 0$, there are no turning points for c_{g2}.

Case C: $(\beta < 0\,, \mu > 0)$

Example 1:

Here we put $\tilde{i} = 2\,, \tilde{j} = 1$ and find that $c_{p1k} < 0$ and so there is no turning point for c_{p1}. However, there is a single turning point for c_{p2}, given by $c_{p2k} = 0$, $k = k_0 + \epsilon k_1 \approx 0.308$ for the parameter values of Figure 6.4, compared to the exact value of 0.879. However, we note here that $k_0 = 1$ and the correction term ϵk_1 indicates that the asymptotic expansion is not very useful in this case. Next there is a single turning point for c_{g1} and $c_{g1k} = 0$ gives $k = k_0 + \epsilon k_1 \approx 0.633$, compared to the exact value of 1.122 that is point A in Figure 6.4. However, it is pertinent to note here that the 'flat' point C in Figure 6.4 is 0.665. Hence here it seems that the asymptotic expansion selects the point C rather than the point A for which the real expansion parameter of ϵk^4 is too large. Since $c_{g2k} < 0$ there are no stationary point in c_{g2}. Note that the detailed numerical simulations for this example are not discussed.

Example 2:

Same as example 1 by putting $\tilde{i} = 2, \tilde{j} = 1$ and find that $c_{p1k} < 0$ and so there is no turning point for c_{p1}. However, there is a single turning point for c_{p2}, given by $c_{p2k} = 0$, $k = k_0 + \epsilon k_1 \approx -0.408$ for the parameter values of Figure 6.5, compared to the exact value of 0.259. However, note here that $k_0 = 0.316$ and the correction

term $|\epsilon k_1|$ is much too large, indicating that the asymptotic expansion is not at all useful in this case. Next there is a single turning point for c_{g1} and $c_{g1k} = 0$ which gives $k = k_0 + \epsilon k_1 \approx 0.151$, compared to the exact value of 0.152 that is point B in Figure 6.5. However, note here that there also exists a minimum point K in Figure 6.5 at $k = 0.209$, and a maximum point A at $k = 0.306$ which are not found by this asymptotic analysis. Since $c_{g2k} < 0$ there are no stationary points in c_{g2}.

Case D: $(\beta < 0\,, \mu < 0)$
Here put $\tilde{i} = 1\,, \tilde{j} = 2$. There are turning points for both c_{p1}, c_{p2} and $c_{p1k} = 0, c_{p2k} = 0$ yielding $k = k_0 + \epsilon k_1 \approx 0.322, 0.392$, respectively, for the parameter values of Figure 6.6, compared to the exact values of $0.322, 0.395$. Here both $c_{g1k} < 0$ and $c_{g2k} < 0$ and hence there are no turning points in both c_{g1} and c_{g2}.

6.4 Numerical results

In this section we present some results from numerical simulations of the scaled equations (3.30 , 3.31), using the pseudo-spectral method for the four different cases, corresponding to the parameters of the linear dispersion curves described in section 6.2.2. For all cases considered here we have $n = m = p = q = \gamma = \nu = 0$.

For the initial conditions we use either an approximation to a solitary wave solution of the corresponding coupled KdV system, which is mainly suitable for Case A, or an approximation to a nonlinear wave packet, which is more suitable for Cases B,C,D. The former initial condition is described by Alias et al. [49] (see also Section 4.3), is denoted as 'weak coupling KdV solitary waves', and given by,

$$u = a\,\mathrm{sech}^2(\gamma_1 X)\,, \quad \tfrac{a}{3} = 4(1+\alpha)\gamma_1^2\,, \tag{6.50}$$

$$v = b\,\mathrm{sech}^2(\gamma_2 X)\,, \quad \tfrac{b}{3} = 4(\delta+\lambda)\gamma_2^2\,. \tag{6.51}$$

Then, the nonlinear wave packet initial condition is based on either a maximum point in the group velocity curve where $\partial c_g/\partial k = 0$ and $k = k_m$, or a maximum point in the phase velocity curve where $c_p = c_g$ and $k = k_s$. The former corresponds to the unsteady nonlinear wave packet travelling at a speed close to the maximum group velocity, and is relevant for both modes in Case A, but only for mode 1 in Cases B and C. The latter corresponds to a steady wave packet and is relevant for mode 2 in Cases B and C, and both modes in Case D.

To obtain a suitable wave packet initial condition, the procedure is to choose k, either k_m or k_s, and then find the ratio $r = u_0/v_0$ from (6.32) or (6.33) in the form $u_0 = U_0 a_0\,, v_0 = V_0 a_0$ where a_0 is an arbitrary function of X, but $U_0\,, V_0$ are known functions of k. Based on the expected outcome that the nonlinear wave packet will be governed by an evolution equation such as the nonlinear Schrödinger equation, we choose $a_0(X) = A_0\,\mathrm{sech}(K_0 X)$. Note that the underlying theory suggests that the shape should be sech, and that K_0 depends on the amplitude A_0 (e.g., Grimshaw and Helfrich [1]). Here instead we choose a value of $K_0 << k$. Then the wave packet initial condition is

$$u(X,0) = rV_0A_0\,\mathrm{sech}(K_0X)\cos(kX)\,, \tag{6.52}$$

$$v(X,0) = V_0A_0\,\mathrm{sech}(K_0X)\cos(kX)\,, \tag{6.53}$$

where $r = U_0/V_0$ is a known function of k, and we can choose V_0 arbitrarily.

Our main aim is to understand and interpret the observed dynamical behaviour by relating it to the main features of the relevant dispersion curves, comparing especially the theoretically predicted group speeds and $r = u_0/v_0$ amplitude ratios with those found in the numerical simulations. For the latter, we adopt the following methodology; the speed is measured at the maximum of the dominant wave packet, and the numerical ratio is measured as $R = \max|u|/\max|v|$ in the interval between the two nearest peaks, containing the maximum value of the dominant wave packet. Note that R is necessarily positive, unlike r, since phase determination numerically is quite difficult. In some cases wave packets generated in the numerical simulations are either contaminated by radiation, or show signs of more

than one carrier wavelength. In these cases the ratio is not so instructive, and instead we choose the relevant points on the dispersion curves primarily by the speed of the wave packet, ruling out some points if the corresponding wavelength is too long or too short.

6.4.1 Case A: $\beta > 0, \mu > 0$

A typical numerical result is shown in Figures 6.7 and 6.8 using the KdV solitary wave initial condition (6.50). The generation of two wave packets can be seen in the u-component, but one of them is too small to be seen in the v-component. The comparison of the numerical modal ratio R, determined as described above, shows very good agreement with the theoretical prediction from the dispersion relation, see Table 6.1. The theoretical modal ratio is $r = 3.692$ for mode 1 and $r = -0.132$ for mode 2, while the speeds are $c_{g1} = -2.912, c_{g2} = -3.854$ and $k_{m1} = 0.895, k_{m2} = 0.584$. The ratios of the numerically found wave packets obtained from the vertical blue dashed lines A and B in Figure 6.8 are given, respectively by $R = 3.433$ for mode 1 and $R = 0.176$ for mode 2, which are in agreement with the theoretical predictions, and the numerically found speeds $-2.960, -3.933$ are also in good agreement. However, it can be seen that there is also some significant radiation to the left of these wave packets, and in particular some focussing possibly associated with the point G_1 in Figure 6.2. This is a resonance between the group velocity of mode 1 and the phase velocity of mode 2. The numerical speed and ratio at this point are given by, respectively, -4.937 and 0.639 in reasonable agreement with the theoretical prediction. However, this resonance is perhaps contaminated here because the resonance points C, D, E, F on the dispersion curves near $G_{1,2}$ are quite close for a wide range of wavenumber k.

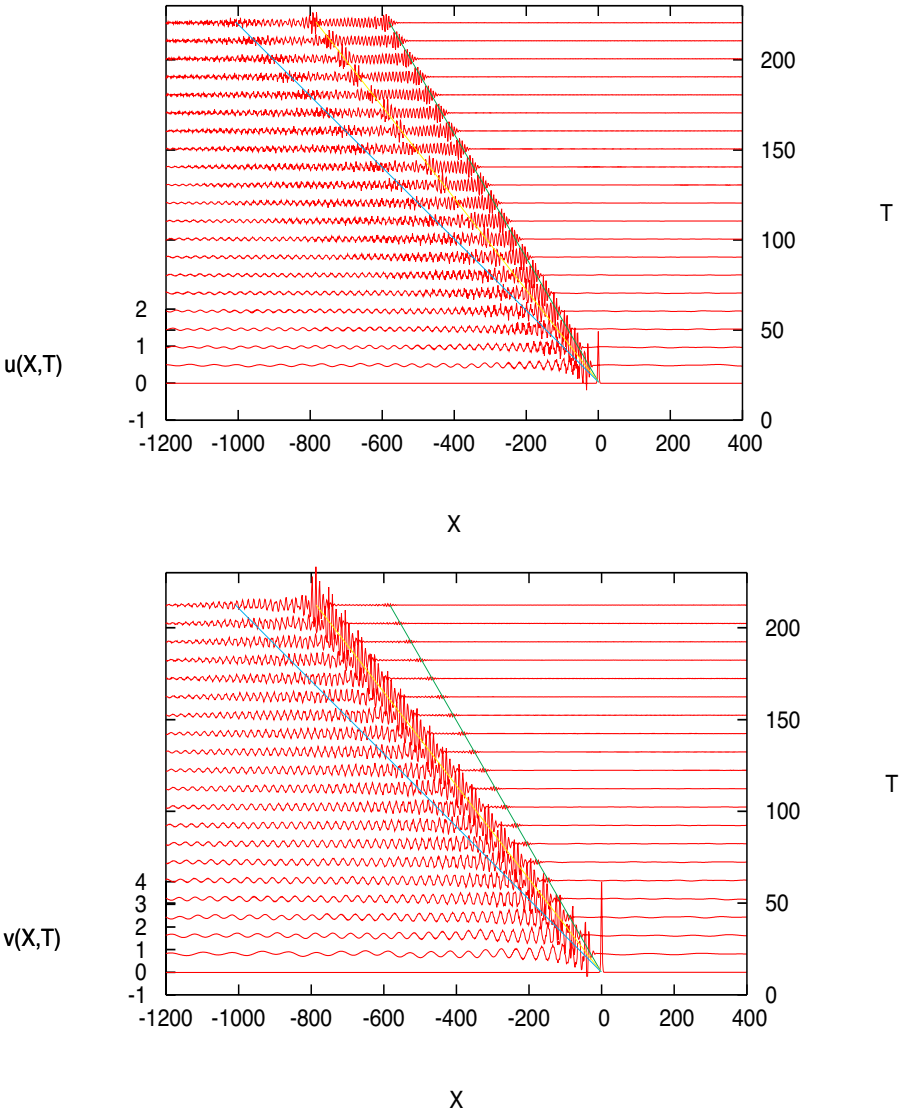

FIGURE 6.7: Numerical simulations for Case A using a KdV initial condition of weak coupling with $a = 1.4$ and $b = 4.38$ in (6.50). The green, yellow and blue lines in both plots refer to the points A, B and G_1 in Figure 6.2.

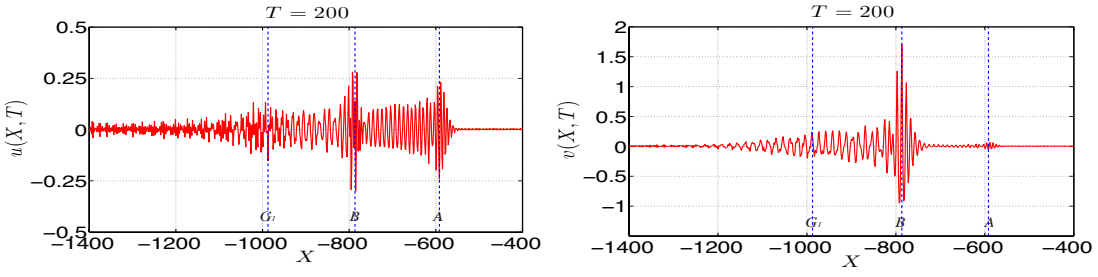

FIGURE 6.8: Same as Figure 6.7, but a cross-section at $T = 200$.

Next Figure 6.9 shows the numerical results initiated using the wave packet initial conditions (6.52) with $k = k_{m1} = 0.895$ and ratio $r = 3.692$ for mode 1, while setting $A_0 = 0.1$. These parameters correspond to mode 1, see point A in Figure 6.2. In qualitative agreement with the analogous results for a single Ostrovsky equation, we can see the emergence of a nonlinear wave packet propagating to the left with speed -2.940 and ratio 3.685, which are both close to the theoretical prediction for point A, see Table 6.1. Here we can also detect a mode 2 wave packet, corresponding to point B in Figure 6.2, as well as some radiation due to modal energy exchange associated with the resonance point G_1. The numerically found speeds are, respectively, -4.805 for point B and -5.996 for point G_1, with ratios $R = 0.411$ and $R = 1.162$. In this simulation, there is no evidence of waves associated with the points C, D, E, F.

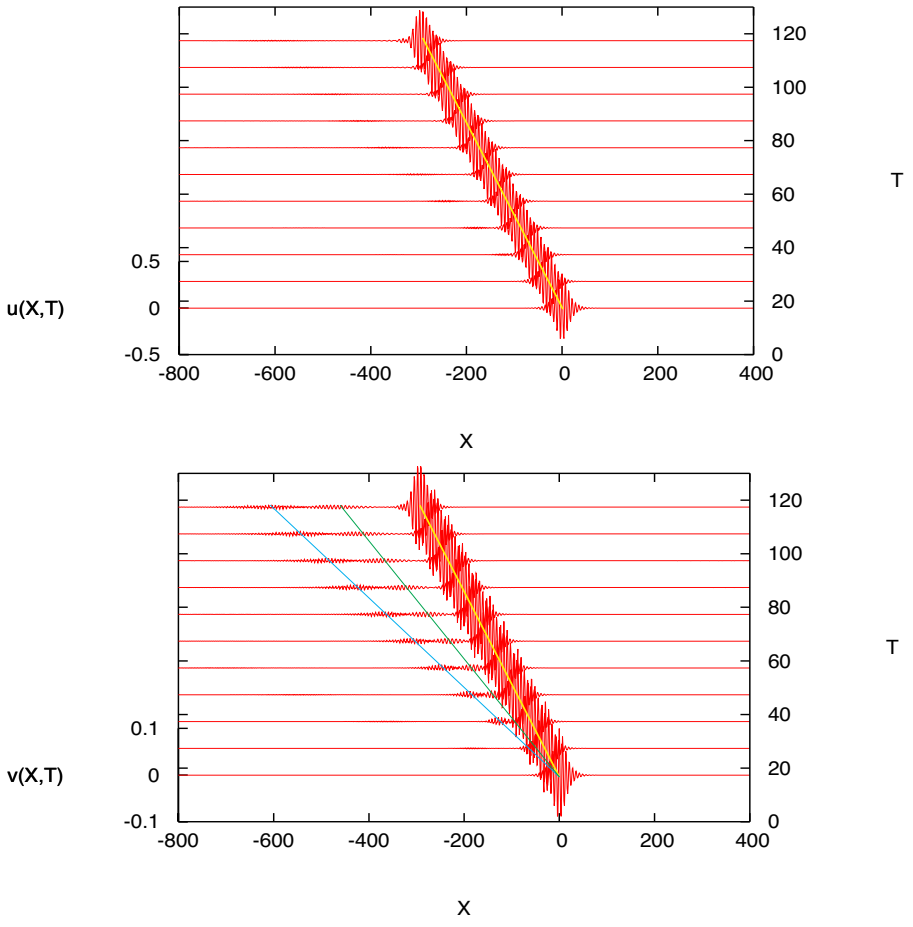

FIGURE 6.9: Numerical simulations for Case A using the wave packet initial condition (6.52) with $k = k_{m1} = 0.895$ for mode 1, and $A_0 = 0.1, K_0 = 0.1\,k$. The yellow, green and blue lines refer to the points A, B and G_1 in Figure 6.2.

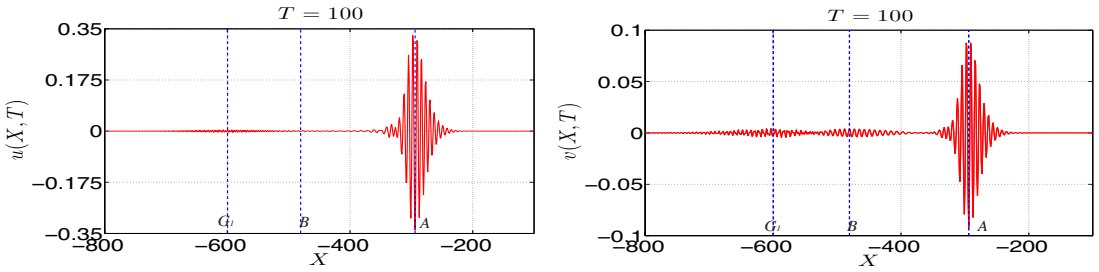

FIGURE 6.10: Same as Figure 6.9, but a cross-section at $T = 100$.

Figures 6.11, 6.12 and 6.13 show the numerical results which commenced with wave packet initial conditions (6.52) with $k = k_{m2} = 0.584$ and ratio $r = -0.132$ for mode 2. These parameters correspond to point B in Figure 6.2. Again, we can clearly see one wave packet emerging and propagating with a speed -3.904 and ratio 0.177, both close to the theoretical prediction for point B, see Table 6.1. But here there is also a small unsteady wave packet, seen in the u-component, moving with the speed -3.281 close to the theoretical prediction of $c_{g1} = -2.912$ and ratio $R = 2.555$ for a mode 1 wave packet, corresponding to point A in Figure 6.2 and Table 6.1. Here we can also see the formation of wave packets to the left, corresponding to points G_1 and C, E with the numerically found speeds $-6.050, -8.262$ and ratios $1.436, 0.567$ also in reasonable agreement with the theoretical prediction.

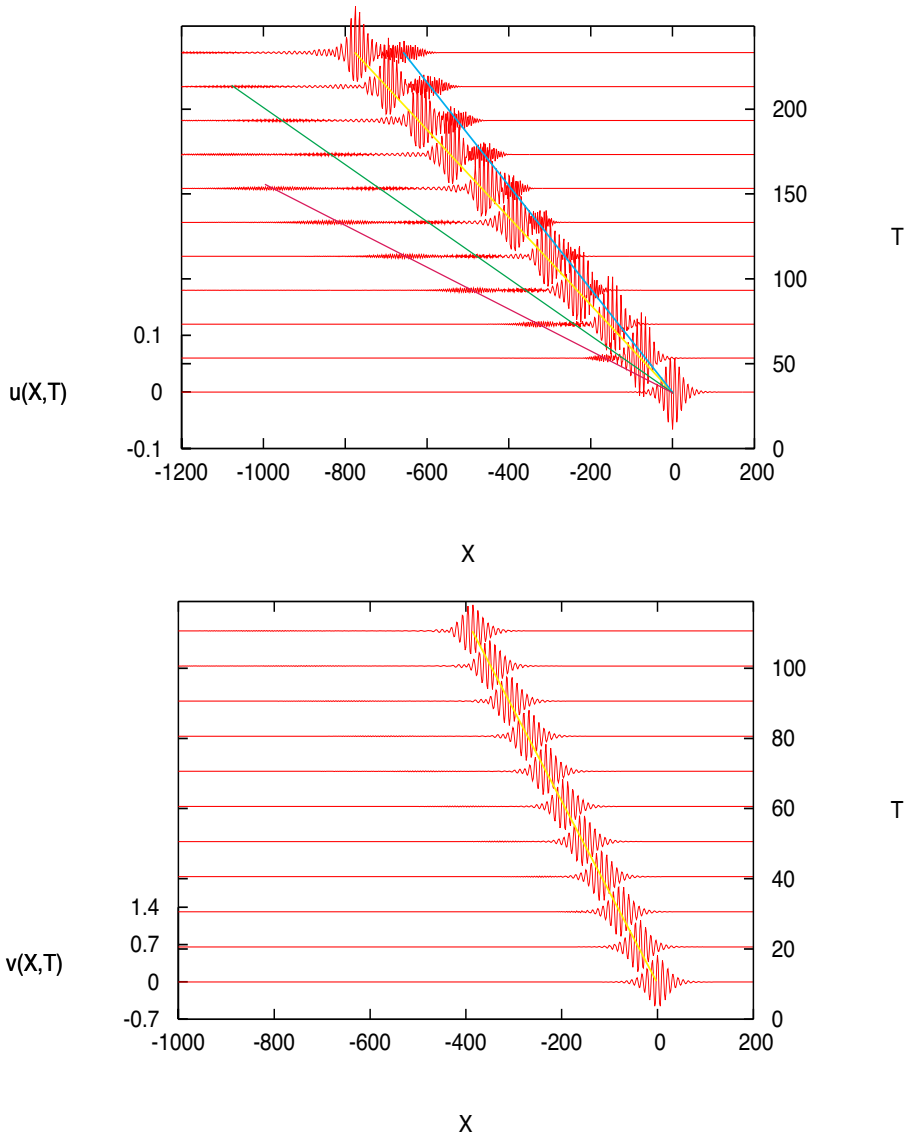

FIGURE 6.11: Numerical simulations for Case A using the wave packet initial condition (6.52) with $k = k_{m2} = 0.584$ for mode 2, and $A_0 = 0.5, K_0 = 0.1\,k, V_0 = 1$. The blue, yellow, green and magenta lines refer to the points A, B, G_1 and (C, E) in Figure 6.2. Note that the scales for the u and v components are different.

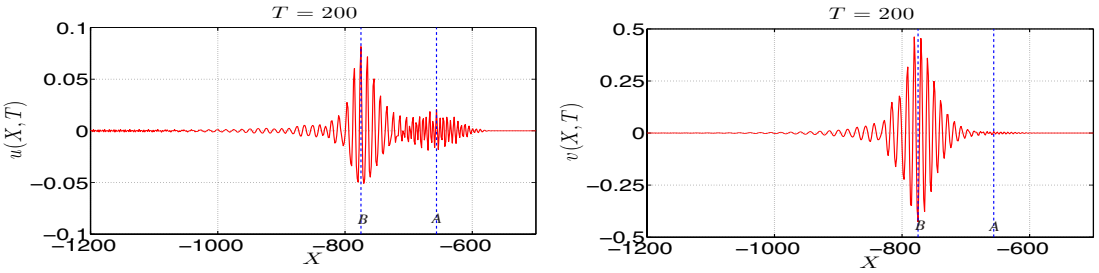

FIGURE 6.12: Same as Figure 6.11, but a cross-section at $T = 200$.

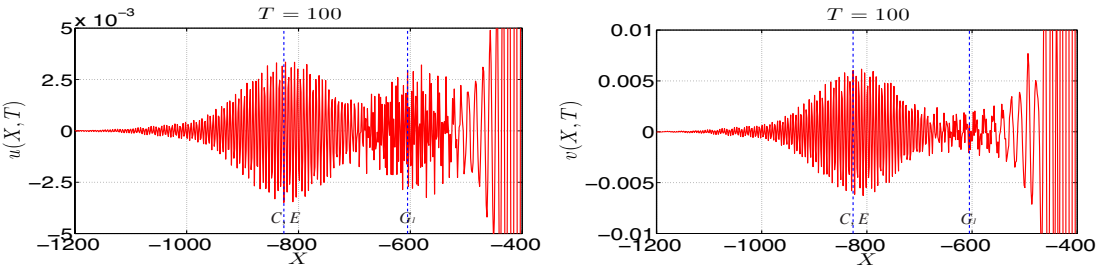

FIGURE 6.13: Same as Figure 6.11, but a cross-section at $T = 100$ of the domain $-1200 < X < -400$ and with rescaled u and v.

6.4.2 Case B: $\beta > 0, \mu < 0$

A typical numerical result is shown in Figures 6.14, 6.15 using the KdV solitary wave initial condition (6.50). We can clearly see a wave packet in the u-component identified by the vertical blue dashed line A, with speed -0.710 and ratio 4.815. The corresponding theoretical predictions are a speed $c_{g1} = -0.6834$ and ratio $r = 33.696$, corresponding to point A in Figure 6.3, see Table 6.2. However, here the wave packet is strongly nonlinear, and it is noted that if v is measured at the point where $|u|$ is at maximum, then the numerical ratio is 25, closer to the theoretical value. Another wave packet can be clearly seen in v-component with speed -1.743 and ratio -0.221. Here the corresponding theoretical predictions are a speed -1.785 and ratio $r = -0.036$, corresponding to point B in Figure 6.3, see Table 6.2. Again, this wave packet is strongly nonlinear, and if u is measured at the point where $|v|$ is at maximum, then the numerical ratio is -0.023, closer to the theoretical value. It is also noted that there is considerable radiation in the plot, so that it is not possible to see the wave packet associated to point A in the v-plot, and similarly for the point B in the u-plot.

In Figures 6.16 and 6.17 we use the wave packet initial condition (6.52), with $k = k_{m1} = 0.345$ and the ratio $R = 33.696$ corresponding to a maximum group velocity $c_{g1} = -0.683$ in mode 1 corresponding to point A in Figure 6.3, see Table 6.2. As expected, an unsteady wave packet emerges, clearly seen in both the u and v plots in the first yellow line, propagating with speed -0.610 and ratio 21.261 in reasonable agreement with the theoretical predictions. The blue line

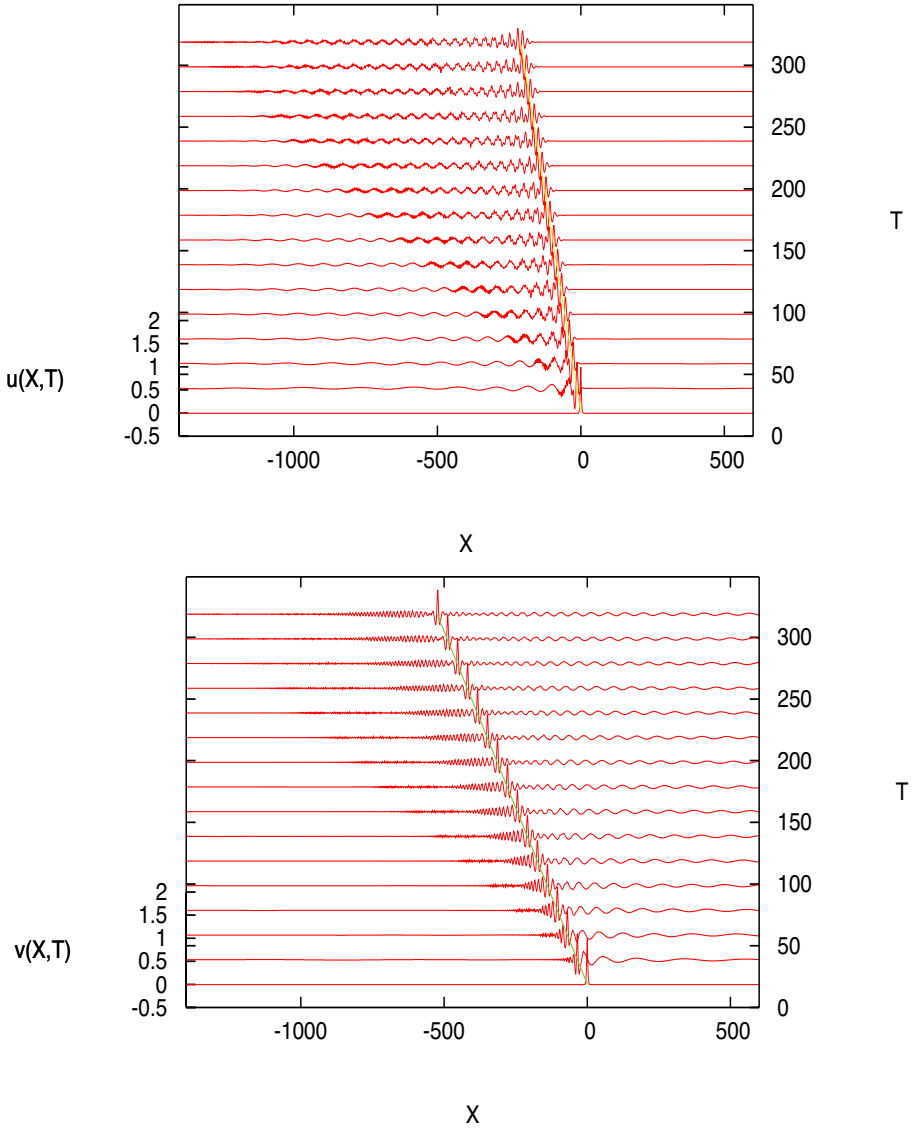

FIGURE 6.14: Numerical simulations for Case B using a KdV initial condition of weak coupling with the parameter $a = b = 1$.

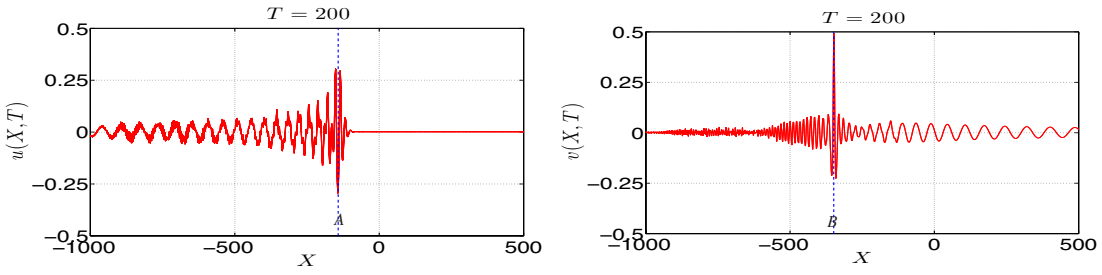

FIGURE 6.15: Same as Figure 6.14, but a cross-section at $T = 200$ for both modes.

in the v-plot shows a wave packet propagating with speed -1.343, but the ratio cannot be measured here as in the u-plot, this location is the tail of the larger wave packet associated with point A. Based on the speed and wavenumber, it is suggested that this is associated with point B in Figure 6.3, see Table 6.2. A third small wave packet can be observed in the v -mode represented by the green line with speed -2.446 and ratio 3.160, which is associated with the resonance point C for mode 1 in Figure 6.3, see Table 6.2, generated by a mode 1 unsteady wave packet associated with the point A. Then, a fourth small wave packet can also be observed in the v-mode represented by the magenta line with speed -3.057 and ratio 0.148, which is associated with the point E, based on ratio and wavenumber considerations. Both these third and fourth wave packets have speeds which might be associated with the point D_1, but this connection has been ruled out due to a large disparity between the predicted and observed ratio and wavenumber.

Figures 6.18 and 6.19 show the case when the wave packet initial condition (6.52) has $k = k_{s2} = 0.372$ with ratio $R = -0.036$ corresponding to a maximum phase speed in mode 2, represented by the point B in Figure 6.3, see Table 6.2. In both modes, the main feature is a steady wave packet with speed -1.787 and ratio 0.042, see the yellow line, in good agreement with the predicted values from the dispersion relation, see Table 6.2. There is a very small wave packet indicated by the green line with a speed -0.461 which is associated with point A based on the speed. Here the ratio cannot be measured as this location lies the tail of the larger wave packet associated with point B. There is a third wave packet shown by the blue line with speed -3.362 and ratio 0.144, which is associated with the point E, based on the consideration of the speed and wavenumber, as the ratio cannot be measured accurately since in the v-plot this location lies in the tail of the main wave packet. Wave packets have speeds which might be associated with the point D_1, but this connection has been ruled out due to a large disparity between the predicted and observed ratio and wavenumber.

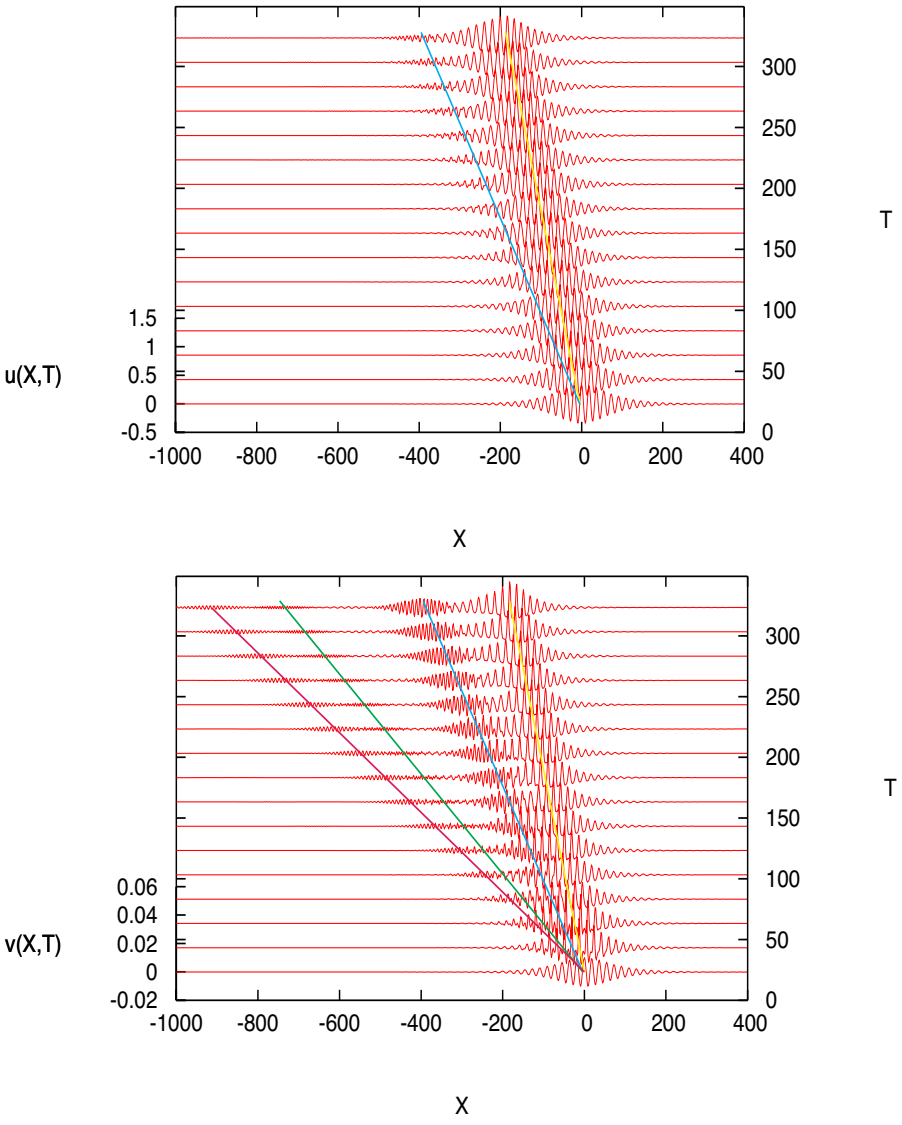

FIGURE 6.16: Numerical simulations for Case B using a nonlinear wave packet initial condition corresponding to the value $k = k_{m1} = 0.345$ with $A_0 = 0.01\,, K_0 = 0.05\,k$ and $V_0 = 1$. The yellow, blue, green and magenta lines respectively refer to points A, (B, C), (C, D_1) and (D_1, E) in the dispersion relation.

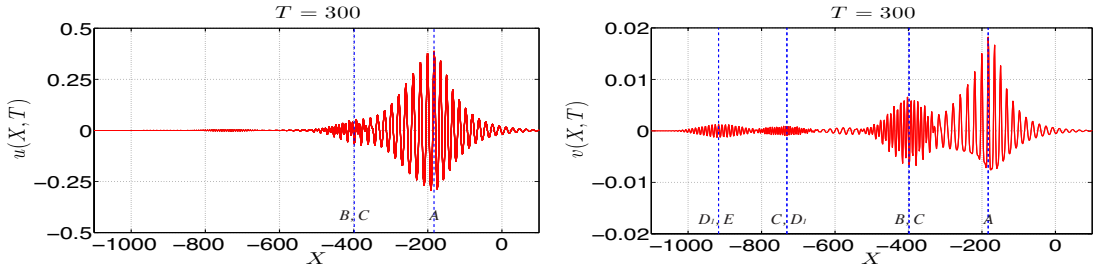

FIGURE 6.17: Same as Figure 6.16, but a cross-section at $T = 300$ for both modes.

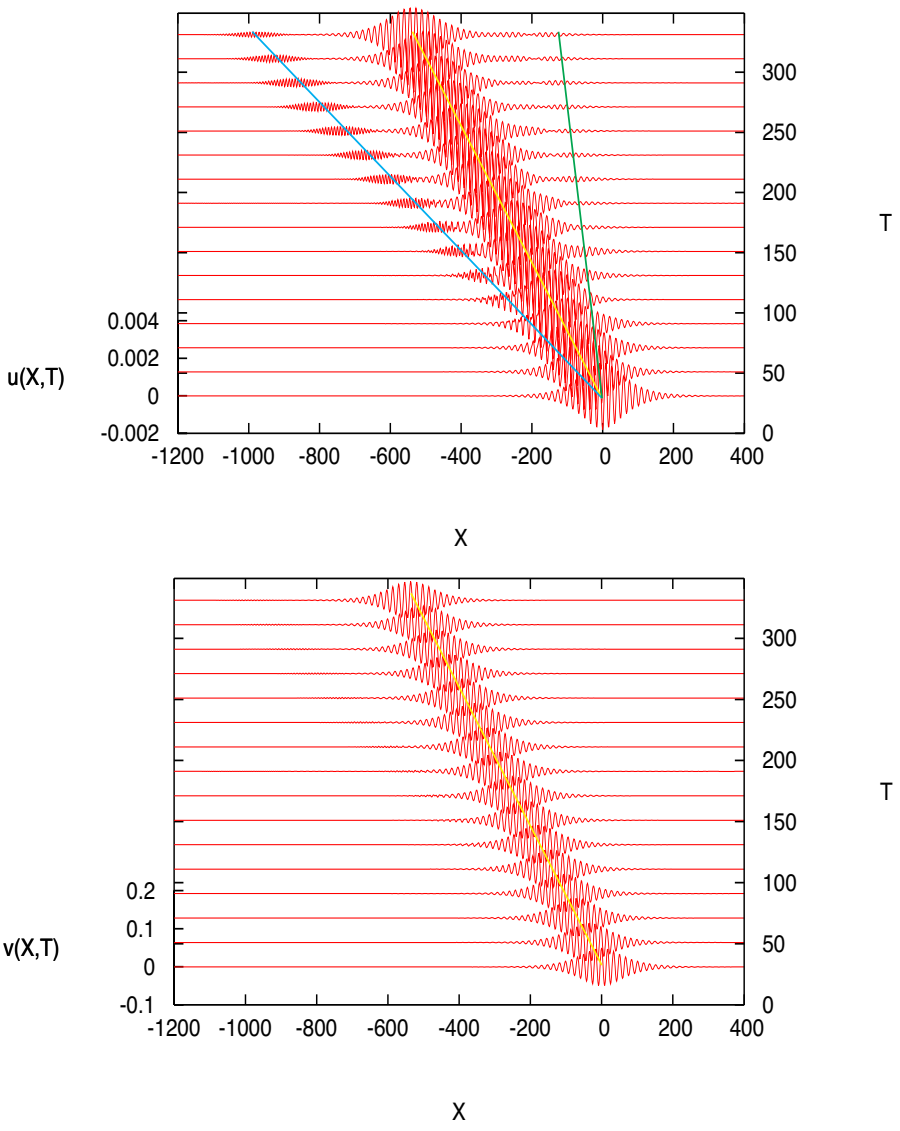

FIGURE 6.18: Numerical simulations for Case B using a nonlinear wave packet initial condition corresponding to the value $k = k_{s2} = 0.372$ with $A_0 = 0.05, K_0 = 0.05\,k, V_0 = 1$. The green, yellow and blue lines respectively refer to points A, B and (D_1, E) in the dispersion relation.

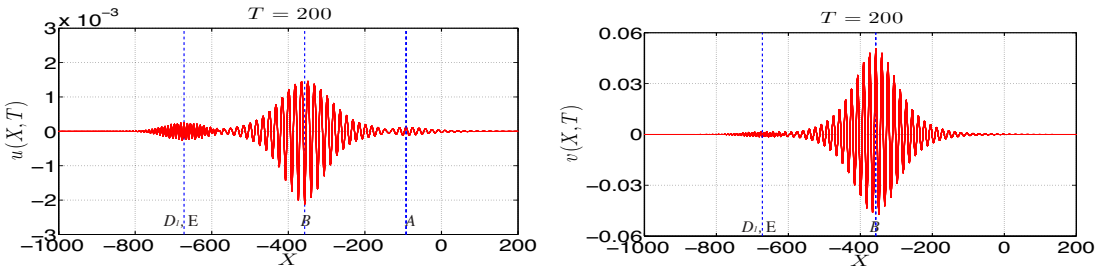

FIGURE 6.19: Same as Figure 6.18, but a cross-section at $T = 200$ for both modes.

6.4.3 Case C: $\beta < 0, \mu > 0$

Case C is analogous to the Case B. A typical numerical result is shown in Figures 6.20 and 6.21 using the KdV solitary wave initial condition (6.50). But here we chose $\gamma_1 \neq \gamma_2$ in order that the ratio a/b should coincide with the predicted ratio 1.3 corresponding to the point A in Figure 6.5. A strongly nonlinear unsteady wave packet emerges, denoted by the vertical line A in Figure 6.21, with speed -0.156 and ratio 0.5496, in agreement with the theoretical predictions from the point A in the dispersion plots of Figure 6.5 and Table 6.4. This wave packet has a phase speed which is very close to the group velocity over the range of wave numbers from the point D to E, leading to strongly nonlinear effects and difficulty in numerically determining a ratio.

In Figures 6.20 and 6.21 there is also evidence of significant radiation both to the right and to the left of the main wave packet. The waves to the right with positive speed can be associated with the points F_2 and/or N as these have a positive group velocity for mode 2 and a ratio of nearly -10, which means that the amplitude in the v-plot is too small to be seen. Although the points F and N are very close, they have a different interpretation. The point F_2 is a resonance between c_{g1} and c_{p2}, while the point N is a resonance between the speed at the minimum point of c_{g1} with c_{p2}. Moreover, this wave to the right has the appearance of a linear dispersive wave, and hence there is no very clear identifiable speed or wavenumber. The waves to the left show both small-scale and large scale features in both u and v, with the small-scale features more prominent in u and the large-scale features more prominent in v. The large-scale feature may be associated with either B or K and the small-scale with either J or M. That is, these are mode 1 waves associated with turning points in the group velocity, and a resonance with the phase velocity. Also note that for both B and K, the ratio is such that v dominates, while for J and M it is u that dominates, features consistent with the numerical simulation. Thus, overall all the features in the numerical simulation can be associated with the turning points in the group velocity curve c_{g1} for mode 1.

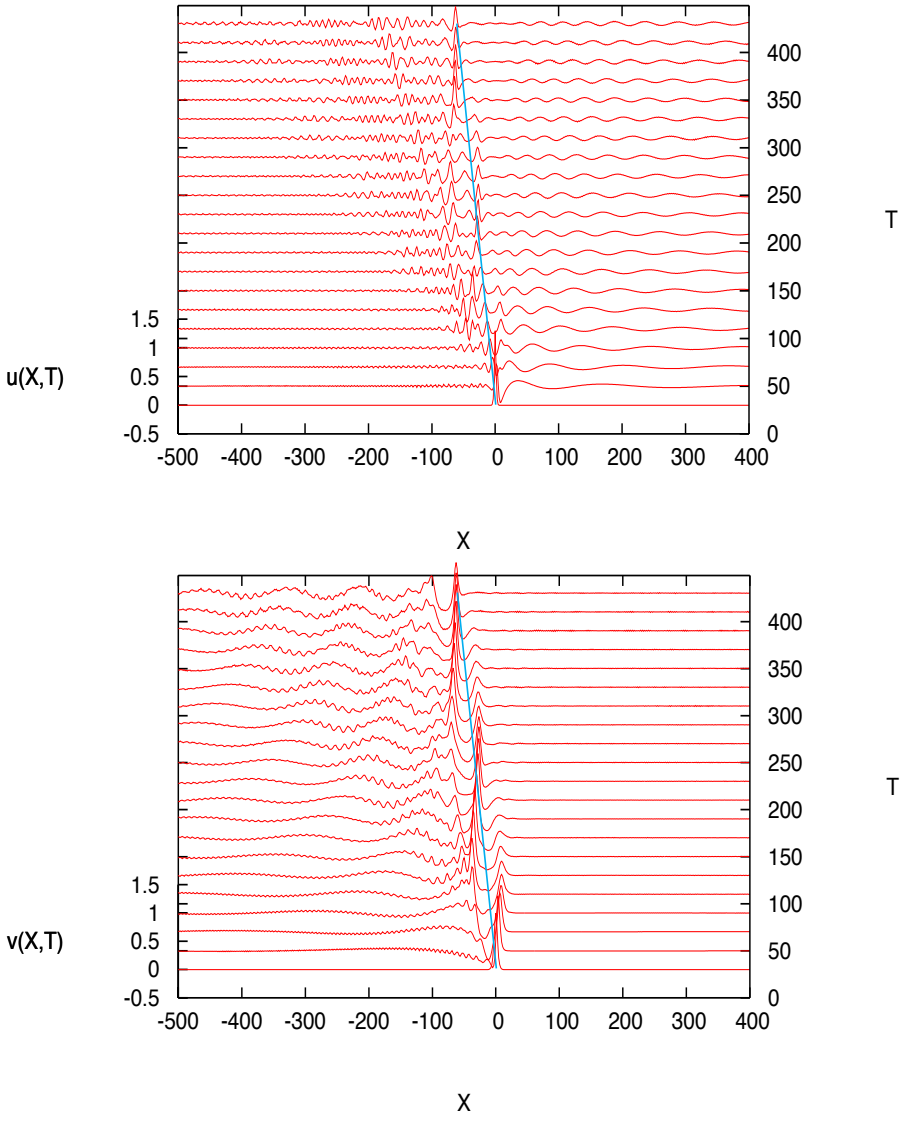

FIGURE 6.20: Numerical simulations for Case C using a KdV initial condition of weak coupling (6.50) with $a = 1.3$ and $b = 1$.

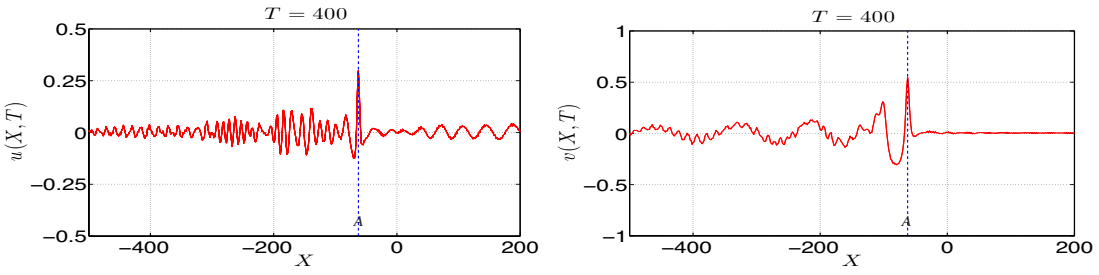

FIGURE 6.21: Same as Figure 6.20, but a cross-section at $T = 400$ for both modes.

As noted above, the group velocity curve c_{g1} for mode 1 has three turning points, while there are no such turning points for c_{g2}. To examine each of these, the turning point A was examined in Figure 6.5 and Table 6.4, whilst using the wave packet initial condition (6.52) with wavenumber $k = k_{m1} = 0.306$ and ratio $R = 1.309$. The numerical results are shown in Figures 6.22, 6.23 and the emergence of a nonlinear wave packet is clearly seen. At the vertical line A, the speed is -0.146 with ratio 1.387, in agreement with the theoretical prediction. There is a secondary wave packet now discernible on the vertical line I, moving with speed -0.625 and ratio 1.910, which from the dispersion relation in Figure 6.5 is identified with the point I, which is a resonance between the maximum value of the phase speed of mode 2 (point C) with mode 1. However, it is noted that the resonance points J, M are close by with similar values, and so may also be relevant.

Next was used the wave packet initial condition associated with the turning point B in Figure 6.5, with $k = 0.152$ and $A_0 = 0.25, K_0 = 0.2k, V_0 = 1$. The numerical result is shown in Figures 6.24 and 6.25. A nonlinear wave packet emerges with speed -0.156 and ratio 0.380. However, these values are not consistent with the theoretical predictions for point B in Table 6.4. Instead the outcome for the speed would seem to be more consistent with the points A or D_2, but the ratios are not in agreement. Examination of the v-plot suggests that possibly packets associated with both these points are generated, and the consequent interaction between them makes determination of a consistent ratio quite difficult.

The corresponding numerical results for an initial condition associated with the turning point K are shown in Figures 6.26 and 6.27. A strongly nonlinear wave packet emerges, with speed -0.303 and ratio 0.492, as can be seen in both the u and v plots, and is in reasonable agreement with the theoretical prediction. However, the resonance points D_1, F_1 have similar speeds and the strong nonlinearity suggests there may be some interaction here, leading to difficulty in determining a numeral ratio. There is also a small wave propagating to the right, seen in the u-plot, with the speed 0.234 and the ratio 4.939, indicated by the vertical line N, which can be associated with one or more of the resonance points N, F_2, G in Figure 6.5.

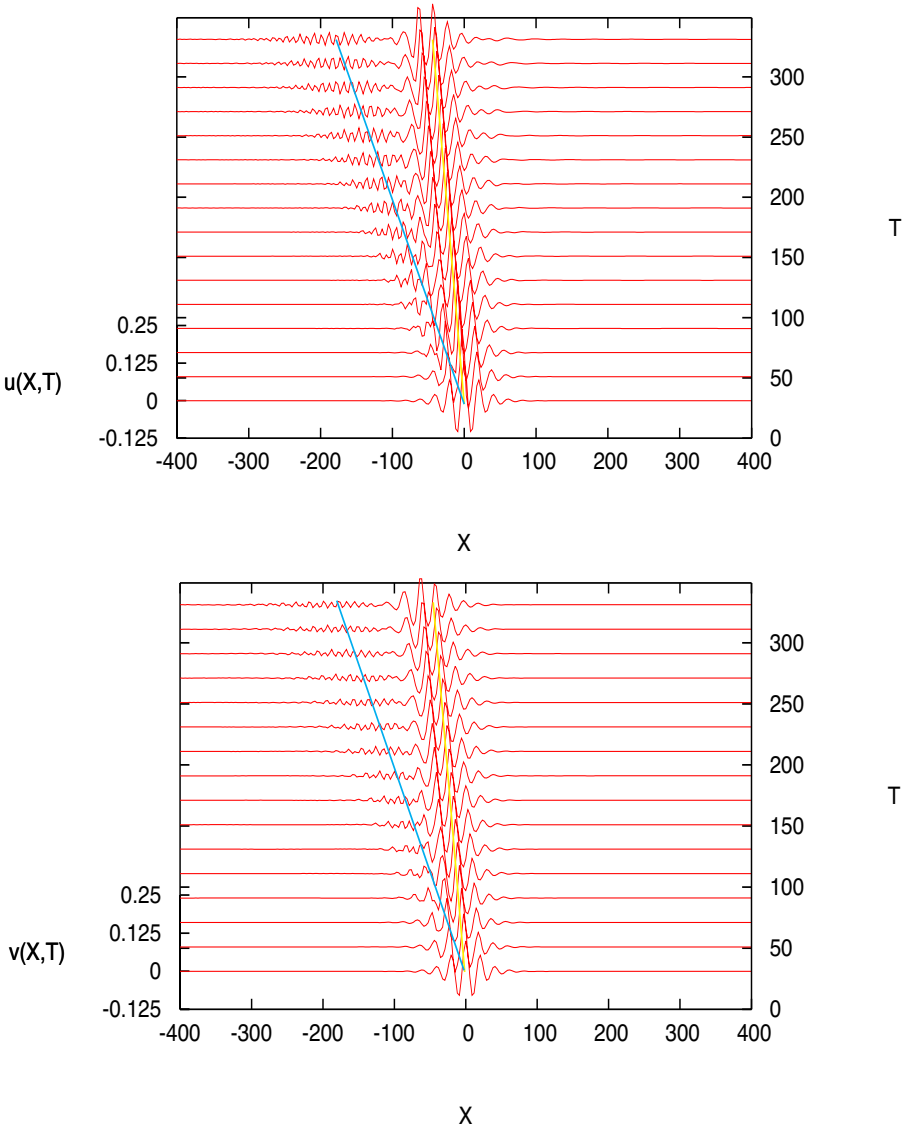

FIGURE 6.22: Numerical simulations for Case C using the wave packet initial condition (6.52) with $k = k_{m1} = 0.306$ corresponding to point A with $A_0 = 0.1, K_0 = 0.2\,k, V_0 = 1$. The yellow and blue lines respectively refer to points A and (I, J, M) indicated in Figure 6.23.

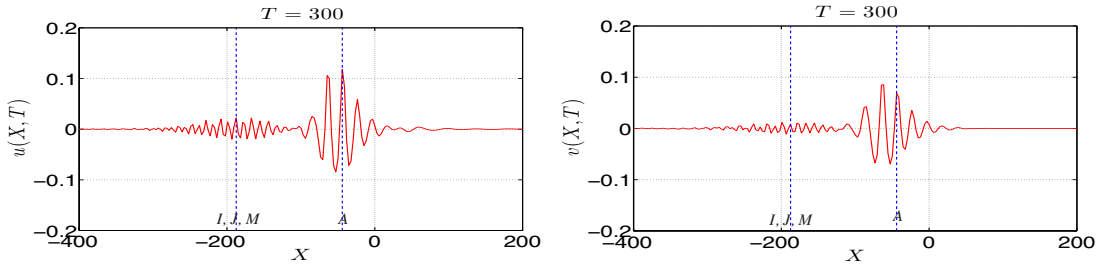

FIGURE 6.23: Same as Figure 6.22, but a cross-section at $T = 300$ for both modes.

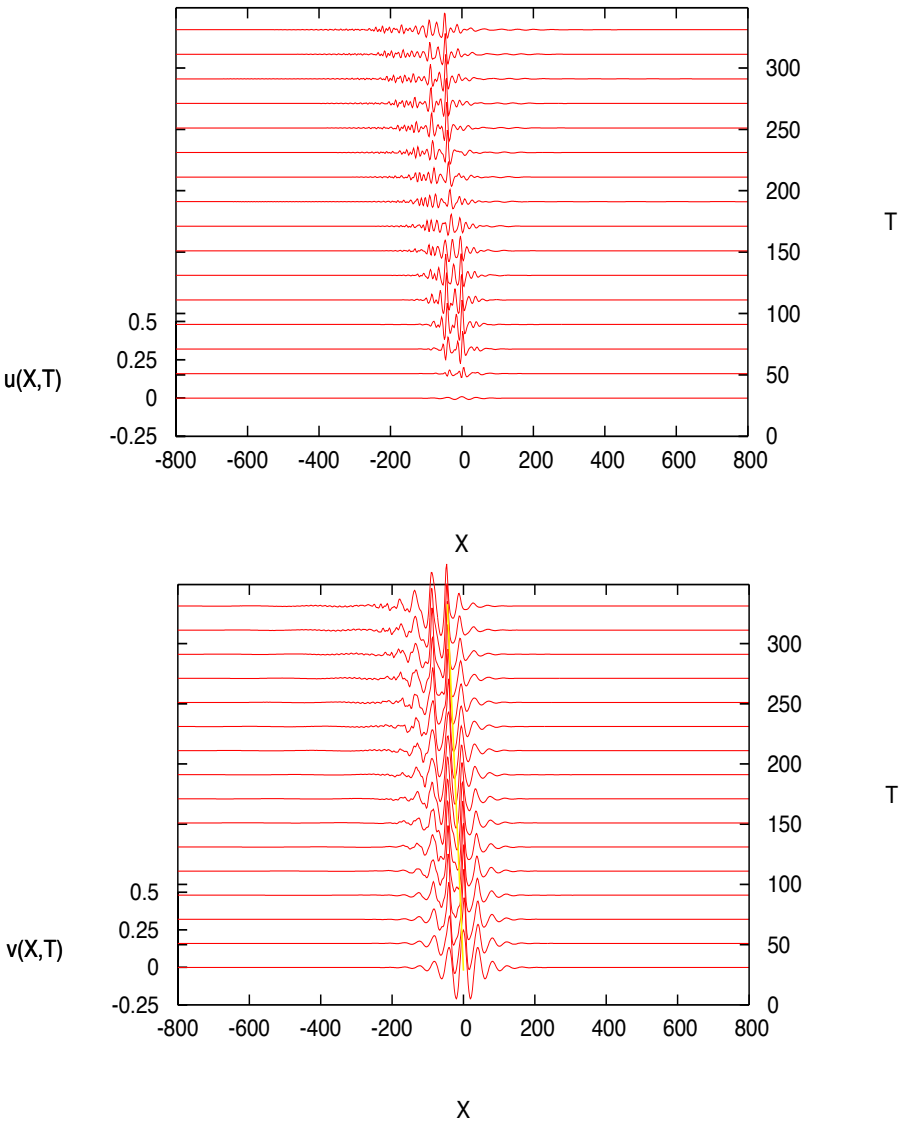

FIGURE 6.24: Numerical simulations for Case C using the wave packet initial condition (6.52) with $k = 0.152$ corresponding to point B with $A_0 = 0.25, K_0 = 0.2\,k, V_0 = 1$.

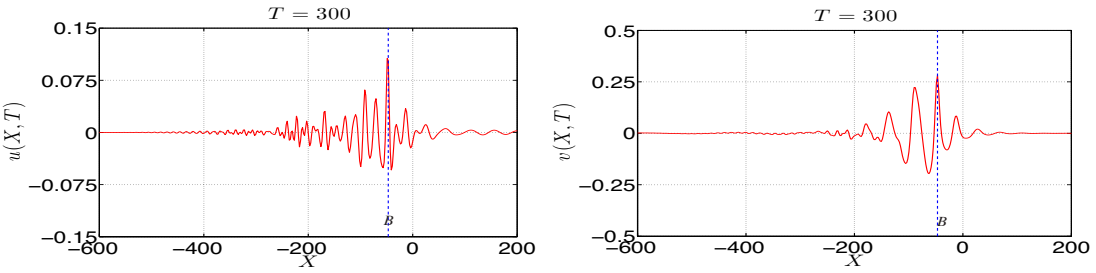

FIGURE 6.25: Same as Figure 6.24, but a cross-section at $T = 300$ for both modes.

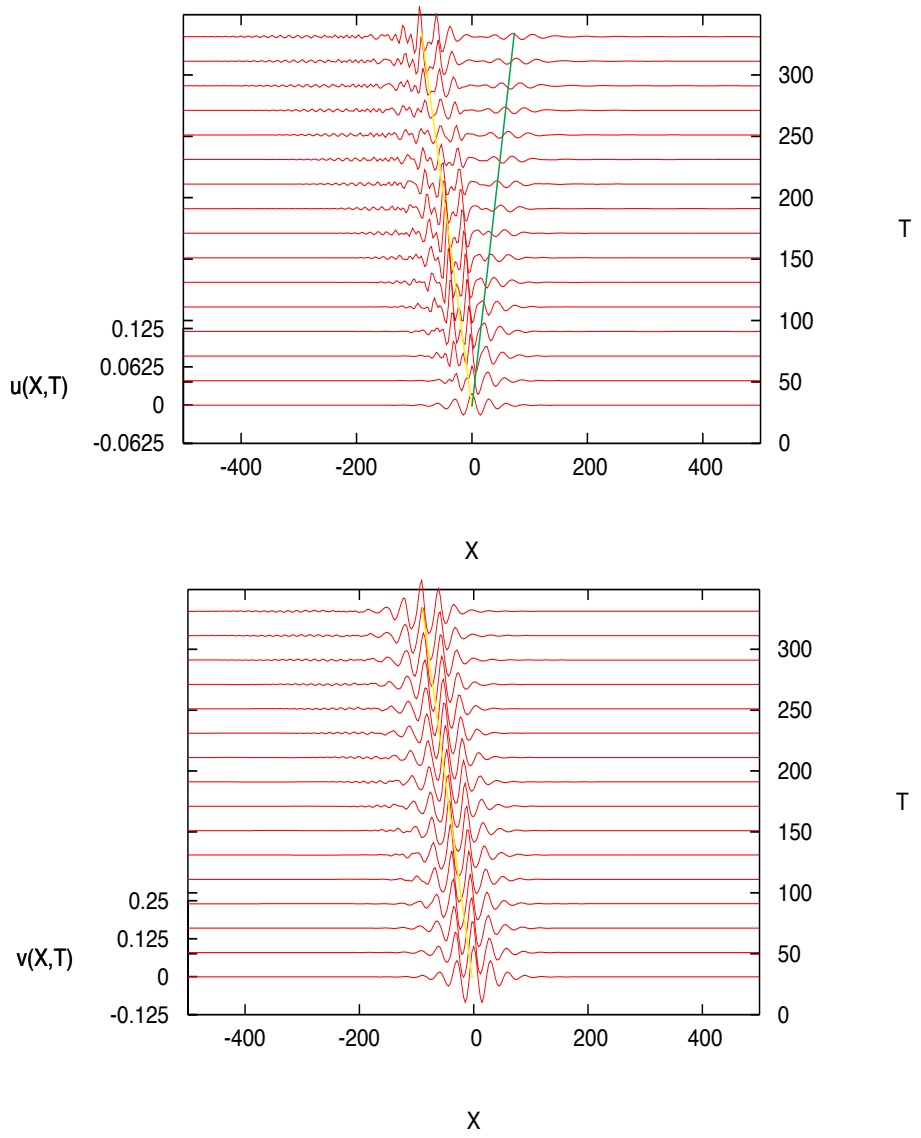

FIGURE 6.26: Numerical simulations for Case C using the wave packet initial condition (6.52) with $k = 0.209$ corresponding to point K with $A_0 = 0.1, K_0 = 0.2\,k, V_0 = 1$.

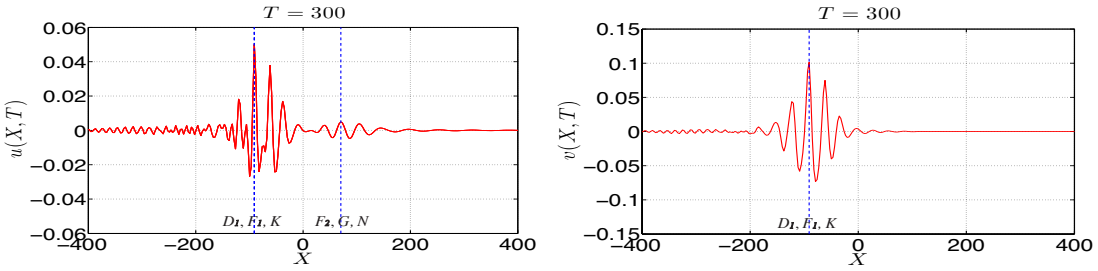

FIGURE 6.27: Same as Figure 6.26, but a cross-section at $T = 300$ for both modes.

Finally, the simulation associated with the turning point C in Figure 6.5 is examined, using the wave packet initial condition (6.52) with $A_0 = 0.025, K_0 = 0.05k, V_0 = 1$. The numerical result is shown in Figures 6.28 and 6.29. In this case a steady wave packet clearly emerges, indicated by the green vertical line, with speed -0.244 and ratio 1.874, in good agreement with the predicted theoretical values. Note that the resonance point E has a similar speed, but quite different wavenumber, and indeed the wave formation associated with this point is not seen.

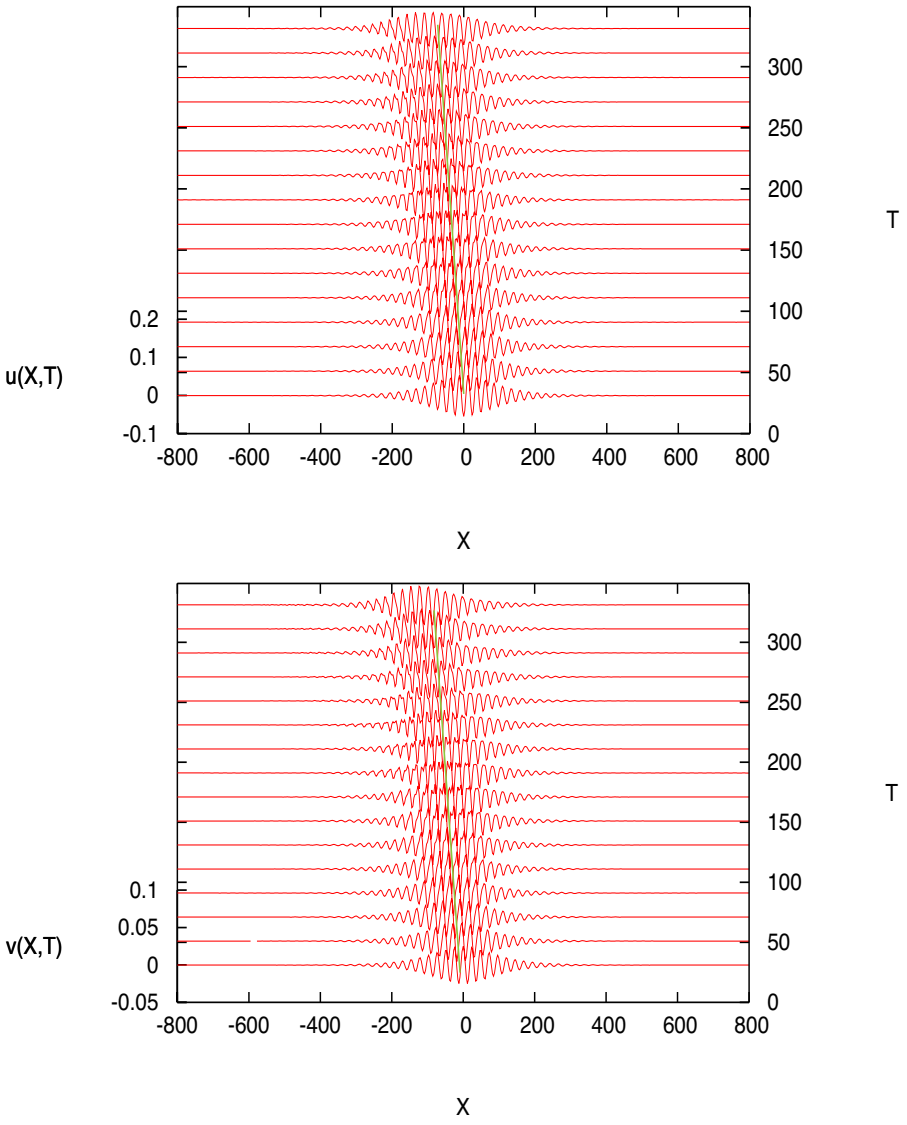

FIGURE 6.28: Numerical simulations for Case C using the wave packet initial condition (6.52) with $k = k_{s2} = 0.259$ corresponding to point C with $A_0 = 0.025, K_0 = 0.05\,k, V_0 = 1$.

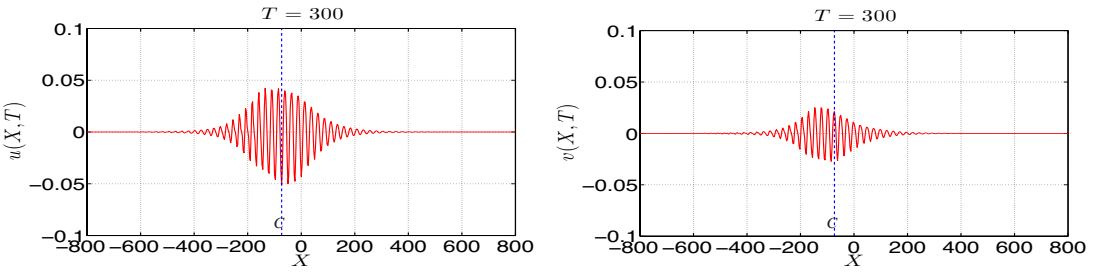

FIGURE 6.29: Same as Figure 6.28, but a cross-section at $T = 300$ for both modes.

6.4.4 Case D: $\beta < 0, \mu < 0$

A typical numerical result is shown in Figures 6.30 and 6.31 using the KdV solitary wave initial condition (6.50). The numerical results show two steady wave packets emerging, as expected, with speeds $-0.146, -0.586$ and ratios $10.136, 1.753$ associated with the vertical lines A and B respectively in Figure 6.31, in reasonable agreement with the theoretical values. These wave packets are strongly nonlinear and there is considerable evidence of resonances and radiation. In particular, the vertical line F in Figure 6.31 is interpreted as an interaction between the points B and F_1, the latter being a resonance between the group velocity of mode 1 and the phase speed of mode 2, see Figure 6.6 and Table 6.5. There is also a transient wave propagating to the right, probably due to fact that the negative signs of both β and μ allow both modes to have positive group velocities for low wavenumbers.

There are two different wavenumbers to consider when using the wave packet initial condition (6.52) corresponding to the points A and B in Figure 6.6. First, choose $k = k_{s1} = 0.3221$ and $R = 10.9729$ corresponding to the point A in Figure 6.6, see Table 6.5. The numerical results are shown in Figures 6.32, 6.33 and we see that the solution is dominated by a steady mode 1 wave packet, with speed -0.189 and ratio 7.934 in good agreement with the theoretical values. Another wave packet can be seen corresponding to the points B, F_2 in Figure 6.6, with speed -0.846 and ratio 3.056. Here there is some interaction between these two points. Further, there is a very small wave packet associated with the point F_2 in Figure 6.6, with speed -1.706 and ratio 0.368, in good agreement with the

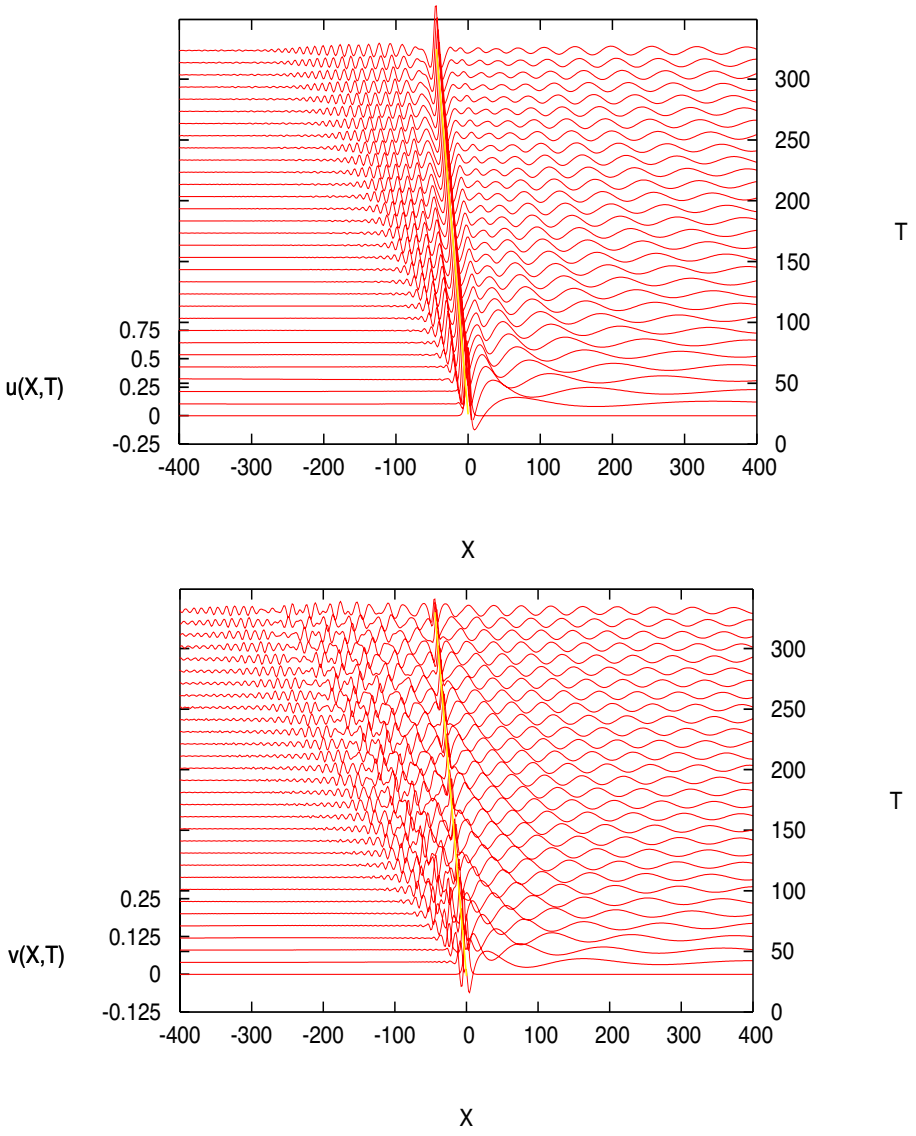

FIGURE 6.30: Numerical simulations for Case D using a KdV initial condition of weak coupling (6.50) with $a = 0.6$ and $b = 0.2$. The yellow line in both plots refers to point A.

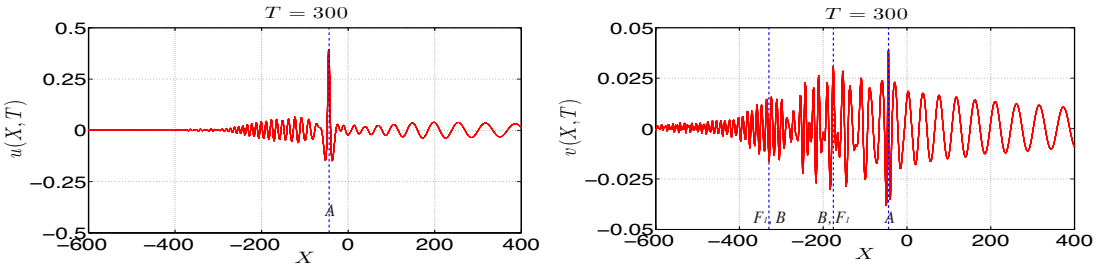

FIGURE 6.31: Same as Figure 6.30, but a cross-section at $T = 300$ for both modes.

theoretical values, although there may be some contamination here due to the point D, which has a similar speed.

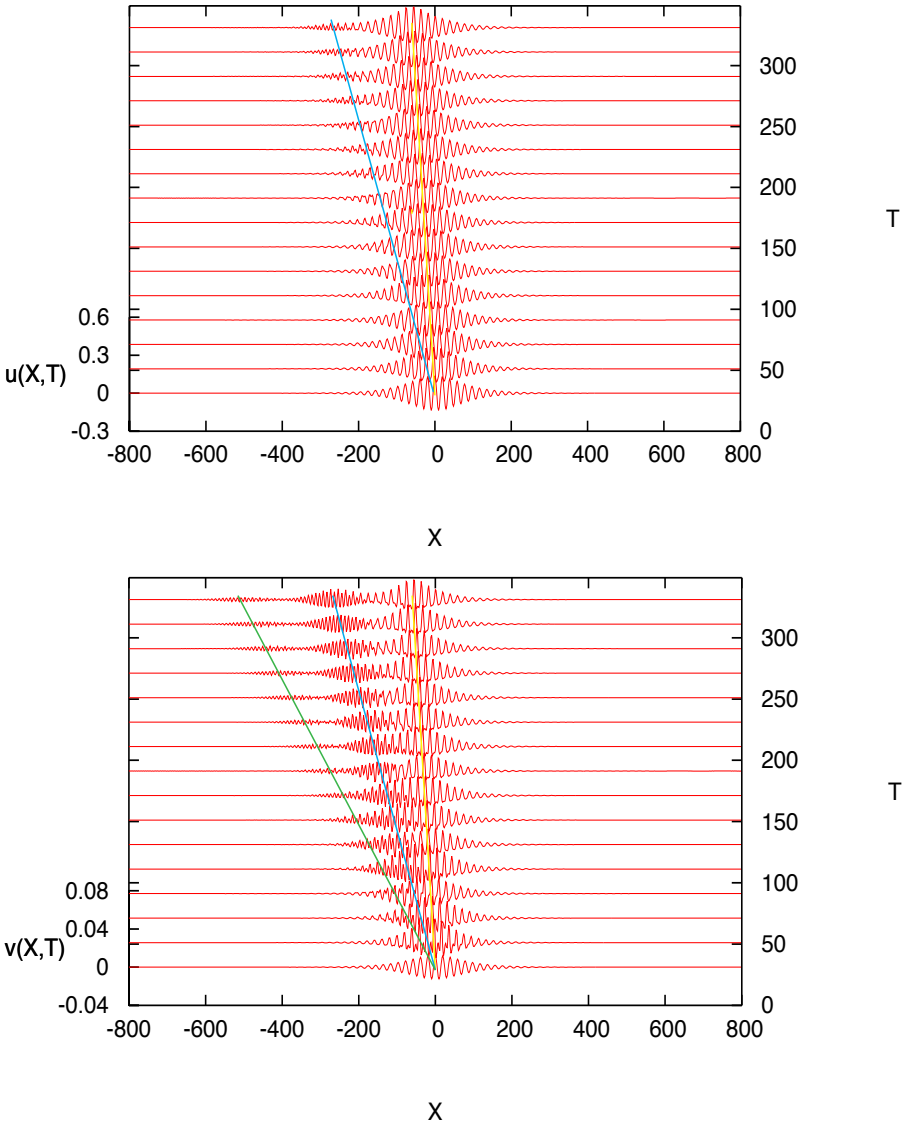

FIGURE 6.32: Numerical simulations for Case D using the wave packet initial condition (6.52) with $k = k_{m1} = 0.322$ corresponding to the point A in Figure 6.6, with $A_0 = 0.05, K_0 = 0.05\,k, V_0 = 0.25$. The yellow, blue and green lines respectively refer to points A, (B, F_1) and (F_2, D).

Secondly, use the wave packet initial condition (6.52) with $k = k_{s2} = 0.395$ and ratio, $R = -0.105$ corresponding to the point B in Figure 6.6, see Table 6.5. The numerical results are shown in Figures 6.34, 6.35 and the solution is now dominated by a steady mode 2 wave packet, as expected, with speed -0.820 and ratio -0.229, in good agreement with the theoretical values. There is also some

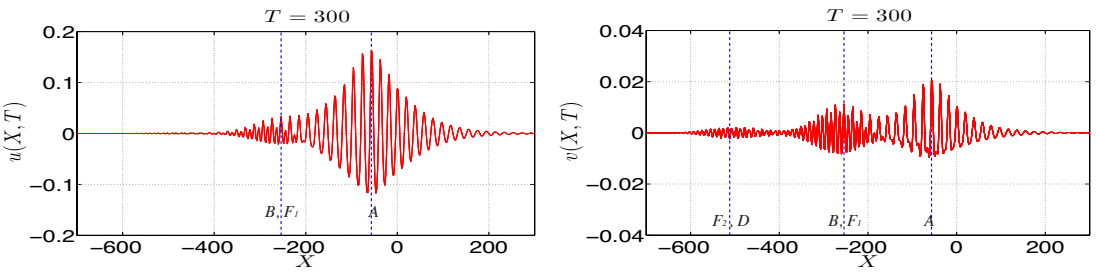

FIGURE 6.33: Same as Figure 6.32, but a cross-section at $T = 300$ for both modes.

interaction with the point F_1 here, seen in the u-plot where two wavenumbers can be seen. However, the dispersion curves in Figure 6.6 show that here there are potential resonances with mode 1 at $k = 0.1168$ and $k = 1.0657$, associated with the points C and D, see Table 6.5. There is no discernible evidence here of radiation into the wavenumber $k = 0.1168$ due to the large ratio of $O(200)$ needed, but a wave packet is seen with wavenumber $k = 1.0657$, indicated by the blue vertical line D in Figure 6.35, with the speed -2.014 and ratio 0.814, in reasonable agreement with the theoretical prediction, although there could also be some interaction with the point F_2 here, which has quite similar values. Another small wave packet can be seen, possibly corresponding to point G_1 in Figure 6.35 with the speed -2.578 and ratio 0.503.

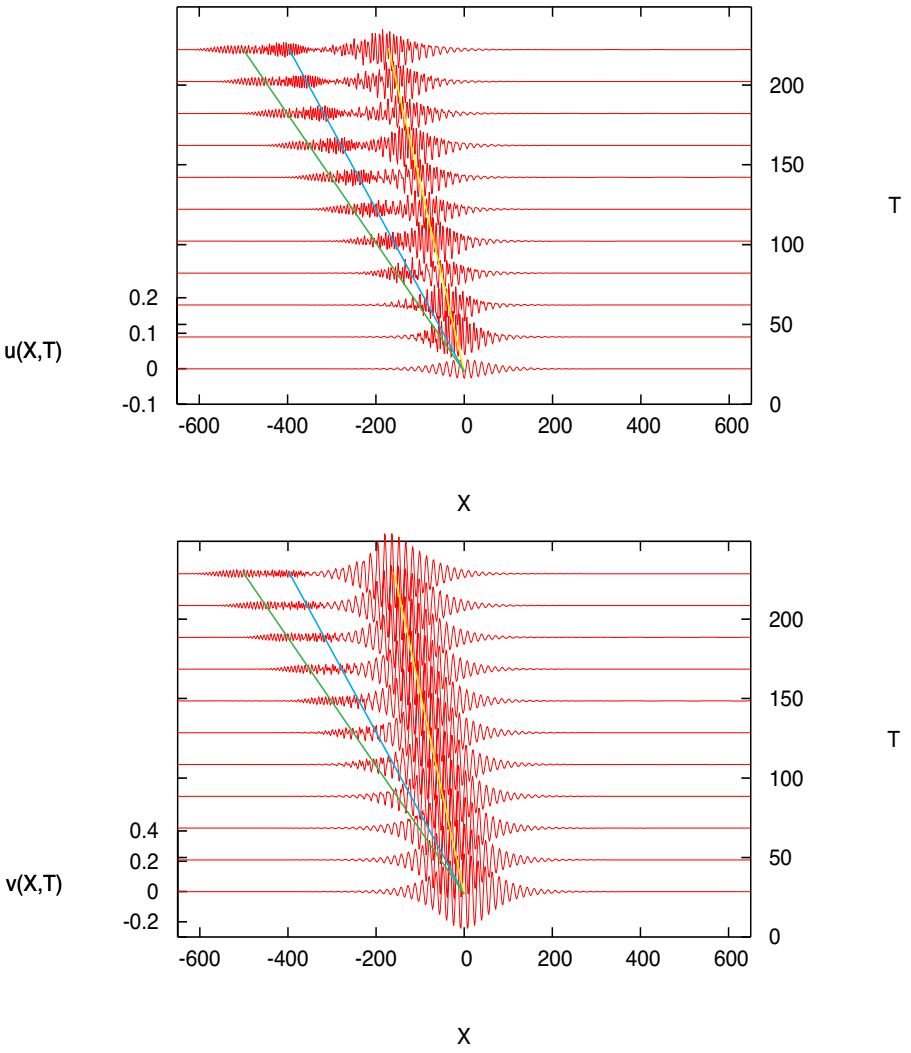

FIGURE 6.34: Numerical simulations for Case D using the wave packet initial condition (6.52) with $k = k_{s2} = 0.395$, corresponding to the point B in Figure 6.6 with $A_0 = 0.25, K_0 = 0.05\,k, V_0 = 1$. The yellow, blue and green lines respectively refer to points (B, F_1), (F_2, D) and G_1.

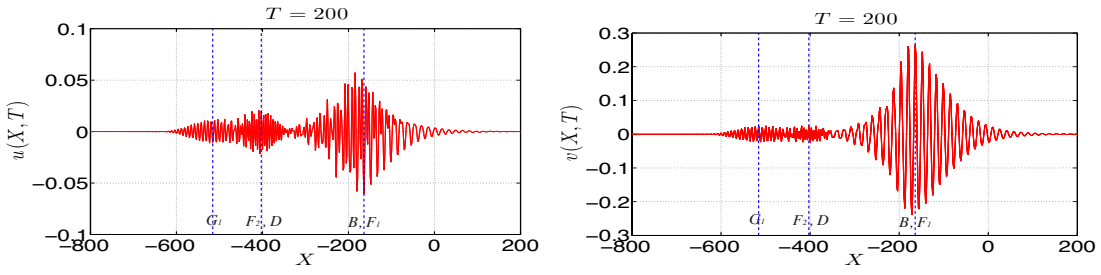

FIGURE 6.35: Same as Figure 6.34, but a cross-section at $T = 200$ for both modes.

6.5 Conclusion

In an extension of Chapter 5, here the focus is on the effect of a background shear flow, using a three-layer model as a guide to the possible values that the normalised coefficients may take. The significant difference that emerges is that the coefficients β, μ of the rotation terms in the coupled Ostrovsky equations (3.30, 3.31), are not necessarily equal, or indeed positive, as is the case in the absence of a background shear flow. Instead, there are four essentially different cases corresponding to different sign combinations of β and μ.

Then, the system was examined numerically, using two different initial conditions. Firstly, the initial condition was a solitary wave type, based on an approximation to the coupled KdV systems obtained when the rotation terms are removed, and for which there is no *a priori* wavenumber selection, see subsection (6.50). Second, the initial condition was a wave packet, see subsection (6.52) based on certain predicted wavenumbers, obtained from the linear dispersion relation where either the phase velocity, or the group velocity, has a turning point. The former can be associated with the possible emergence of a nonlinear steady wave packet, and the latter with the possible emergence of an unsteady nonlinear wave packet.

These two contrasting scenarios were examined numerically for each of the four cases. In each case, these predicted wave packets are identified as the dominant feature of the numerical solution. However, in many cases there was also evidence of nonlinear interactions generating other wave packets associated with some of the possible resonant points identified on each linear dispersion curve. Thus, in comparison with the simulations of the single Ostrovsky equation reported by Grimshaw and Helfrich [1] where only a single unsteady nonlinear wave packet typically emerges, the coupled Ostrovsky system can support a wide variety of nonlinear wave packets. Importantly, it has been shown that the dominant features of the observed dynamical behaviours can be classified and interpreted in terms of the main features of the relevant dispersion curves. This is a first step towards predicting the long-time asymptotic behaviour of the solutions of the initial-value problems for this coupled system of equations.

Chapter 7

Conclusions

7.1 Summary of Research

Our main theme in this thesis has been the development of the coupled Ostrovsky equations, as an appropriate model for the description of resonantly interacting internal waves in a rotating fluid. The introduction of the Earth's background rotation causes significant changes in the wave characteristics. In particular, we have focussed on the emergence of a coherent steadily propagating nonlinear wave packets due to this effect. Helfrich [33] and Grimshaw and Helfrich [1, 34] showed that the long time effect of rotation in the absence of a shear flow is the destruction of the initial internal solitary wave solution by the radiation of small amplitude inertia gravity wave, and the emergence of an unsteady nonlinear wave packet.

The coupled Ostrovsky equations were derived to describe the evolution of the amplitudes of two weakly-nonlinear wave modes whose phase speeds are close, $c_1 \approx c_2$ with $c_1 = c$ and $c_2 = c + \epsilon^2\Delta$ where $\epsilon << 1$ and Δ is the detuning parameter. They are derived from the full set of Euler equations for an inviscid, incompressible fluid with the free surface and rigid bottom boundary conditions, appropriate for the oceanic applications. The PS method has been used in order to develop a numerical solution of the coupled Ostrovsky equations, as explained in Chapter 4. This method is an efficient approach because it can be employed in

simulating both single and coupled system, also can reduce the necessary computer memory and computation time. The scheme is complemented with the sponge layer at the ends of the domain and with the de-aliasing to treat nonlinear terms in the systems.

Chapter 5 is devoted to the case when the shear flow is not present. The coefficients in coupled Ostrovsky equations for the case of a three-layer stratification have been evaluated. Within the scope of this model, both branches of the dispersion relation of the linearised equations resemble the dispersion curve of a typical single Ostrovsky equation, with no spectral gaps, and with an extremum in both group velocity curves. Importantly, in all the cases shown here these extrema are distinct. Hence, based on the results for the single Ostrovsky equation obtained by Grimshaw and Helfrich [1], it is expected that we will observe the emergence of two unsteady nonlinear wave packets associated with the extrema in these group velocity curves. We have discussed two main cases; symmetric case ($N_1 = N_3$) and non-symmetric case ($N_1 \neq N_3$).

The effect of the background shear flow was studied in Chapter 6 and a three-layer model was considered in details. According to the analysis of the dispersion relation, four essentially different cases have been found corresponding to different sign combinations of β and γ, as Case A: $\beta > 0, \mu > 0$, Case B: $\beta > 0, \mu < 0$, Case C: $\beta < 0, \mu > 0$ and Case D: $\beta < 0, \mu < 0$. The complicated dynamics observed in numerical simulations was interpreted in terms of the main features of the linear dispersion curves. Overall, from the dispersion relations and numerical simulations, we emphasise the emergence of steady and unsteady nonlinear wave packets associated with the turning points for either group or phase velocity curve. The formation of a leading nonlinear wave packet with carrier wavenumber, carrier phase speed, and packet group speed is in good agreement with the theoretical predictions from the linear dispersion relation.

An important results has been also obtained for a single Ostrovsky equation, where we showed that a background shear flow can result in a combination of signs of

coefficients in the equation which leads to the emergence of a steady wave packet (see Appendix A).

7.2 Future research

Several extensions to the work in this thesis are possible. Firstly, one could develop a nonlinear Schrödinger (NLS) type model similar to the paper by Grimshaw and Helfrich [1]. In our case with the coupled system, we would construct a weakly nonlinear theory leading to a single higher-order NLS equation for each turning point in order to describe the numerically found wave packets. Secondly, we have derived the coupled Ostrovsky equations to model the strong interaction between the small amplitude internal waves with the consideration of the Earth's rotation. It would be interesting to consider the interaction between the waves of moderate amplitude, extending the recent work by Obregon and Stepanyants [63] for a single Gardner-Ostrovsky equation.

Thirdly, the rotation-modified Kadomtsev-Petviashvili (KP) equation has been studied in Chen et al. [69] to describe small-amplitude, long internal waves in a rotating fluid in two-dimensions. It would be useful to extend the derivation of single rotation-modified KP equation to coupled rotation-modified KP equations. In addition, it would be interesting to investigate the existence of near-resonances for the realistic ocean density and current profiles. This can be done by solving the modal equations numerically.

Appendix A

Single Ostrovsky equation with shear flow

It should be pointed out that the type of the current model considered in Chapter 6 can also lead to the anomalous version of the single Ostrovsky equation when $\lambda\gamma < 0$. In particular, it can be shown that the two-layer reduction of this three-layer model obtained by taking the $h_2 \gg h_{1,3}$, that is a single shallow layer with the density ρ_1 and current U_1 overlying a deep layer with the density ρ_2 and zero current can lead to this anomalous situation. Indeed, for this special case, the dispersion relation determining the speed c is again given by (6.8), now letting $h_2 \gg h_{1,3}$, so that $D_2 = 0$, and then, for a single mode, either $D_1 = 0$ or $D_3 = 0$. Here, choose $D_1 = 0$ and with now $D_3 \neq 0$, it follows from (6.4) that $A_3 = 0$, A_1 is arbitrary and set $A_1 = 1$. Then the modal function ϕ obtained from (6.1) is given by:

$$\phi = 0\,, \quad \phi_z = 0\,, \quad -h < z < -h_2 - h_1\,, \tag{A.1}$$

$$\phi = \frac{h_1 + h_2 + z}{h_2}\,, \quad \phi_z = \frac{1}{h_2}\,, \quad -h_2 - h_1 < z < -h_1\,, \tag{A.2}$$

$$\phi = -\frac{z}{h_1}\,, \quad \phi_z = -\frac{1}{h_1}\,, \quad -h_1 < z < 0\,. \tag{A.3}$$

Without loss of generality, we put $U_2 = 0$ henceforth. Then the speed c is given by:

$$c_{1,2} = \frac{\rho_1 U_1 h_2 \pm \sqrt{(\rho_1 U_1 h_2)^2 - (\rho_1 h_2 + \rho_2 h_1)[g(\rho_1 - \rho_2)h_1 h_2 + \rho_1 U_1^2 h_2]}}{\rho_1 h_2 + \rho_2 h_1} \,. \quad \text{(A.4)}$$

In the limit $h_2 \gg h_1$, we obtain

$$c_{1,2} = U_1 \pm (g' h_1)^{1/2} \quad \text{where} \quad g' = \frac{g(\rho_2 - \rho_1)}{\rho_1} \,. \quad \text{(A.5)}$$

Note that the third layer is not involved at all. To avoid an implicit critical layer, we choose $c > \max[U_1, 0]$, or $c < \min[U_1, 0]$. The first case, denoted as the positive mode propagating to the right, holds provided that $U_1 + (g' h_1)^{1/2} > 0$, and the latter, denoted as the negative mode propagating to the left, holds provided that $U_1 - (g' h_1)^{1/2} < 0$.

Now all coefficients in the Ostrovsky equation (2.46) can be calculated, taking into account that $h_2 \gg h_1$ where appropriate:

$$I\nu = \frac{3\,c^2 \rho_2}{h_2^2} - \frac{3\rho_1 g'}{h_1} \to -\frac{3\rho_1 g'}{h_1} \,, \quad \text{(A.6)}$$

$$I\lambda = \frac{c^2 \rho_2 h_2}{3} + \frac{\rho_1 h_1^2\, g'}{3} \to \frac{c^2 \rho_2 h_2}{3} \,, \quad \text{(A.7)}$$

$$I\gamma = \frac{\rho_1 \tilde{f}^2}{h_1}[1 + \frac{1}{2}\log\frac{|W_2|}{|W_1|} - \frac{U_1}{2W_1}\log\frac{\rho_2}{\rho_1} + \frac{\rho_2 h_1}{\rho_1 h_2}(1 - \frac{1}{2}\log\frac{|W_2|}{|W_1|} + \frac{U_2}{2W_2}\log\frac{\rho_2}{\rho_1})]$$

$$\to \frac{\rho_1 \tilde{f}^2}{h_1}(1 + \frac{1}{2}\log\frac{|W_2|}{|W_1|} - \frac{U_1}{2W_1}\log\frac{\rho_2}{\rho_1}) \,, \quad \text{(A.8)}$$

$$I = \frac{2\rho_1 W_1}{h_1} - \frac{2\rho_2 W_2}{h_2} \to \frac{2\rho_1 W_1}{h_1} \,. \quad \text{(A.9)}$$

Note that $I > 0$, so that $\nu < 0, \lambda > 0$, for the mode to the right, and $I < 0$, so that $\nu > 0, \lambda < 0$, for the mode to the left. As expected $\nu\lambda < 0$ for both modes, which describes waves of depression. In the Boussinesq approximation when $\rho_1 \approx \rho_2$, the following is obtained:

$$I\gamma = \frac{\rho_1 \tilde{f}^2}{h_1}\{\frac{h}{h_2} + \frac{h_2 - h_1}{2h_2}\log[\frac{|c|}{|c - U_1|}]\} \,. \quad \text{(A.10)}$$

Thus, $I\gamma > 0$ unless U_1 is such that:

$$\frac{|c|}{\sqrt{g'h_1}} = |1 \pm \frac{U_1}{\sqrt{g'h_1}}| < e^{-2\,\alpha}\,, \tag{A.11}$$

where $\alpha = h/(h_2 - h_1)$. Since h_2 is large, $\alpha \to 1$ and in this limit (A.11) becomes

$$\begin{aligned} -1 < \tfrac{U_1}{\sqrt{g'h_1}} < e^{-2} - 1 = -0.865\,, \\ \text{or}\,, \qquad 1 > \tfrac{U_1}{\sqrt{g'h_1}} > 1 - e^{-2} = 0.865\,, \end{aligned} \tag{A.12}$$

for the mode to the right and left respectively. Here we also used the exclusion of an implicit critical layer condition. Note that the two modes are essentially the same, so it is enough to consider the mode to the right. Then unless (A.12) holds, $\lambda\gamma > 0$ and we have the typical Ostrovsky equation with only unsteady wave packet solutions. But if instead (A.12) holds then $\lambda\gamma < 0$ and this leads to the anomalous Ostrovsky equation for which there is a steady envelope wave packet solution, discussed by Obregon and Stepanyants [28] in a different setting.

A typical dispersion curve is shown in Figure A.1, where $\nu = -4.7\,\mathrm{x}\,10^{-3}\,, \lambda = 41.64$ and $\gamma = -1.9\,\mathrm{x}\,10^{-5}\,$, when setting $h_1 = 0.1\,km, h_2 \approx 3.0\,km, U_1 = -0.3\,m\,s^{-1}$, $\rho_1 = 1\,kg\,m^{-3}$ and $\rho_2 = 1.0001\,kg\,m^{-3}$. Here, $\alpha \approx 1.069$ and $U_1/\sqrt{g'h_1} \approx -0.958$, while $e^{-2\alpha} - 1 \approx -0.822$. There exists a spectral gap for the phase speed, which has a maximum value $c = -0.057$ at $k = 0.026$. The group velocity is positive as $k \to 0$, but negative as $k \to \infty$, and at the point of maximum phase speed, the phase and group velocities are equal. Hence a steady wave packet can exist.

A typical numerical result is shown in Figures (A.2) and (A.3) using the wave packet initial condition given as:

$$A(s,0) \;\; = \;\; V_0 A_0\,\mathrm{sech}(K_0 X)\cos(kX)\,, \tag{A.13}$$

where $V_0 = 1\,, A_0 = 8\,, K_0 = 0.25\,k$ and $k = 0.026$. The solution is dominated by a steady wave packet, as expected, with the speed -0.069, which is in good agreement with the theoretical value.

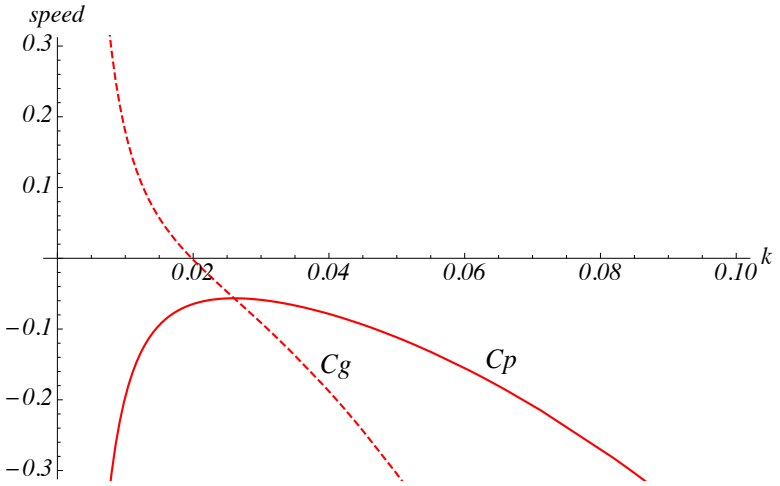

FIGURE A.1: Dispersion relation for the single Ostrovsky equation when $\lambda\gamma < 0$.

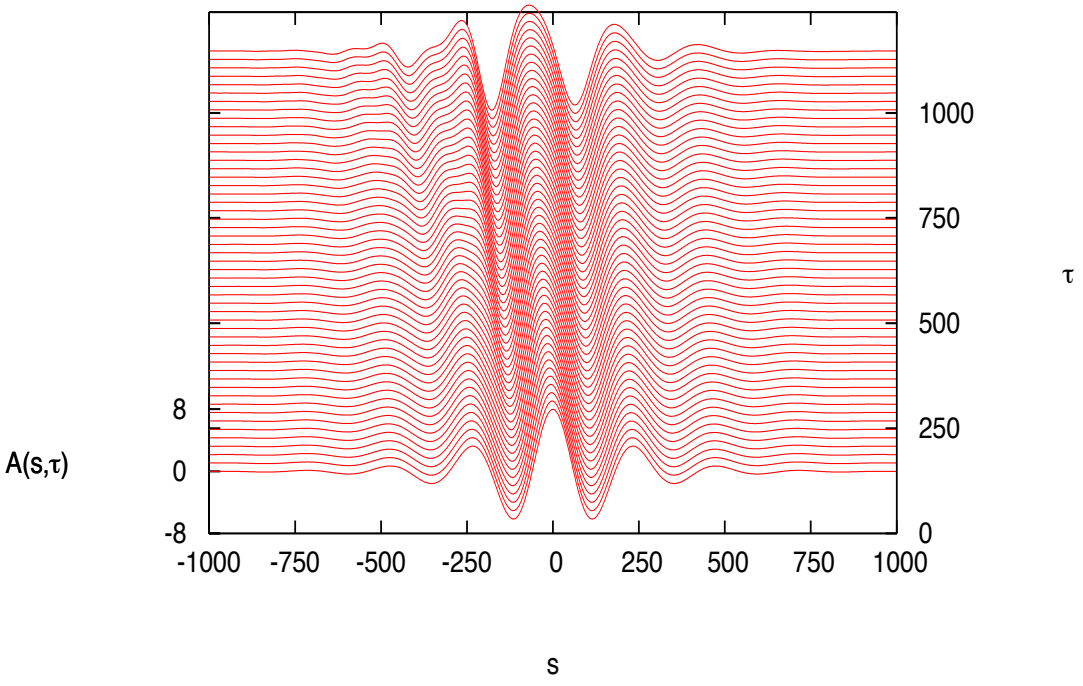

FIGURE A.2: Numerical simulation for the single Ostrovsky equation when $\lambda\gamma < 0$ using the wave packet initial condition (A.13) with $k = 0.026\,, A_0 = 8, K_0 = 0.25\ k$ and $V_0 = 1$.

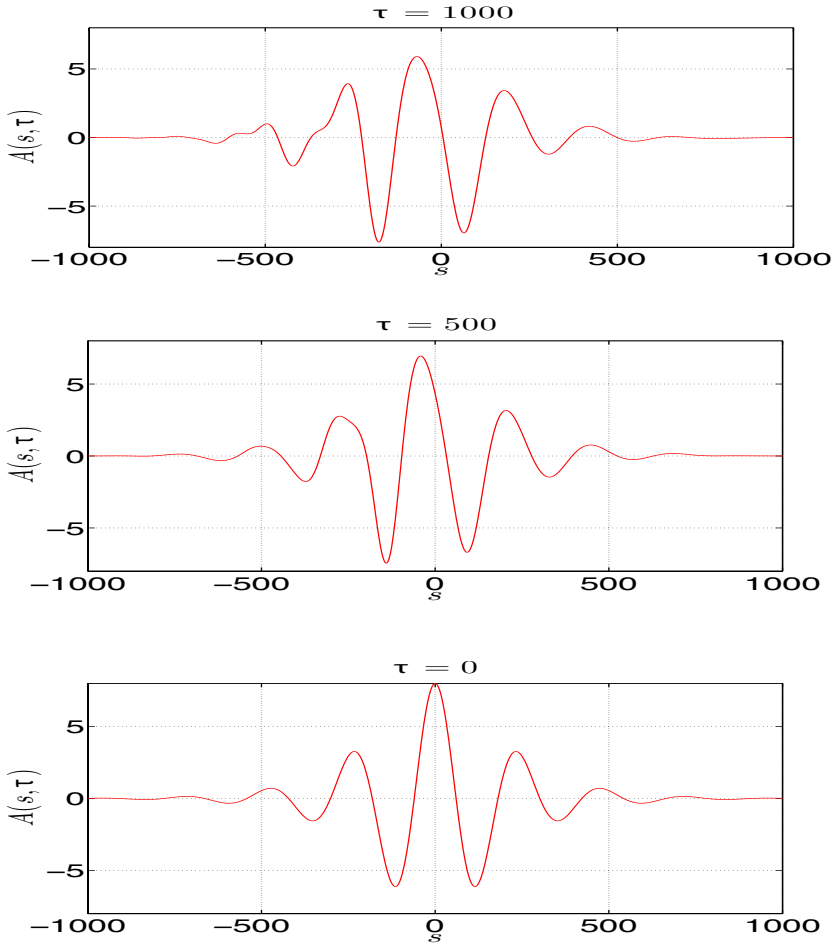

FIGURE A.3: Same as Figure A.2, but a cross-section at $\tau = 0\,, 500\,, 1000$.

Bibliography

[1] R. H. J. Grimshaw and K. R. Helfrich. Long-time solutions of the Ostrovsky equation. *Studies in Applied Mathematics*, 121(1):71–88, 2008.

[2] R. H. J. Grimshaw. Internal solitary waves. In R. H. J. Grimshaw, editor, *Environmental Stratified Flows*, volume 3 of *Topics in Environmental Fluid Mechanics*, pages 1–27. Springer US, 2001. ISBN 978-0-7923-7605-7.

[3] P. Holloway, E. Pelinovsky, and T. Talipova. Internal tide transformation and oceanic internal solitary waves. In R. H. J. Grimshaw, editor, *Environmental Stratified Flows*, volume 3 of *Topics in Environmental Fluid Mechanics*, pages 29–60. Springer US, 2001. ISBN 978-0-7923-7605-7.

[4] K. R. Helfrich and W. K. Melville. Long nonlinear internal waves. *Annual Review of Fluid Mechanics*, 38:395–425, 2006.

[5] K. S. Roger. Travelling waves and bores in the lower atmosphere: the 'morning glory' and related phenomena. *Earth-Science Reviews*, 25(4):267 – 290, 1988.

[6] J. W. Rottman and R. H. J. Grimshaw. Atmospheric internal solitary waves. In Roger Grimshaw, editor, *Environmental Stratified Flows*, volume 3 of *Topics in Environmental Fluid Mechanics*, pages 61–88. Springer US, 2002.

[7] T. B. Benjamin. Internal waves of finite amplitude and permanent form. *Journal of Fluid Mechanics*, 25:241–270, 1966.

[8] R. H. J. Grimshaw, E. Pelinovsky, T. Talipova, and O. Kurkina. Internal solitary waves: propagation, deformation and disintegration. *Nonlinear Processes in Geophysics*, 17(6):633–649, 2010.

[9] L. A. Ostrovsky and Y. A. Stepanyants. Internal solitons in laboratory experiments: comparison with theoretical models. *Chaos*, 15(3):37111, 2005.

[10] R. H. J. Grimshaw, E. Pelinovsky, and T. Talipova. Modelling internal solitary waves in the coastal ocean. *Surveys in Geophysics*, 28(4):273–298, 2007. ISSN 0169-3298.

[11] J. S. Russell. Report on waves. In *Report of the 14th Meeting of the British Association for the Advancement of Science*, pages 311–390. John Murray, 1845.

[12] J. W. S. Lord Rayleigh. On waves. *Phil. Mag.*, 1:257–279, 1876.

[13] D. J. Korteweg and G. de Vries. On the change of form of long waves advancing in a rectangular canal, and on a new type of long stationary waves. *Philosophical Magazine*, 39:422–443, 1895.

[14] J. W. Miles. Solitary waves. *Annual Review of Fluid Mechanics*, 12:11– 43, 1980.

[15] J. W. Miles. The Korteweg-de Vries equation: a historical essay. *Journal of Fluid Mechanics*, 106:131–147, 1981.

[16] C-Y. Lee and R. C. Beardsley. The generation of long nonlinear internal waves in a weakly stratified shear flow. *Journal of Geophysical Research*, 79 (3):453–462, 1974.

[17] L. A. Ostrovsky. Nonlinear internal waves in a rotating ocean. *Oceanology*, 18:181–191, 1978.

[18] S. A. Maslowe and L. G. Redekopp. Long nonlinear waves in stratified shear flows. *Journal of Fluid Mechanics*, 101:321–348, 1980.

[19] P. E. Holloway, E. Pelinovsky, and T. Talipova. A generalized Korteweg-de Vries model of internal tide transformation in the coastal zone. *Journal of Geophysical Research: Oceans*, 104:18333–18350, 1999.

[20] N. J. Zabusky and M. D. Kruskal. Interactions of 'Solitons' in a collisionless plasma and the recurrence of intial states. *Physical Review Letters*, 15:240–243, 1965.

[21] C. S. Gardner, J. M. Greene, M. D. Kruskal, and R. M. Miura. Method for solving the Korteweg-de Vries equation. *Phys. Rev. Lett.*, 19:1095–1097, Nov 1967.

[22] L. A. Ostrovsky and Y. A. Stepanyants. Do internal solitions exist in the ocean? *Reviews of Geophysics*, 27(3):293–310, 1989.

[23] G-Y. Chen and J. P. Boyd. Analytical and numerical studies of weakly nonlocal solitary waves of the rotation-modified Korteweg-de Vries equation. *Physica D: Nonlinear Phenomena*, 155(3 - 4):201 – 222, 2001.

[24] R. H. J. Grimshaw. Evolution equations for weakly nonlinear, long internal waves in a rotating fluid. *Studies in Applied Mathematics*, 73:1–33, 1985.

[25] R. H. J. Grimshaw, L. A. Ostrovsky, V. I. Shrira, and Y. A. Stepanyants. Long nonlinear surface and internal gravity waves in a rotating ocean. *Surveys in Geophysics*, 19(4):289–338, 1998. ISSN 0169-3298.

[26] R. H. J. Grimshaw, J.-M. He, and L. A. Ostrovsky. Terminal damping of a solitary wave due to radiation in rotational systems. *Studies in Applied Mathematics*, 101(2):197–210, 1998. ISSN 1467-9590.

[27] L. A. Ostrovsky and Y. A. Stepanyants. Nonlinear surface and internal waves in rotating fluids. In A. V. Gaponov-Grekhov, M. I. Rabinovich, and J. Engelbrecht, editors, *Nonlinear Waves 3*, Research Reports in Physics, pages 106–128. Springer Berlin Heidelberg, 1990.

[28] M. A. Obregon and Y. A. Stepanyants. Oblique magneto-acoustic solitons in a rotating plasma. *Physics Letters A*, 249:315–323, 1998.

[29] A. J. Whitfield and E. R. Johnson. Rotation-induced nonlinear wavepackets in internal waves. *Physics of Fluids (1994-present)*, 26(5):056606, 2014.

[30] A. I. Leonov. The effect of the Earth's rotation on the propagation of weak nonlinear surface and internal waves. *Annals of the New York Academy of Sciences*, 373(1):150–159, 1981.

[31] O. A. Gilman, R. H. J Grimshaw, and Y. A. Stepanyants. Dynamics of internal solitary waves in a rotating fluid. *Dynamics of Atmospheres and Oceans*, 23(1-4):403 – 411, 1996.

[32] D. Renouard and J-P. Germain. Experimental study of long nonlinear internal waves in rotating fluid. *Annales Geophysicae*, 12(2–3):254–264, 1994.

[33] K. R. Helfrich. Decay and return of internal solitary waves with rotation. *Physics of Fluids*, 19(2):026601, 2007.

[34] R. H. J. Grimshaw and K. R. Helfrich. The effect of rotation on internal solitary waves. *IMA Journal of Applied Mathematics*, 77(3):326–339, 2012.

[35] Y. Daisuke and K. Takuji. Strongly nonlinear envelope soliton in a lattice model for periodic structure. *Wave Motion*, 34(1):97–107, 2001.

[36] R. H. J. Grimshaw, K. R. Helfrich, and E. R. Johnson. The reduced Ostrovsky equation: Integrability and breaking. *Studies in Applied Mathematics*, 129 (4):414–436, 2012.

[37] E. R. Johnson and R. H. J. Grimshaw. Modified reduced Ostrovsky equation : Integrability and breaking. *Phys Rev E Stat Nonlin Soft Matter Phys*, 88 (2):021201, 2013.

[38] C. Eckart. Internal waves in the ocean. *Physics of Fluids*, 4(7):791–799, 1961.

[39] J. A. Gear and R. H. J. Grimshaw. Weak and strong interactions between internal solitary waves. *Studies in Applied Mathematics*, 70(1):235–258, 1984.

[40] R. H. J. Grimshaw. Coupled Korteweg-de Vries equations. In Ramon G. Rubio, Yuri S. Ryazantsev, Victor M Starov, Guo-Xiang Huang, Alexander P

Chetverikov, Paolo Arena, Alex A. Nepomnyashchy, Alberto Ferrus, and Eugene G. Morozov, editors, *Without Bounds: A Scientific Canvas of Nonlinearity and Complex Dynamics*, Understanding Complex Systems, pages 317–333. Springer Berlin Heidelberg, 2013. ISBN 978-3-642-34069-7.

[41] T. Gerkema. A unified model for the generation and fission of internal tides in a rotating ocean. *Journal of Marine Research*, 54(3):421–450, 1996.

[42] K. R. Khusnutdinova, A. M. Samsonov, and A. S. Zakharov. Nonlinear layered lattice model and generalized solitary waves in imperfectly bonded structures. *Physical Review E*, 79:056606, May 2009.

[43] K. R. Khusnutdinova and K. R. Moore. Initial-value problem for coupled Boussinesq equations and a hierarchy of Ostrovsky equations. *Wave Motion*, 48(8):738–752, 2011.

[44] K. R. Khusnutdinova, K. R. Moore, and D. E. Pelinovsky. Validity of the weakly nonlinear solution of the Cauchy problem for the Boussinesq-type equation. *Studies in Applied Mathematics*, 133(1):52–83, 2014.

[45] P. K. Kundu and I. M. Cohen. *Fluid Mechanics*. Elsevier Science, 2010. ISBN 9780123814005.

[46] M. J. Ablowitz and H. Segur. *Solitons and the Inverse Scattering Transform*. SIAM Studies in Applied Mathematics. Society for Industrial and Applied Mathematics, 1981.

[47] V. N. Galkin and Y. A. Stepanyants. On the existence of stationary solitary waves in a rotating fluid. *Journal of Applied Mathematics and Mechanics*, 55 (6):939–943, 1991.

[48] R. H. J. Grimshaw, K. R. Helfrich, and E. R. Johnson. Experimental study of the effect of rotation on nonlinear internal waves. *Physics of Fluids*, 25(5): 056602, 2013.

[49] A. Alias, R. H. J. Grimshaw, and K. R. Khusnutdinova. On strongly interacting internal waves in a rotating ocean and coupled Ostrovsky equations. *Chaos: An Interdisciplinary Journal of Nonlinear Science*, 23(2): 023121, 2013.

[50] R. H. J. Grimshaw and I. Gerard. Solitary waves of a coupled Korteweg-de Vries system. *Mathematics and Computers in Simulation*, 62(1-2):31–40, 2003.

[51] C. Fochesato, F. Dias, and R. H. J. Grimshaw. Generalized solitary waves and fronts in coupled korteweg-de vries systems. *Physica D: Nonlinear Phenomena*, 210(1–2):96 – 117, 2005.

[52] T. F. Chan and T. Kerkhoven. Fourier methods with extended stability intervals for the Korteweg-de Vries equation. *SIAM Journal on Numerical Analysis*, 22(3):441–454, 1985.

[53] C. Canuto, M. Y. Hussaini, A. Quarteroni, and T. A. Zang. *Spectral methods in fluid dynamics*. Springer series in computational physics. Springer-Verlag, 1988.

[54] F. Z Nouri and D. M Sloan. A comparison of fourier pseudospectral methods for the solution of the Korteweg-de Vries equation. *Journal of Computational Physics*, 83(2):324–344, 1989.

[55] J. P. Boyd. *Chebyshev and Fourier Spectral Methods*. Dover books on mathematics. Dover Publications, 2001.

[56] X. Huang and X. Zhang. A fourier pseudospectral method for some computational aeroacoustics problems. *International Journal of Aeroacoustics*, 5(3): 279–294, 2006.

[57] A. Rashid. Convergence analysis of three-level Fourier Pseudospectral method for Korteweg-de Vries Burgers equation. *Computers and Mathematics with Applications*, 52(5):769 –778, 2006. Hot Topics in Applied and Industrial Mathematics.

[58] Y. H. Thomas and L. Ruo. Computing nearly singular solutions using Pseudo-spectral methods. *Journal of Computational Physics*, 226(1):379–397, 2007.

[59] C. Klein. Fourth order time-stepping for low dispersion Korteweg-de Vries and nonlinear schrodinger equations. *ETNA. Electronic Transactions on Numerical Analysis [electronic only]*, 29:116–135, 2007.

[60] V. Gulkac and T. Ozis. A numerical application of the semi-implicit pseudo-spectral method for the Korteweg-de Vries equation. *Ozean Journal of Applied Sciences*, pages 25–31, 2009.

[61] A. Rashid and A. I. M. Ismail. A Fourier Pseudospectral method for solving coupled viscous Burgers equations. *Comput. Meth. in Appl. Math.*, 9(4):412–420, 2009.

[62] T. Yaguchi, T. Matsuo, and M. Sugihara. Conservative numerical schemes for the Ostrovsky equation. *Journal of Computational and Applied Mathematics*, 234(4):1036–1048, 2010. Proceedings of the Thirteenth International Congress on Computational and Applied Mathematics (ICCAM-2008), Ghent, Belgium, 711 July, 2008.

[63] M. A. Obregon and Y. A. Stepanyants. On numerical solution of the Gardner-Ostrovsky equation. *Mathematical Modelling of Natural Phenomena*, 7:113–130, 1 2012.

[64] J. Cooley and J. Tukey. An algorithm for the machine calculation of complex fourier series. *Mathematics of Computation*, 19(90):297–301, 1965.

[65] M. T. Heideman, D. H. Johnson, and C. S. Burrus. Gauss and the history of the fast fourier transform. *Archive for History of Exact Sciences*, 34(3): 265–277, 1985. ISSN 0003-9519.

[66] L. S. Mulholland and D. M. Sloan. The effect of filtering on the pseudospectral solution of evolutionary partial differential equations. *Journal of Computational Physics*, 96(2):369 – 390, 1991.

[67] R. H. J. Grimshaw. *Models for Long-wave Instability Due to a Resonance Between Two Waves*. Applied mathematics reports and preprints. Monash University, Department of Mathematics and Statistics, 1998.

[68] R. H. J. Grimshaw and Y. Skyrnnikov. Long-wave instability in a three-layer stratified shear flow. *Studies in Applied Mathematics*, 108(1):77–88, 2002.

[69] R. M. Chen, V. M. Hur, and Y. Liu. Solitary waves of the rotation-modified Kadomtsev-Petviashvili equation. *Nonlinearity*, 21(12):2949, 2008.